



HAL
open science

Grazing Incidence Fast Atom Diffraction in high-pressure conditions: from collisional decoherence to real-time characterization of thin-film growth by HiPIMS

Arindam Mukherjee

► **To cite this version:**

Arindam Mukherjee. Grazing Incidence Fast Atom Diffraction in high-pressure conditions: from collisional decoherence to real-time characterization of thin-film growth by HiPIMS. Material chemistry. Université Paris-Saclay, 2023. English. NNT: 2023UPASP146 . tel-04925285

HAL Id: tel-04925285

<https://theses.hal.science/tel-04925285v1>

Submitted on 2 Feb 2025

HAL is a multi-disciplinary open access archive for the deposit and dissemination of scientific research documents, whether they are published or not. The documents may come from teaching and research institutions in France or abroad, or from public or private research centers.

L'archive ouverte pluridisciplinaire **HAL**, est destinée au dépôt et à la diffusion de documents scientifiques de niveau recherche, publiés ou non, émanant des établissements d'enseignement et de recherche français ou étrangers, des laboratoires publics ou privés.

Grazing Incidence Fast Atom Diffraction in high-pressure conditions: from collisional decoherence to real-time characterization of thin-film growth by HiPIMS

*Diffraction d'atomes rapides en incidence rasante à haute pression :
de la décohérence collisionnelle à la caractérisation en temps réel de
la croissance de couches minces par HiPIMS*

Thèse de doctorat de l'université Paris-Saclay

École doctorale n° 572: ondes et matière (EDOM)

Spécialité de doctorat: Physique

Graduate School : Physique. Référent : Faculté des sciences d'Orsay

Thèse préparée dans l'unité de recherche **Institut des Sciences Moléculaires
d'Orsay (Université Paris-Saclay, CNRS)**, sous la direction de **Hocine KHEMLICHE**,
Chargé de recherche, et le co-encadrement de **Tiberiu MINEA**, Professeur

Thèse soutenue à Paris-Saclay, le 21 Novembre 2023, par

Arindam MUKHERJEE

Composition du jury:

Membres du jury avec voix délibérative

Jacques ROBERT

Professeur, Université Paris-Saclay

Grégory ABADIAS

Professeur, Université de Poitiers

Gabriel DUTIER

Maître de conférences HDR, Université Sorbonne Paris Nord

Stéphane LUCAS

Professeur, Université de Namur

Kerstin THORWARTH

Scientifique senior, Swiss Federal Laboratories for Materials Science
and Technology (Empa)

Président

Rapporteur & Examineur

Rapporteur & Examineur

Examineur

Examinatrice

Titre: Diffraction d'atomes rapides en incidence rasante à haute pression : de la décohérence collisionnelle à la caractérisation en temps réel de la croissance de couches minces par HiPIMS.

Mots clés: Diffraction d'atomes rapides en incidence rasante (GIFAD), décohérence collisionnelle, pulvérisation magnétron impulsionnelle de haute puissance (HiPIMS), croissance de couches minces, diagnostic temps réel croissance de couches minces, analyse de la structure de la surface.

Résumé: La caractérisation temps-réel de la croissance de couches minces est un défi majeur car les paramètres de croissance prédéterminent pour une large part les propriétés du film. Ceci est particulièrement problématique dans le cas du dépôt de couches minces par pulvérisation magnétron (MS) où la présence de champs électromagnétiques à proximité du substrat rend inopérante la diffraction d'électrons de haute énergie (RHEED). A ce jour, il n'existe pas d'approche simple en laboratoire pour suivre la croissance par MS et obtenir des informations en temps réel sur le mode de croissance, les propriétés cristallographiques, l'orientation de la maille, etc. Ce travail porte sur le développement et la validation d'un nouvel outil de caractérisation de surfaces et de couches minces dans un environnement haute pression (au-delà de 10^{-4} mbar) utilisant la diffraction d'atomes rapides en incidence rasante (GIFAD). GIFAD est une technique sensible à l'extrême surface et non destructive, considérée comme un complément/alternative au RHEED. Elle est exploitée pour suivre en temps réel la croissance de couches minces de l'ultravide jusqu'à environ 10^{-6} mbar. La première partie du travail est dédiée à la mise en œuvre d'un nouveau dispositif, HP-GIFAD, permettant un fonctionnement à plus haute pression. Une solution compacte à double pompage différentiel,

qui préserve la cohérence du faisceau ainsi qu'un bon rapport signal/bruit sur le détecteur, permet d'opérer HP-GIFAD jusqu'à 10^{-2} mbar (1 Pa) d'Ar. La deuxième partie s'intéresse aux propriétés fondamentales du faisceau diffracté par la surface et se propageant dans la zone haute pression. Une décohérence induite par l'interaction du paquet d'ondes avec les atomes d'Ar environnants a pu être quantifiée, elle est associée à un rétrécissement anormal des pics de Bragg qui dépend fortement de la largeur de cohérence initiale du faisceau. La dernière partie de la thèse se concentre sur la compatibilité de HP-GIFAD avec le dépôt de couches minces par pulvérisation magnétron impulsionnelle de haute puissance (HiPIMS), une variante du MS. La pulsation du détecteur, anti-synchronisée sur l'impulsion du plasma, permet de réduire sensiblement l'effet des particules, identifiées comme des atomes métastables produits par le plasma, sur le détecteur. Ainsi, du point de vue technique, HP-GIFAD est pleinement compatible avec HiPIMS. Les résultats préliminaires sur la croissance de films de Cu sur un substrat isolant indiquent une croissance par îlots ; un ajustement supplémentaire des paramètres HiPIMS (puissance et durée de l'impulsion, accélération des ions, pression Ar, etc.) devrait favoriser un mode de croissance en couche par couche.

Title: Grazing Incidence Fast Atom Diffraction in high-pressure conditions: from collisional decoherence to real-time characterization of thin-film growth by HiPIMS.

Keywords: Grazing Incidence Fast Atom Diffraction (GIFAD), collisional decoherence, High Power Impulse Magnetron Sputtering (HiPIMS), thin film growth, real-time growth monitoring, surface structure analysis.

Abstract: Real-time characterization of thin film growth is a major issue because the growth parameters largely predetermine the properties of the film. This is particularly challenging in the case of film deposition by magnetron sputtering (MS) where the presence of electromagnetic fields near the substrate makes high energy electron diffraction (RHEED) ineffective. To date, there is no simple laboratory approach to monitor thin film growth by MS and obtain real-time information on growth mode, crystallographic properties, lattice orientation, etc. This work focuses on the development and validation of a new tool for characterizing surfaces and thin layers in a high pressure environment (beyond 10^{-4} mbar) using Grazing Incidence Fast Atom Diffraction (GIFAD). GIFAD is an extremely surface sensitive and non-destructive technique, considered as a complement/alternative to RHEED. It is used to monitor in real time the growth of thin films from ultra-high vacuum up to approximately 10^{-6} mbar. The first part of the work is dedicated to the implementation of a new device, HP-GIFAD, allowing operation at higher pressures. A compact solution with double differential pumping, which preserves the

beam coherence and a good signal-to-noise ratio on the detector, allows HP-GIFAD to operate up to 10^{-2} mbar (1 Pa) of Ar. The second part investigates the fundamental properties of the beam diffracted by the surface and propagating in the high pressure zone. A decoherence induced by the interaction of the wave packet with the surrounding Ar atoms could be quantified; it is associated with an anomalous narrowing of the Bragg peaks that strongly depends on the coherence width of the primary beam. The last part of the thesis focuses on the compatibility of HP-GIFAD with thin film deposition by high-power impulse magnetron sputtering (HiPIMS), a variant of MS. Pulsing the detector, in anti-synchronization with the plasma pulse, makes it possible to significantly reduce the effect of particles, identified as metastable atoms produced by the plasma, on the detector. Thus, from a technical point of view, HP-GIFAD is fully compatible with HiPIMS. Preliminary results on the growth of Cu films on an insulating substrate indicate an island growth; further adjustment of the HiPIMS parameters (pulse power and duration, ion acceleration, Ar pressure, etc.) should favor a layer-by-layer growth mode.

Dedicated to my family

Contents

Gratitude in few words...	3
Résumé	5
1 Introduction	12
1.1 Surfaces and interfaces: History, definition, importance	12
1.2 Thin-film deposition technologies	14
1.2.1 Physical Deposition	14
1.2.1.1 Vacuum evaporation	14
1.2.1.2 Sputter deposition	15
1.2.1.3 Pulsed Laser Deposition (PLD)	15
1.2.1.4 Cathodic Arc Deposition (arc-PVD)	16
1.2.2 Chemical deposition	16
1.2.2.1 Chemical Vapor Deposition (CVD)	16
1.2.3 Different thin film growth modes	17
1.2.4 Thin film and surface characterization	17
1.2.5 Different <i>in-situ</i> techniques for thin film growth	20
1.3 Overview of the thesis	22
2 High-pressure Grazing Incidence Fast Atom Diffraction (HP-GIFAD): experimental setup, operational principles, and results	23
2.1 Introduction	24
2.2 Experimental setup	27
2.2.1 Ion source	27
2.2.2 Neutralization or charge exchange cell	27
2.2.3 The UHV chamber and the detector system	29
2.2.3.1 The UHV chamber	29
2.2.3.2 The detector system	36
2.3 Principles of GIFAD	37
2.3.1 Scattering geometry	37
2.3.2 Quantitative analysis of the diffraction pattern	40
2.4 Experimental results	45
2.4.1 Analysis of direct beam and scattered beams	46
2.4.2 Beam divergence	48
2.4.3 Number of collisions along the path length of beam	48
2.4.4 Scattered beam intensity before and after the experiments	49
2.5 Conclusions and perspectives	49

3	Observation of collisional decoherence using Grazing Incidence Fast Atom Diffraction	51
3.1	Introduction	51
3.2	Experimental results	53
3.2.1	Influence of pressure on the diffraction pattern	54
3.2.1.1	Lateral profile	54
3.2.1.2	Polar profile	58
3.2.2	Decoherence from surface	60
3.2.2.1	Analysis of perylene deposition on Ag(110)	60
3.2.2.2	Analysis of KCl deposition on Ag(001)	62
3.2.3	Decoherence with large slit size	64
3.2.4	Dependency of intensity attenuation and decoherence	64
3.3	Near field region- an overview	65
3.3.1	Decoherence from near field region-Recoiling of Ar atoms	68
3.4	Discussions and conclusions	69
4	Compatibility of GIFAD with High Power Impulse Magnetron Sputtering(HiPIMS)	72
4.1	Introduction	72
4.1.1	An introduction of plasma	72
4.1.2	DC glow discharges	73
4.1.3	Electrical breakdown	76
4.1.4	Interactions of ions with surface	78
4.1.5	The sputtering process	79
4.1.6	Magnetron Sputtering	80
4.1.7	Direct Current Magnetron Sputtering (DCMS)	81
4.1.8	High Power Impulse Magnetron Sputtering (HiPIMS)	82
4.2	Experimental results	85
4.2.1	Condition of GIFAD detector in the presence of plasma	85
4.2.2	Possible source of noise on GIFAD detector	85
4.2.3	Effect of delay between detector ON time and HiPIMS pulse on noise	87
4.2.4	Direct beam condition	88
4.3	Conclusions and discussions	90
5	Ongoing work and future perspectives	91
5.1	Introduction	91
5.2	Experimental results and discussion	92
5.3	Conclusions and perspectives	96
6	Conclusions and perspectives	98
A	Comparison between LEED, RHEED, TEAS, GIFAD: wavelength, energy, incidence angle	101
B	Binary elastic collision	102
C	Density matrix	104

Gratitude in few words...

I would like to convey my heartfelt gratitude to those people who constantly supported me in my journey toward my Ph.D.

I am extremely grateful to my Ph.D. supervisors **Dr. Hocine KHEMLICHE** and **Prof. Tiberiu MINEA** for giving me the chance to be a part of their team and introduce me to the world of research. Their guidance, constant support, and expertise throughout the research journey helped to shape the thesis. I have spent the majority of my time working closely with Hocine, and I can genuinely state that he is an exceptional individual who encouraged me and tried to fulfill all of my requests. I extend my gratitude to Tiberiu for his willingness to provide assistance whenever I knocked on his door. I appreciate your patience and tolerance over the last three years.

I am deeply and sincerely thankful to the esteemed jury members **Prof. Jacques ROBERT**, **Prof. Grégoire ABADIAS**, **Dr. Gabriel DUTIER**, **Dr. Kerstin THORWARTH**, and **Prof. Stéphane LUCAS** to accept the invitation to evaluate my work.

I take the opportunity to thank my thesis committee members **Dr. Thomas PINO** and **Prof. Jacques ROBERT** to provide me valuable feedback during the interactions.

I am thankful to **Dr. Franck FORTUNA** for assisting us with the SEM experiments and generously providing the turbo pump to continue the experiments on thin film deposition.

I am grateful to the members of the Nanophysics team who have given valuable suggestions and engaging discussions during our meeting, which gave me a boost in the research journey. I am delighted to meet with **Prof. Elizabeth BOER DUCHEMIN**, a perfect team leader who consistently offered me encouragement and support.

Remembering the quote by **Helen KELLER** "*Alone we can do so little; together we can do so much*", I want to express my sincere thanks to my teammates **Dr. Anouchah MOMENI**, **Dr. Elena-Magdalena STAICU CASAGRANDE**, **Abdel**, and **Christian**.

When it comes to the technical knowledge I have gained, I am truly grateful to **Anouchah**. I have always enjoyed his companionship as he was eager and willing to provide all the answers to my scientific and technical questions.

I want to express my gratitude to **Magda** for her unwavering support and putting effort into clarifying complex stuff and making them more accessible and comprehensible. I am thankful to her family. I cherish the moments I spent with **Thomas**, **Horia**, and **Ioan**—my best wishes to **Horia** and **Ioan** for their future.

The moments I shared with **Abdel** will forever remain a cherished treasure. I was consistently enthusiastic about engaging in discussions with him to acquire a deeper understanding of his work. In addition

to our scientific endeavors, I had the opportunity to explore the wonders of Paris alongside him. I wish him all the best for his upcoming defense and for all his future endeavors.

Christian, your ability to lighten the mood has been a blessing during my stressful times. I regret not having had more opportunities to spend additional time with him, especially considering our shared experiences as team members. I appreciate your effort to improve my French level. I extend my best wishes to you for the years ahead.

I want to appreciate my friends, who are the silent heroes of my Ph.D. journey. I am fortunate to have met **Anam, Amitayush, Hamza, Xiao, Kokouvi, Dylan, Souhail, Yimin, Peng** in France. I am thankful to my friends from India **Arijit, Anupam, Dipanjan, Swadesh, Sukesh, Sudipta, Subrata, Bithika** for being a constant source of support. I have had wonderful times with **Dr. Nishith MAITY**. I am grateful for the support and friendship we have shared, and my best wishes will always be with you.

The support from ISMO mechanical and electrical teams was always crucial during my research days. My sincere thanks to **Jérôme GUIGAND, Jean-Philippe DUGAL, Sylvain LUPONE, Marc ALBARET, Chrstophe CHARRIERE and Julien VINCENT** for their assistance. I take the opportunity to thank all the administrative members of ISMO **Nathalie BAUDRY, Sylvie CHABOT, Frédéric DURRAND, Aïssata BA, and Véronique SARRAZIN** for their help. Despite my non-French speaking background, I have not encountered any problems as they always made an effort to address any of my issues.

I am thankful to my former laboratory colleagues, **Dr. Badri VISHAL** and **Dr. Sharon HORTA**, for their invaluable support throughout my pre-Ph.D. journey and for being a constant source of motivation.

I would like to take this moment to appreciate my teachers and professors in India. **Dr. Pabitra Kumar CHAKRABARTI, Dr. Jayanta MANDAL, Dr. Chanchal GHOSH** have consistently provided unwavering support and invaluable motivation that helps me every step of the way.

While living in France, **Madhan** and his family have helped me consistently, and I consider them an integral part of my own family. I had wonderful times and have special memories with his family.

I am thankful to **Science Accueil** for the support and assistance over the past three years.

I want to extend my gratitude to my landlord **Mr. Gérard OUTREQUIN** and his wife **Mrs. Lisa OUTREQUIN**. For the last three years, they have been remarkably helpful and tried to resolve all sorts of problems that came up.

Transitioning towards my personal expressions of gratitude, I would like to express my profound gratitude to my parents for their immeasurable support, guidance, love, and sacrifices throughout my life. I am profoundly thankful to my extended family members for their encouragement and unwavering belief in me, which has been a source of my strength.

With this, I want to conclude my acknowledgments by expressing my heartfelt gratitude to everyone I have had the opportunity to meet throughout my life, as they have generously shared invaluable wisdom with me.

Thank You (*merci beaucoup!*)...

Arindam

2023

Résumé

Les techniques de dépôt de couches minces ont évolué au cours des dernières décennies et sont classées en deux grandes catégories : le dépôt physique en phase vapeur (PVD) et le dépôt chimique en phase vapeur (CVD). La pulvérisation magnétron (MS) est l'une des méthodes PVD largement utilisées dans la recherche et l'industrie.

Le suivi en temps réel de la croissance des couches minces est l'un des problèmes les plus critiques, car les paramètres de croissance influencent directement la morphologie du film et donc ses propriétés finales. Ce problème est encore plus complexe dans le cas de la pulvérisation magnétron (MS) en raison de la présence inhérente de champs électromagnétiques (EM) dans la zone de dépôt. C'est donc un défi d'adapter des outils de diagnostic structural utilisant des particules chargées, comme le RHEED (Reflection High Energy Electron Diffraction). L'autre possibilité consiste à utiliser les rayons X en incidence rasante afin d'améliorer la sensibilité à la surface. Cependant, cette géométrie nécessite un flux élevé de rayons X, principalement disponible dans les installations de rayonnement synchrotron, ce qui exclut cette méthode du champ des techniques de laboratoire.

L'objectif de la thèse est de combler cette lacune en matière de recherche en développant une technique de laboratoire efficace qui peut être intégrée à la MS pour contrôler la croissance en temps réel de couches minces. Les travaux sont divisés en trois phases.

La première phase implique la conception et la mise en œuvre d'une nouvelle configuration (HP-GIFAD) qui permet le fonctionnement de la diffraction d'atomes rapides en incidence rasante (GIFAD) à hautes pressions (supérieures à 10^{-6} mbar). GIFAD est une technique sensible aux surfaces et non destructive, considérée comme un complément/alternative au RHEED, utilisée pour suivre en temps réel la croissance de couches minces dans des conditions de vide poussé (de l'UHV à 10^{-6} mbar). Le fonctionnement de GIFAD à des pressions supérieures à 10^{-6} mbar pose de nombreux problèmes tels que l'atténuation du faisceau, la perte de cohérence du faisceau due aux collisions en phase gazeuse et un bruit excessif sur le système de détection à galettes de microcanaux. Grâce à un schéma compact avec un système de double pompage différentiel, nous démontrons que le fonctionnement du GIFAD peut être obtenu à des pressions d'Ar jusqu'à 10^{-2} mbar. A cette pression et au-delà des attentes, le diagramme de diffraction est toujours bien résolu, malgré une atténuation substantielle du faisceau.

La deuxième phase de nos recherches implique l'étude fondamentale des propriétés du faisceau diffusé en régime haute pression (au-dessus de 10^{-6} mbar). Cette étude est mise en perspective avec l'investigation plus générale de la décohérence des systèmes quantiques en interaction avec un environnement. L'interprétation largement acceptée repose sur l'intrication irréversible entre le système quantique et l'environnement via l'échange de quantité de mouvement. Dans la configuration HP-GIFAD, malgré une forte atténuation du faisceau dans la région à haute pression, seule une décohérence mineure induite par l'interaction du paquet d'ondes avec les atomes d'Ar environnants a pu être quantifiée ; elle est associée à un rétrécissement anormal des pics de Bragg qui dépend fortement de la largeur de co-

hérence du faisceau primaire. Un tel rétrécissement n'est pas compatible avec une description classique du processus de collision.

Dans la troisième phase de nos travaux, nous nous sommes concentrés sur l'intégration de HP-GIFAD dans un système de dépôt par pulvérisation magnétron impulsionnelle de haute puissance (HiPIMS), une variante récente de MS. HiPIMS offre de nombreux avantages, parmi lesquels des films plus denses et une meilleure cristallinité, au prix d'un grand nombre de paramètres ajustables. La combinaison de HiPIMS et HP-GIFAD apparaît non triviale en raison des atomes d'Ar métastables à longue durée de vie produits par les impulsions plasma (durée de 20 à 50 μs). Ces métastables finissent par se frayer un chemin vers le détecteur et produisent un niveau de bruit inacceptable. Nous avons pu parvenir à un fonctionnement satisfaisant en utilisant un système de pulsation du détecteur, rendant ainsi HP-GIFAD entièrement compatible avec HiPIMS.

L'objectif ultérieur était d'identifier et d'établir les conditions optimales pour suivre en temps réel la croissance de couches métalliques sur des surfaces isolantes. Les résultats préliminaires sur le dépôt HiPIMS de Cu sur NaCl (001) sont prometteurs. Nous prévoyons qu'en ajustant les paramètres de dépôt (puissance d'impulsion, accélération des ions pulvérisés, etc.), le mode de croissance par îlots observé dans des conditions standard évoluera vers une croissance en couche par couche. Cette preuve de concept sera ensuite étendue à la croissance d'oxydes fonctionnels, avec un accent particulier sur le dioxyde de titane (TiO_2) et le dioxyde de vanadium (VO_2).

List of Figures

1.1	<i>A schematic of the initial stage of three growth modes. Θ is the surface substrate coverage in monolayers (ML).</i>	17
1.2	<i>Schematic of the universality of GIFAD technique.</i>	20
1.3	<i>Schematic of experimental GIFAD setup having GIFAD source and detector mounted on an MBE deposition system.</i>	21
1.4	<i>Normalized intensity oscillations during GaAs growth at different substrate temperatures. (b) Intensity oscillations of the first few monolayers for initial surface reconstruction (2×4) (black/gray) and c(2×4) (red). Vertical lines are showing the formation of 2.3, 2.8, and 3.3 MLs deposition correspond to maxima and minima of the intensity oscillations at 570° C.</i>	22
2.1	<i>Schematic of the diffraction condition of a wave packet of transverse length L_c interacting with a surface having period d.</i>	26
2.2	<i>(a)-(b) Photograph of the charge exchange cell with its different stages.</i>	28
2.3	<i>A schematic of the main chamber and the detector with the different components.</i>	29
2.4	<i>Schematic drawing of the prototype differential pumping system.</i>	30
2.5	<i>a) Configuration of the multi-tube differential pumping system: each tube is equipped with a cap of having a small aperture. (b) Entrance aperture to the first tube, Kapton tape is used to reduce the aperture size, (c) evolution of the pressure ratio between the UHV chamber and the detector chamber as a function of the number of stages, a stage is considered active when the apertured cap is mounted.</i>	31
2.6	<i>The image of the Extorr RGA with CCU box compatible with DN 40 CF.</i>	32
2.7	<i>RGA spectra at 3×10^{-8} mbar of pressure. Taken from HP-GIFAD UHV chamber.</i>	33
2.8	<i>Sputter ion gun configuration with different components.</i>	33
2.9	<i>(a) Top view and (b) front view of the UHV side of manipulator.</i>	34
2.10	<i>Configuration of the shield and shutter inside the UHV main chamber.</i>	35
2.11	<i>(a) Introduction chamber to transfer the sample, (b) wobble stick trigger grip to hold the sample.</i>	35
2.12	<i>Configuration of the detector comprises of Microchannel Plates and phosphor screen and CCD camera.</i>	36
2.13	<i>The ‘Photonis’ detector having (a) UHV side and (b) air-side with feed-throughs, the air-side of the fiber optic screen is clearly visible.</i>	37
2.14	<i>Schematic of scattering geometry in GIFAD.</i>	38
2.15	<i>Left side : 3D corrugated surface $V(x, y, z) = 3$ eV of He atom at LiF(001) surface , arrow indicates the direction for averaging of $V(x, y, z)$ along $\langle 110 \rangle$. Right side: 2D corrugated surface of $V(y, z) = 3$ eV.</i>	39

2.16	<i>Grazing scattering of He atoms from the topmost layer of the surface. Due to the very low energy in the direction normal to the surface, the atoms are scattered above the first atomic plane.</i>	39
2.17	<i>(a) LiF(001) surface and two directions are shown here, (b) Diffraction of He atoms from LiF(001) surface along <100> direction.</i>	41
2.18	<i>Classical trajectories of deflected atoms after the interaction with the corrugation of the surface. The flat portion of the corrugation (bottom and top points, A and B trajectories), produces zeroth order and the deflection from different slopes gives nth order of the Bragg peaks.</i>	42
2.19	<i>Top: He atom diffraction at 400 eV from c(2×2) reconstructed ZnSe(001), along <1-10>, <110> and <100>. Bottom: Corrugation extracted from diffraction intensities along three directions.</i>	44
2.20	<i>Schematic of the main chamber of HP-GIFAD. The entrance and exit tubes are T_{in} and T_{out}. The distance between them $l_2 = 65$ mm. LiF(001) surface is shown in blue color.</i>	45
2.21	<i>He atom diffraction along the <100> direction from LiF(001) surface at (a) 10^{-8} mbar and (b) 3.6×10^{-3} mbar and along the <110> direction at (c) 5.6×10^{-9} mbar, and (d) 8.9×10^{-3} mbar of Ar pressure. (e) shows the projected intensities, from 2.21(a) and 2.21(b), contained between the two Laue circles superimposed on the images. (f) normalized projected intensities from (e).</i>	46
2.22	<i>Intensity decay of (a) the direct beam and (b) the scattered beam along the <100> direction; the semi-log plots are shown in the insets [$\ln(\text{Intensity})$ vs. pressure].</i>	47
2.23	<i>(a) Normalized Gaussian distribution of the direct beam and the horizontal line is the intensity at $\frac{1}{e^2}$ of the maximum intensity. The data corresponds to the base pressure (10^{-8}) mbar, (b) evolution of divergence of the gaussian beam with pressure.</i>	48
2.24	<i>Scattered beam intensity from LiF(001) surface before and after the experiment. Diffraction images were captured at 10^{-8} mbar of pressure.</i>	49
3.1	<i>He atom diffraction from LiF (001) surface along the <100> direction at (a) 10^{-8} mbar, (b) 3.6×10^{-3} mbar and (c) projected intensity of (a) fitted with Pseudo Voigt function.</i>	54
3.2	<i>The main chamber of the HP-GIFAD setup with different zones is considered in the discussions. T_1 and T_2 are the entrance and the exit tubes with diameters 150 μm and 4 mm respectively. The LiF(001) sample is shown in blue color.</i>	55
3.3	<i>Zoom-in view of zone 2 and 3.</i>	56
3.4	<i>Single and double exponential fitting of coherent fraction data.</i>	56
3.5	<i>(a) Decay of coherent fraction and (b) behavior of Lorentzian width with pressure. $1\text{\AA}^{-1} = 0.06^\circ = 1.04$ mrad. Data is shown here for 60 μm slit size.</i>	58
3.6	<i>Polar distribution fitted with Lorentzian and Log-normal profile. Spectrum is at 10^{-8} mbar.</i>	59
3.7	<i>Dependency of the Lorentzian width with Ar pressure along the polar direction</i>	60
3.8	<i>Schematic of He atom scattering from surface adsorbates.</i>	60
3.9	<i>Deposition of perylene on Ag (110) surface. (a) Time evolution of scattered beam intensity from Ag(110) surface along <1-10> direction during perylene deposition, (b) variation of the reflectivity from the surface over the deposition time. Experiments were performed at 500 eV energy of He atom. ML: Mono Layer.</i>	61
3.10	<i>(a) He atom diffraction from Ag(110) along <1-10> direction, (b) normalized fitted diffraction spectrum projected in between Laue circles.</i>	62
3.11	<i>(a) Decay of coherent fraction (b) evolution of Ag peak width with deposition time.</i>	62

3.12	<i>Deposition of KCl on Ag (001) surface. (a) Time evolution of scattered beam intensity from Ag(001) surface along <110> direction during KCl deposition, (b) variation of the reflectivity from the surface over the deposition time of KCl.</i>	63
3.13	<i>(a) decay of coherent fraction over the KCl deposition time and (b) behavior of the Lorentzian width during the deposition time.</i>	63
3.14	<i>Comparison of the (a) variation of peak width and (b) decay of coherent fraction with pressure with different slit sizes.</i>	64
3.15	<i>Decay of relative coherent fraction with relative intensity for 60 μm slit width. The dotted line is used to guide the eyes.</i>	65
3.16	<i>Optical Talbot effect using monochromatic light and the Talbot carpet. The revival of the images happen at the integer of Talbot length at the right.</i>	66
3.17	<i>Evolution of near field region with the number of slits, $N=(a)1, (b)2, (c)4, (d)8, (e)12, (f)20$. Zoom in near field regime is shown in insets (a) and (b). The triangle area in (f) exhibits the internal area of the near-field interference pattern; the near filed region is a few tens of talbot length.</i>	67
3.18	<i>Talbot carpet formation with different number of slits, (a) $N=1, (b) N=2, (c) N=3, (d) N=10$ and (e) $N=50$ are shown in left panel and right side are the quantum trajectories according to the left panels. X is the distance scaled in units of the grating period d, and z is terms of Talbot length ($2L_T$)</i>	68
4.1	<i>Several regions in the DC glow discharge appears between cathode and anode.</i>	74
4.2	<i>Distribution of voltage in a DC glow discharge. In this hypothetical case, 1000V is applied on the cathode, and the anode is grounded. Here V_p is the plasma potential.</i>	74
4.3	<i>Different inelastic processes are depicted here.</i>	75
4.4	<i>Current-voltage characteristics of direct current (D.C.) electrical discharges</i>	76
4.5	<i>Interactions of an ion with a surface.</i>	79
4.6	<i>Cross-sectional view of (a) planar circular magnetron and (b) top view with central and annular disc, (c) Cu sputtered target with a race track having heavy erosion.</i>	81
4.7	<i>Types of magnetron configurations, a- conventional balanced magnetron, b- unbalanced magnetron I, and c- unbalanced magnetron of the type II.</i>	82
4.8	<i>(a) DC mode and (b) HiPIMS mode discharge. Both images were taken in ISMO magnetron reactor mounted on the high-pressure GIFAD chamber. A two-inch Cu target is used here.</i>	84
4.9	<i>Current-voltage characteristic during the discharge of HiPIMS, Pulse duration 20 μs and frequency 200 Hz. Here an one-inch Cu target is used.</i>	84
4.10	<i>(a) Noise on the detector in the presence of plasma and (b) schematic of the deflector system mounted on the ConFlat (CF) UHV 5-way cross.</i>	86
4.11	<i>(a) Three different samples attached on the deflector plate, (b) Noise on the detector.</i>	86
4.12	<i>Schematic of HiPIMS pulse and delay between the pulse and the detector time gate.</i>	87
4.13	<i>Variation of noise with the delay between HiPIMS pulse and detector time-gate.</i>	88
4.14	<i>Condition of the He atom beam with and without plasma, (a) without the filament the ignition pressure is 2.2×10^{-2} mbar and (b) with filament the pressure is 3.2×10^{-3} mbar.</i>	89
5.1	<i>(a) iPhone 12 gold coated with HiPIMS, (b) hip and knee replacement materials coated using HiPIMS deposition[Taken from Sheffield Hallam University webpage].</i>	92

5.2	(a) Diffraction of He atoms at 500 eV energy from NaCl(001) surface along $\langle 110 \rangle$ direction. He atoms scattered at 500 eV of energy from NaCl, (b) HiPIMS discharge for the deposition of Cu, a voltage of 700V is applied for 30 μ s to the cathode.	93
5.3	(a) Intensity distribution observed after deposition and annealing at 150 °C at (a) 894 eV of energy and (b) at 394 eV of energy, (c) is the projection of (b) along the polar direction shows a sharp peak, considered as an elastic peak.	94
5.4	Normalized scattered beam intensity over the deposition time of Cu.	95
5.5	Scattered beam intensity at different stages according to the reflectivity curve (Fig.5.4).	96
5.6	(a) and (b) are the SEM images at two different magnifications. Magnification of (a) is \sim twice of (b).	96
B.1	Schematic of a binary collision. The blue dot is the projectile, and gray dot is the target atom.	102

List of Tables

1.1	<i>Summary of different techniques used for characterization of surface and composition of the surface layer.</i>	19
4.1	<i>Typical parameters during DCMS and HiPIMS discharges.</i>	83
A.1	<i>Comparison table of LEED, RHEED, TEAS, and GIFAD.</i>	101

Chapter 1

Introduction

1.1 Surfaces and interfaces: History, definition, importance

Surface science is the product of a combination of science and technology. Within the context of 'Surface Science,' the objective is to understand and interpret the structure and properties of the surfaces, interfaces, and dynamics of chemical reactions at the surface. However, the fine observation of the surface and its control were the road map to technological advances. The invention of Ultra High Vacuum (UHV) technologies in 1960-70 had an immediate consequence on the development of electron spectroscopy techniques based on electron-solid interaction. Over the years, surface science has been enriched by the development of many surface diagnostic techniques using mainly charged particles (electrons and ions) or photons (from IR to X-ray). Hence, the understanding of the surface requires a broad knowledge of chemical bonds, particle-surface interactions, etc., and it becomes an interdisciplinary research area. All the developments in surface science can be categorized into four different timelines.

The first revolution happened in the 1960s with the emergence of UHV systems and electron spectroscopy techniques. At the beginning of the 1980s, the rise of semiconductor microelectronics helped to build sophisticated experimental probes of surfaces. The age of imaging of the surface received maturity in the 1990s. The discovery of scanning microscopes helped to image the surface and to understand the growth, deposition, and chemical reactions. The fourth stage is the application of surface science techniques to understand more complex systems like biological systems and liquid-solid interfaces[1].

The properties of a surface are different from the properties of bulk materials. The definition of the surface can be framed as an intimate interface of another phase (solid, liquid, gas); accordingly, the surface can be considered as 2-10 atomic or molecular layers (1-3 nm). However, some technological requirements need thick layers (up to 100 nm). Generally, above few nm (~ 10 nm) bulk properties dominate.

A thin film is described as a material layer having a thickness ranging from a few nanometers to several micrometers. The fundamental steps behind the application of thin films are hidden behind the controlled growth mechanism.

There are several processes involved in the growth of materials, and the sputter deposition technique has gained visibility over the last few decades as one of the widely used methods. Sputtering is the ejection of surface particles due to the bombardment of energetic particles (energetic ions or neutrals, both co-exist in laboratory discharge plasma).

Coating technology has drawn attention in today's world due to the development of advanced systems in different areas. For example, the high-temperature blades of gas turbines are expected to work at high temperatures and must be corrosion-resistant. In this condition, the coating technology gives mechanical stability, wear resistance to the system.

Although the term 'coating' has gained popularity over the last few decades, the methodology of making coating is relatively old. After the discovery of gold (~ 11000 years ago), it has been given special importance in the human history. The first documented inorganic thin gold layers ($< 3000 \text{ \AA}$) were done by Egyptians almost 5000 years ago. The coatings were generally done by Egyptians using chemi-mechanical processes[2].

Today, thin film coatings have a broad range of applications in several areas, like superconducting technology[3], magnetic memory[4], semiconductor devices[5], optical coatings[6], hard coatings (for cutting tools, aerospace, automotive etc.) [7], energy generation (thin film photovoltaics)[8], energy storage (thin film batteries)[9]. Hence, the utilization of thin film coatings remarkably contributes in the modern science. Also, thin films have a significant impact on various aspects of daily life like electronics, energy generation, optics and displays, medical purposes etc.

The consumption of energy is elevating due to the population rise, which desperately increasing burdens on the environment, especially on the global climate. Due to the shift towards the clean energy resources, the term 'renewable energy' or 'green energy' has become a multidisciplinary and international forum for research in basic science. Photovoltaics now have a rapid growth in a subsidized market and the industries are gearing up for the large-scale production. Thin Film Photovoltaics (TFPV) is one of the promising fields of research now a days and the cost of producing thin-film photovoltaics are the lowest among the current alternative technologies but the attention must be drawn to the toxicity[10] of materials used in production for the manufacture (Pb, Ge, Te, Se etc.).

The subject of thin film deposition has a considerable interest, and diverse techniques are involved in the production of these films. The next section will give a partial overview of the several deposition methods without elaborating in detail.

1.2 Thin-film deposition technologies

Deposition of a thin layer refers to several monolayers of material, or more, with a chemical composition generally different from the surface material. The growth of a thin film is the succession of monolayers one on the top of the other (typically 10 monolayers correspond to a film of about 3 nm thickness) on a surface. This surface can be a pure substrate or a previously deposited layer (for multilayers). The property of the initial material is changed by depositing a thin layer of a material, for example, hardness, electrical conductivity, and optical properties of the substrate.

There are several ways of depositing thin films, but the methods are broadly classified into two large categories: 1. Physical Deposition and 2. Chemical Deposition. In Physical Deposition, the atoms or molecules of the source materials (often solid, but could be liquid as well) pass in the gas phase (vapors) due to providing a considerable amount of energy. The origin of this energy often gives the name of the technique such as evaporation (thermal or electron beams), sputtering (ions or plasma), ablation (lasers), etc. Chemical Deposition relies on the chemical reaction of vapor species containing thin film ingredients on the substrate to produce a film of desired composition. Often the precursors in chemical methods are gaseous or liquids and they contain the elements of the material to be deposited. The other undesired chemical constituents are often eliminated in gas phase.

Physical Deposition usually requires High Vacuum (HV) or Ultra-High-Vacuum (UHV) conditions to avoid contamination on the layers, while Chemical Deposition happens even in atmospheric pressure.

1.2.1 Physical Deposition

The physical deposition method generally uses a solid source of matter and energy to bring this material directly from the solid to the vapor phase. In this context, it is said 'Physical'. A typical example is a heated metal (by e^- beam, for instance) that locally vaporizes and produces metal vapor, which condenses onto the available surface. Hence a thin metal film is grown on the surface. However, a rarefied atmosphere is used (O_2 or N_2) to grow oxide or nitride films.

There are several ways to produce vapor:

1.2.1.1 Vacuum evaporation

High-purity films are deposited using Molecular Beam Epitaxy (MBE)[11] methods in UHV conditions. The UHV conditions help to grow a better quality film. Indeed, the mean free path of species (metal vapors) becomes larger than the typical dimension of the deposition chamber, and so the vapor species can reach the substrate practically without interaction with any other species, producing a high-purity film. One major limitation of MBE is its limited deposition rate. Vacuum evaporation is possible for a wide range of materials. The deposition is achieved by evaporating the precursors kept in crucibles.

in the case of thermal evaporation. A modern alternative is the direct and local evaporation of a solid target by focusing an energetic electron beam. Hence it heats up only very locally ($< 100 \mu\text{m}$) the solid beyond the evaporation temperature, generating a point source of vapors. The latter is known as e^- beam evaporation. The vapor pressure is raised to a point where the sublimation or evaporation happens. Generally, it has been considered that the vapor flux is unidirectional as the residual pressure of the system is low. So, scattering from the residual species is negligible. The vapor species arrived on the substrate and condensed to produce the desired film.

1.2.1.2 Sputter deposition

Sputter deposition is a deposition technique of thin film using sputtering. Sputtering is a process of ejecting materials from a solid surface (target) by energized ions (usually inert gas ions or highly energetic neutrals (few hundred eV)). These ejected atoms have energy of a few eV with a tail up to tens of eV.

The ejected particles, after sputtering, are by far dominant neutral. In the case of High Power Impulse Magnetron Sputtering (HiPIMS) (**Chapter 4**), most of these metal neutrals get ionized inside the ionization region, and the discharge voltage (electric field) accelerates them back toward the target. So, they usually arrive at the cathode (target) with an energy that is close to the discharge voltage (several 100 eV). So, they can sputter the target. This phenomenon is called self-sputtering being induced by the ions of the same element as the target.

To have a good condition of sputtering the atomic mass of sputter species (gas ions) must be close to the target atoms to achieve an efficient momentum transfer. Generally, Ar is used to make sputtering.

There are several commercially available techniques based on sputtering like ion-beam sputtering[12], ion-assisted deposition[13], High Target Utilization Sputtering (HiTUS) [14], High Power Impulse Magnetron Sputtering (HiPIMS)[15] etc.

In **Chapter 4**, a detailed description is given about the Magnetron Sputtering (MS) process, especially on HiPIMS.

1.2.1.3 Pulsed Laser Deposition (PLD)

Pulsed Laser Deposition (PLD)[16] is a physical deposition process where a highly powered pulsed laser beam is focused on a source material inside a vacuum chamber. The source material is then vaporized from the target as a plasma plume and deposited on a substrate as a thin layer. The PLD depositions occur in UHV or high vacuum conditions in the presence of some background gas (to grow oxide, O_2 is used).

The process of laser-target interaction is quite complicated. However, the whole process can be categorized into four steps: evaporation, ablation, plasma formation, and deposition on substrate.

Remarkable laser technology helps to grow thin films of different materials, like high-temperature superconducting alloy ($\text{YBa}_2\text{Cu}_3\text{O}_7$)[17]. The PLD technology of deposited thin film $\text{YBa}_2\text{Cu}_3\text{O}_7$ is superior in quality compared to other alternative methods.

1.2.1.4 Cathodic Arc Deposition (arc-PVD)

Arc-PVD is a physical deposition process, where the process of vaporizing material from a cathode surface is happened due to the electric arc. Cathodic arc[18] is a low-voltage and high-current discharge that takes place between two electrodes under vacuum.

Generally, arc-PVD is used to make hard coatings nowadays. The hard coating as an example, coating of titanium nitride (TiN), chromium nitride (CrN), and aluminum chromium titanium nitride (AlCrTiN), protects the surface of cutting tools from wear and fatigue.

1.2.2 Chemical deposition

In the chemical deposition, the precursor material undergoes a chemical reaction on the substrate surface and creates a thin layer. Thin films deposited using chemical ways are said to be conformal, rather than directional.

There are several ways of doing deposition of thin films using chemical deposition root like electroplating[19], spin-coating[20], dip-coating[21] and Chemical Vapor Deposition (CVD)[22]. The CVD method is the most popular among all the chemical deposition methods and is discussed briefly in the following subsection.

1.2.2.1 Chemical Vapor Deposition (CVD)

CVD is a vacuum deposition process where the substrate surface is exposed to volatile precursors, and the reaction between precursors helps to grow a thin film. It has been observed that the by-products made from the reaction are removed by the gas flow process, and high-quality thin films can be grown.

There are several variants of the CVD process based on the initiation process of the chemical reaction. For example, Atmospheric Pressure CVD (APCVD), Ultra High Vacuum CVD (UHVCVD), Plasma enhanced CVD (PECVD), Atomic-layer CVD (ALCVD), Metal-organic CVD (MOCVD), Atomic Layer Deposition (ALD) etc.

Nowadays, CVD techniques are the most commercially used thin film deposition techniques. ALCVD is used to grow high-quality thin layers, useful for integrated circuits (ICs) and photovoltaic devices. Also, CVD is used to produce artificial diamonds or synthetic diamonds[23] from a hydrocarbon mixture, the most abundant materials on earth.

1.2.3 Different thin film growth modes

The formation of thin films by vapor deposition is a classic case of heterogeneous nucleation, where the condensation of adatoms happens on a substrate that is composed of atoms different from the vapor. The growth of thin films is classified into two parts: growth of the nuclei and their growth. Depending on the interaction energies between surface atoms and the adatoms from the vapor, any of three growth modes can occur:

1. **Layer by layer-** This growth mode is also known as the Frank-van der Merwe growth mode and is considered as two-dimensional growth. In this case, the interaction between substrate and film atoms is greater than between adjacent film atoms.
2. **Island-** It is known as Volmer-Weber mode, where three-dimensional separate islands are formed on the substrate. In this scenario, the interaction between adjacent film atoms is stronger than the film and surface atoms.
3. **Layer plus Island-** Also known as Stranski-Krastanov mode. This growth begins with one or two monolayers from first, followed by islands.

A schematic of the initial stage of three growth modes is depicted in Fig.1.1.

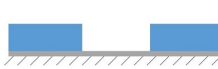
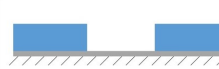






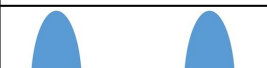
	Frank- van der Merwe	Stranski- Krastanov	Volmer- Weber
$\Theta < 1 \text{ ML}$			
$1 \text{ ML} < \Theta < 2 \text{ ML}$			
$\Theta > 2 \text{ ML}$			

Fig. 1.1: A schematic of the initial stage of three growth modes. Θ is the surface substrate coverage in monolayers (ML).

1.2.4 Thin film and surface characterization

To probe a medium, here a solid surface, different probes are used. The probes can be electrons, ions, neutrals, either photons or electric fields. By changing the mass, energy, or character of the probes, different possible experiments can be performed, and useful information, i.e., structure (electronic and physical) and the surface compositions (chemical), can be obtained. Surface characterization usually needs physical imaging, which can be divided into two parts. 1. Direct Physical Imaging (SEM, TEM, STM), and 2. Indirect Physical Imaging (LEED, RHEED, XRD). Here, direct physical imaging means

information obtained in real space, and indirect physical imaging defines information obtained in reciprocal space. A comparison of different characterization techniques is listed below.

Incident probe	Analyzed response		
	Electrons	Ions/Neutrals	Photons
Electrons	Auger Electron spectroscopy(AES) Scanning electron microscopy (SEM) Transmission electron microscopy (TEM) Low energy electron diffraction (LEED) Reflection High energy electron diffraction (RHEED) Electron Energy Loss Spectroscopy (EELS) in TEM	Electron stimulated desorption (ESD)	Energy dispersive analysis of X-rays (EDAX) Photoluminescence in TEM (TEM/PL)
Ions		Low Energy Ion Scattering Spectroscopy (LEIS) Rutherford backscattering spectroscopy (RBS) Secondary ion mass spectrometry (SIMS)	
Photons	X-ray photoelectron spectroscopy/Electron spectroscopy for chemical analysis (XPS/ESCA). Ultra-violet photoelectron spectroscopy (UPS). Extended X-ray absorption fine structure (EXAFS)	Photon stimulated desorption (PSD)	Raman vibrational spectroscopy (Raman), Fourier transform infrared spectroscopy (FTIR) Near Edge X-ray Absorption Fine Structure (NEXAFS) Fluorescence spectroscopy Laser-induced breakdown spectroscopy (LIBS) Spectroscopical Ellipsometry
Tip	Scanning tunneling microscopy (STM). Atomic Force Microscopy (AFM)		
Neutrals		Thermal Energy Atom Scattering (TEAS). Grazing Incidence Fast Atom Diffraction (GIFAD).	

Table 1.1: Summary of different techniques used for characterization of surface and composition of the surface layer. Taken from [24].

In this thesis, the characterization tool GIFAD is used for the surface structure analysis and to retrieve the fundamental information. In this technique, a neutral He atom is used as a probe, having energy 0.2-5 keV, which scatters from the surface under grazing conditions. The grazing geometry makes it suitable to have a better surface sensitivity compared to RHEED or LEED. GIFAD has been used extensively over the past few years to characterize different types of material, as shown in the schematic below.

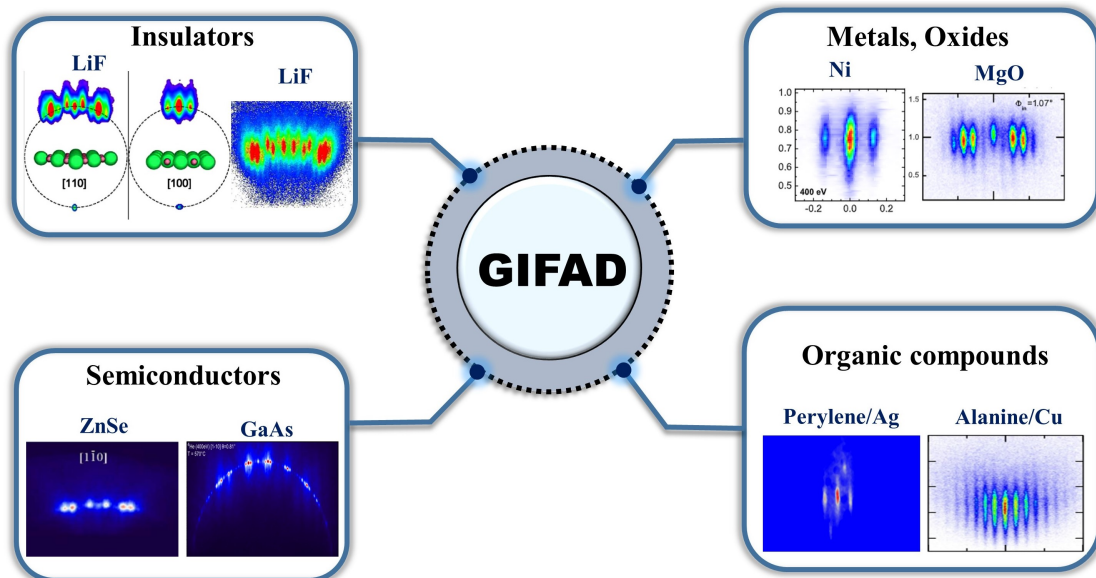


Fig. 1.2: Schematic of the universality of GIFAD technique. Diffraction images are taken from [25, 26, 27, 28, 29, 30, 31].

1.2.5 Different *in-situ* techniques for thin film growth

Thin films are the key element of research due to their different properties from bulk materials. The fundamental research and application of thin films using a huge variety of deposition techniques is expected to remain an area of research interest for the upcoming decades. The high demand for miniaturized devices and nanotech has motivated researchers to improve the quality factor of the thin layers.

The properties of the thin films are dependent on several parameters, thickness of the layer, substrate condition, and growth parameters. So, it is always important to have control of the growth and the film properties in real-time. Thus, different *in-situ* techniques have been evolved to follow and control the growth process.

Various deposition methods have already been discussed in section 1.2.1. Generally, RHEED has been adapted successfully with MBE and later with PLD [32], and ALD[33]. Also, using the optical properties of thin films, the ellipsometry technique is used to deduce *in-situ* information[34]. The ellipsometry method is preferred for ion beam-assisted deposition, MS, or plasma-based deposition due to the insensitivity to the electromagnetic field and to avoid charge-up of the substrate.

Grazing Incidence Small Angle X-ray Scattering (GISAXS) is used to follow the real-time growth in

synchrotron facilities[35].

Structural changes during growth provide stress in the thin layers, depending on the thickness of the film. Generally, the origin of stress is the lattice mismatch between the substrate and the thin film. XRD, Raman, and infrared spectroscopy are ex-situ methods to measure the stress. Real-time stress measurement of the thin films can be done using a multi-beam optical sensor (MOSS) developed by Sandia National Lab and k -space Associates. The basic principle is that thin film under stress conditions will produce a curvature κ in the underlying substrate. By knowing the thickness of the film and substrate, the elastic modulus of the substrate, and the initial curvature of the substrate before starting the growth, the stress can be evaluated [36].

GIFAD has shown its credibility to follow the real-time growth in UHV condition in MBE deposition[37] system. The advantage of GIFAD compared to RHEED is hidden in the sensitivity. Although the primary energy of the beam can be up to keV, the grazing scattering of the He atom from the surface constrained the energy normal to the surface in the meV to few eV range. This prevents the penetration of the He atom below the first atomic planes. The scattering of the He atom at a few Å above from the topmost layer makes GIFAD more sensitive to the surface and surface corrugation (more description in **Chapter 2: 2.3.1**). This helps to identify the low-index crystallographic direction easily. In the case of RHEED, the phase and magnitude of growth oscillations depend on the scattering geometry, where GIFAD is only sensitive to the surface conditions and a robust *in-situ* method to monitor 2D growth.

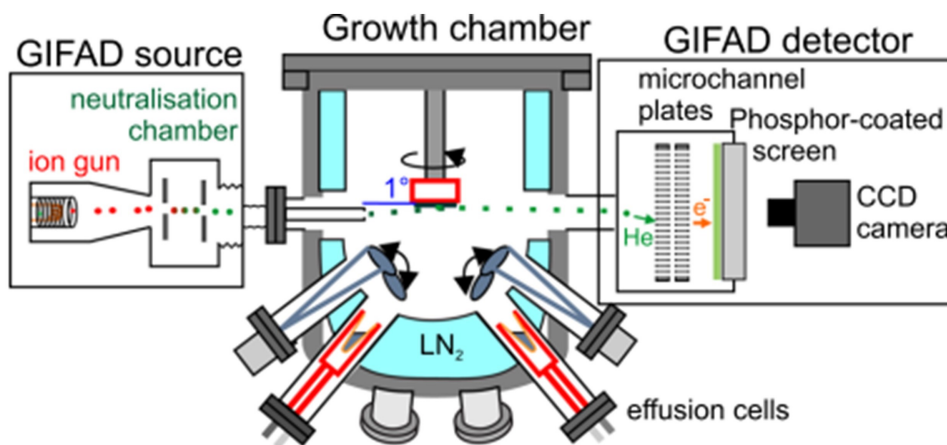


Fig. 1.3: Schematic of experimental GIFAD setup having GIFAD source and detector mounted on an MBE deposition system. Taken from [12].

Generally, the scattered beam intensity is traced over the deposition time. The surface is pretreated and prepared by annealing or by a combination of sputtering and annealing. At the beginning, the surface is clean (adsorbate-free) and flat, which produces a high intensity of the scattered beam. However, during the course of deposition, the reflectivity drops due to the physisorption of the deposited species. But as soon as the full coverage is achieved and it is flat, the reflectivity recovers and reaches the maximum. This phenomenon continues, and several oscillations appear during the deposition. So, basically, one complete

layer is defined by the one complete oscillation in the reflected intensity. In this way, the number of layers can be controlled using GIFAD. However, when there is a change in surface reconstruction at the start of the growth, GIFAD intensity oscillations show that there is a delay in the layer-by-layer growth. An example of homoepitaxial growth of GaAs is shown below.

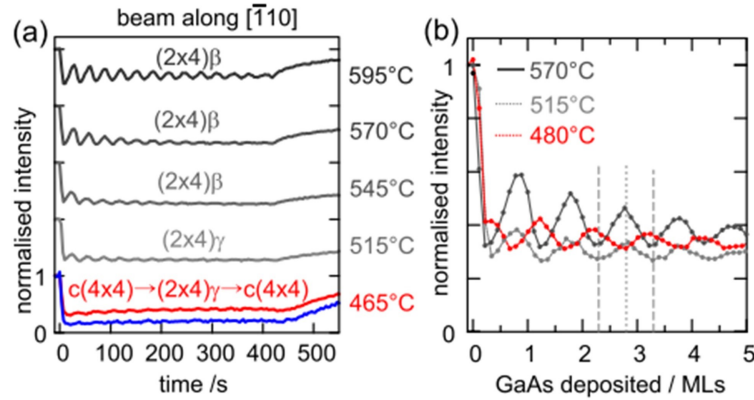


Fig. 1.4: Normalized intensity oscillations during GaAs growth at different substrate temperatures. (b) Intensity oscillations of the first few monolayers for initial surface reconstruction (2×4) (black/gray) and $c(2 \times 4)$ (red). Vertical lines showing formation of 2.3, 2.8, and 3.3 MLs deposition correspond to maxima and minima of the intensity oscillations at 570°C. Taken from [37].

1.3 Overview of the thesis

This thesis aims to develop a technique to monitor the thin film growth in real-time using the Magnetron Sputtering (MS) deposition method. This involves developing a novel GIFAD setup to make it compatible with high-pressure environment ($> 10^{-6}$ mbar), exploring and understanding the high-pressure regime, and combining this high-pressure GIFAD system (HP-GIFAD) with Magnetron Sputtering (MS) to control the thin film growth in real-time.

The chapters of the thesis have been organized as follows: **Chapter-2** describes the instrumental components of the HP-GIFAD system, basic operational principles, and experimental results of HP-GIFAD. **Chapter-3** gives the perspectives of the exploration of collisional decoherence and how the quantum scattering from the surface shifts towards the classical scattering with the pressure due to the interactions with Ar gas environment. **Chapter-4** covers the fundamentals of plasma and sputtering, with a focus on HiPIMS. It describes how the high-pressure GIFAD system is adapted to the MS technique with the initial challenges. **Chapter-5** outlines the first outcomes of depositing Cu on an insulator substrate (NaCl) using HiPIMS deposition mode and characterized by GIFAD. This chapter concludes by discussing the future possibilities for achieving better control on the real-time deposition of thin layers using HiPIMS and GIFAD.

Chapter 2

High-pressure Grazing Incidence Fast Atom Diffraction (HP-GIFAD): experimental setup, operational principles, and results

Overview

Grazing Incidence Fast Atom Diffraction (GIFAD) is a comparatively new surface analysis technique where neutral He atoms are coherently scattered from a crystalline surface. The whole process can be separated into three different steps with first, the production of a neutral atom beam, then subsequently scattering from a crystalline surface, and finally, the detection of the scattered beam on a position-sensitive detector. The earlier development of GIFAD targeted the characterization of surfaces in Ultra High Vacuum (UHV), since the major concern was to preserve the transverse coherence of the beam. In addition, the detector technology that is used requires pressure lower than 10^{-5} mbar. Technological advances led us to design and develop a novel GIFAD setup that is able to operate up to 10^{-2} mbar. The novel HP-GIFAD system opens wide avenues for the study of surface reactivity and thin film growth in Magnetron Sputtering Deposition, where the electromagnetic fields inevitably perturb electron diffraction. This chapter includes the experimental setup of the high-pressure GIFAD system, principles of operation, and experimental results of the newly developed HP-GIFAD system, where the well-resolved diffraction pattern has been observed up to 10^{-2} mbar of pressure.

2.1 Introduction

Surface diffraction methods help to determine the atomic structure of the topmost layer of a crystal. However, most surface diffraction methods operate at Ultra High Vacuum (UHV) conditions to maintain the surface clean, i.e., adsorbate-free over the course of experiments. This limits the reaction condition that can be studied. It is essential to understand the solid surface and its interaction with the environment, which opens up a new field of research in catalysis, corrosion, nanotechnology, and thin film electronics [38, 39, 40]

Grazing geometry provides surface sensitivity, and a number of different measurements can be done to understand surface reactivity. Surface X-ray Diffraction (SXRD) is a powerful method where the hard X-rays (Energy: 6-30 keV) are used to study catalytic activity on the surface under high-pressure conditions. Weak interaction of X-rays with the surface needs intense radiation obtained from the synchrotron facility to detect the diffraction signal from the surface. Thus, SXRD is one of the techniques used for surface structure determination in high vacuum (HV) to ambient conditions.

Another surface-sensitive technique that is widely used is Reflection High Energy Electron Diffraction (RHEED). RHEED is widely used in the thin film community to do *in-situ* diagnostics in UHV deposition systems. However, RHEED has been adapted successfully with Pulsed Laser Deposition (PLD) systems, where the deposition pressure can reach up to 50 Pa (0.5 mbar)[32]. This new configuration of RHEED is called high-pressure RHEED, which is achieved by introducing double differential pumping stages on the gun side and decreasing the path length of e^- beam in the high-pressure region by placing the detector very close to the substrate. The mean free path of the electron is reduced from 100 m to 100 μm when the pressure is increased from 10^{-6} mbar to 1 mbar. The RHEED system kSA 400 is the most powerful RHEED analysis system available for MBE, PLD, and PVD deposition systems[41].

Scattering of mono-energetic He atoms from surfaces is a popular surface analysis technique known as Helium Atom Scattering (HAS) or Thermal Energy Atom Scattering (TEAS), which was demonstrated by Estermann and Stern[42] in the early 1900s, just after the discovery of electron diffraction. TEAS provides information on surface structure, phonon spectra, and impurities. This technique is very sensitive to the topmost layers of the surface but extremely slow for decades. The main reason was the lack of intense or bright He atom sources. In the beginning, the effusive (Knudsen) cells are used to prepare low-intensity and non-monochromatic He beams. Around 1970, the invention of a supersonic expansion nozzle gave a platform to TEAS, and the intensity and monochromaticity were improved simultaneously. This technique has been widely used to characterize the surface and study thin film growth [43]. As the detection is performed by measuring intensity point by point by a mass spectrometer, this technique is relatively slow and laborious[44].

Grazing Incidence Fast Atom Diffraction (GIFAD) is the high-energy counterpart of TEAS, has developed as an effective and complementary method for surface analysis and thin film growth monitoring[45, 43]. In 2003, the Orsay group[25], followed by the Berlin group[29], independently discovered the diffraction of fast He atoms from a crystalline surface under grazing scattering. This led to the development of a tool, named Grazing Incidence Fast Atom Diffraction or GIFAD. Compared to HAS, keV neutral atoms are easy to detect as the entire diffraction region is confined in a narrow cone and recorded instantly without performing any scan. Another advantage of GIFAD is that it provides 2D diffraction images, in which the intensity distribution of scattered atoms provides additional information of the surface scattering process (density of defects, local ordering, elastic vs inelastic ratio, etc.). The extreme surface sensitivity of this technique allows us to probe the projectile surface interaction potential, called Potential Energy Surface (PES)[46, 47, 48]. In the reciprocal space, the intensity distribution is given by the Fourier-like transform of this equipotential surface $Z(y)$ (section 2.3.1). The grazing geometry of the projectile strongly reduces the decoherence effect due to the thermal vibration of surface atoms[49]. The He-surface interaction potential has two parts: the attractive and repulsive parts. When the normal energy (energy normal to surface) to the surface is larger than the potential well, which is 5-15 meV(well depth) [50, 51] for He atoms then the attractive part of the potential can be neglected. Then, the interaction potential only contains the repulsive part, which is equivalent to the electron density profile of the surface.

The de Broglie wavelength of an atom can be expressed as $\lambda_{dB} = \frac{h}{mv} = \frac{h}{\sqrt{2mE}}$, m , v and E are the mass, velocity and initial energy of the atoms. By considering 1 keV energy, the de Broglie wavelength is 0.45 pm. To observe the diffraction, the transverse coherence length, i.e., the width of the associated wave packet must be larger than twice the crystal period. For example, if d is the periodicity of the crystal and L_c is the transverse coherence length, then $L_c > 2d$, as shown in Fig. 2.1. The width of the wavepacket is dependent upon the de Broglie wavelength (λ) and the divergence angle (θ), $L_c \approx \frac{\lambda}{\theta}$ [52] So, the energy and collimation system plays an important role in observing diffraction. A good collimation system is an important parameter in order to maintain sufficient degree of coherence of the beam.

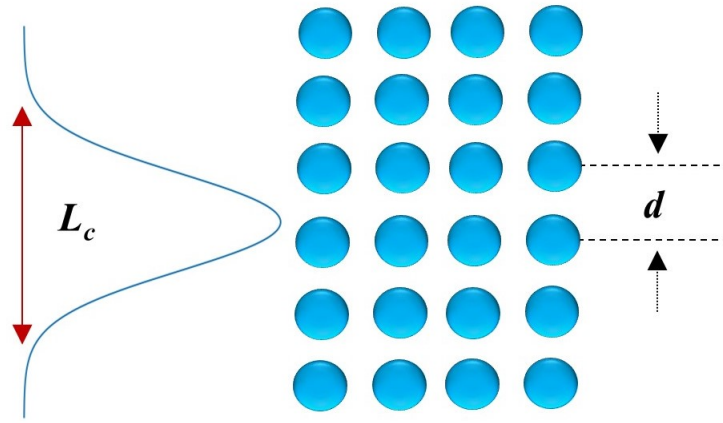


Fig. 2.1: Schematic of the diffraction condition of a wave packet of transverse length L_c interacting with a surface having period d .

Up to now, all the experiments with GIFAD have been confined to the UHV regime. However, most of the thin film growth techniques operate above 10^{-6} mbar of pressure like Magnetron Sputtering (MS) operates between 10^{-3} and 10^{-2} mbar[53], reactive pulsed laser deposition operates up to 0.1 mbar[54], and CVD technique covering large span of pressure from UHV to atmosphere[55, 56].

Among many other PVD-based deposition systems, Magnetron Sputtering (MS) is one of the popular thin film deposition processes that can be used in laboratories and also in industry for mass production. However, the adaptation of RHEED with Magnetron Sputtering systems is quite complex due to the electromagnetic force exerted on the e^- by the electromagnetic fields present in the sputtering systems. RHEED has been tentatively adapted with Magnetron Sputtering (MS) deposition systems. In this situation, the magnetic field is confined near the target so that the field has a negligible effect on the trajectory of the electrons[57]. Obviously, this solution has not been generalized. As an alternative, the high-pressure version of the GIFAD setup could be useful in following the real-time growth of thin films in Magnetron Sputtering (MS) deposition systems.

The standard GIFAD setup comprises four different stages, as described below.

1. An ion source to produce the primary He ion beam.
2. A neutralization cell or charge exchange cell followed by a series of apertures to collimate the beam.
3. A UHV chamber has equipped with a five-axis manipulator (x, y, z, θ, ϕ) system to manipulate the sample.
4. A detector system comprising two Micro Channel Plates (MCPs), a phosphor screen, and a CCD camera.

In section 2.2.3, we will describe in detail the significant evolution of the high-pressure GIFAD with respect to standard configuration.

2.2 Experimental setup

2.2.1 Ion source

Most commercial ion sources that provide low energy (keV range), small diameter, and bright ion beams are of the electron impact type, and beam focusing is obtained by two consecutive lenses, objective and focus. If the beam energy is high (> 500 eV), the objective lens decelerates the ions, and for low energy beam, the objective focus operates in accelerating mode to maintain the high velocity of the ions until the end of the column. This helps to reduce the space charge and minimizes the effect of repulsion.

These sources are usually dedicated to sample preparation and depth profiling with Auger and XPS experiments. Focusing is optimized at rather short distances, of the order of 20-40 mm, this is not the best operation mode for GIFAD where a small and parallel beam is required.

In HP-GIFAD, we used an ion source from Nonsequitur Technologies, model 1406, which is a modified version of the 1401 model. With only one focusing stage, the 1406 has been specifically designed for providing beams of very small divergence for GIFAD. The He gas is injected into the ion gun and the hot filament, which delivers an emission current up to 10 mA, produces electrons that ionize the atoms in a zone set at a voltage (source voltage) that determines the final ion energy. The ions are further extracted by a voltage between 70 and 95% of the source voltage, accelerated/decelerated to the desired energy, usually in the range 200-5000 eV, and finally focused on a differential aperture by the condenser lens. The ion source comprises two filaments and produces ion beams of noble gases (He, Ar, Ne, etc.). To preserve the filament lifetime and reduce beam contamination (there is no mass filtering of the extracted beam), the pressure inside the ion gun is below 10^{-8} mbar.

2.2.2 Neutralization or charge exchange cell

The neutralization of the ions happens inside the neutralization cell (Fig.2.2). In the cell, He gas is injected at a pressure of 10^{-4} to 10^{-3} mbar to neutralize the ions. Due to the resonant charge transfer[58], 10-15 % of the ions are neutralized. It has been considered that the collisions that happen inside the cell are in a single collision regime as the multiple collisions diverge the beam rapidly although a higher neutral fraction is possible to obtain in this scenario.

The pressure measured by the cold cathode gauge mounted on the neutralization cell is 2×10^{-6} mbar. But inside the cell, the pressure is much higher than 10^{-6} mbar, the estimation can be made using the following calculation.

The calculation is quite simple and depends on the probability of collisions. The probability of collisions (P) along a path of length l depends on the number density of gas atoms (n) and the scattering cross section (σ), stated as $P \approx n \times \sigma \times l$. So, if the length of the cell is small, the pressure must be high enough

to achieve the neutralization.

The length of the neutralization cell in HP-GIFAD is almost twice than the older GIFAD (LP-GIFAD). The advantage of having a long cell is to operate at lower pressure.

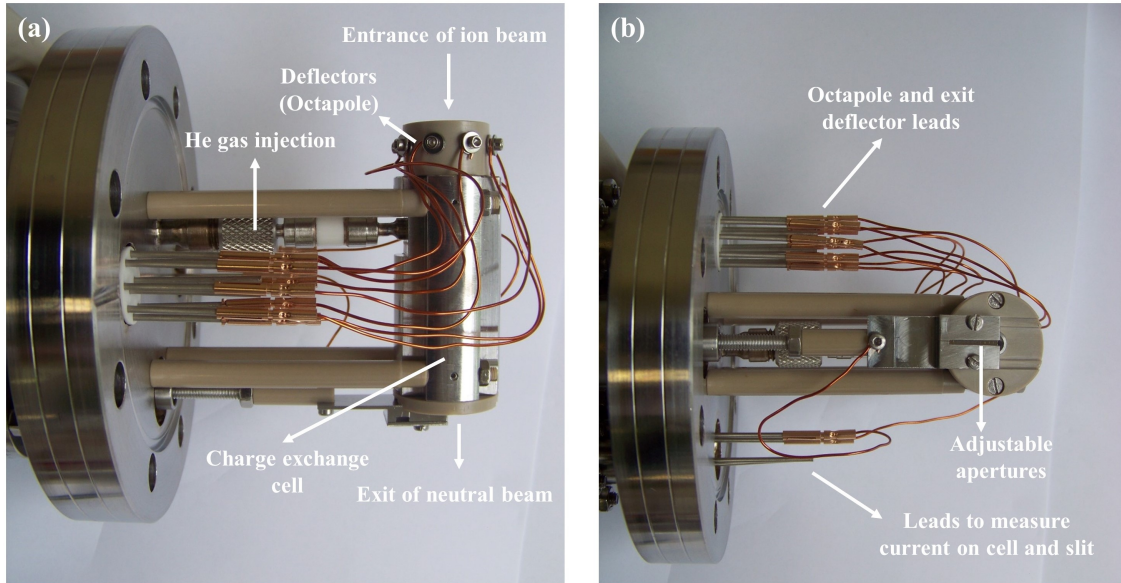


Fig. 2.2: (a)-(b) Photograph of the charge exchange cell with its different stages.

The electron capture cross-section of He^+ on He is $\sim 10^{-15} \text{ cm}^2$ [59], now the length of the cell is 4.6 cm. Suppose 10% of the ions are getting neutral after the charge exchange process, so $P = 0.1$. The pressure inside cell will be $9 \times 10^{-4} \text{ mbar}$ ($\sim 10^{-3} \text{ mbar}$).

In addition, low pressure inside the neutralization cell helps to reduce the diffusion of gas outside the cell, along the beam trajectory. The neutralization cell consists of two apertures, one entrance and one exit aperture having diameters $800 \mu\text{m}$ and $400 \mu\text{m}$. The pressure outside the cell is $\sim 2 \times 10^{-6} \text{ mbar}$. The apertures also limit the divergence of the beam.

At the exit of the neutralization cell, the remaining ions are deflected away by applying a few tens of volts between parallel plates. The stringent collimation of the neutral beam is obtained by a set of two movable plates supporting multiple apertures (with rectangular and circular shapes); the first plate is located at the exit of the neutralization cell, as shown in Fig.2.2-b. In HP-GIFAD setup, the second collimation stage having a fixed aperture, $150 \mu\text{m}$ of diameter is positioned at $\sim 30 \text{ cm}$ downstream, located at the entrance of the UHV chamber (exit of tube T_{in} , Fig.2.3). In order to adjust the beam and optimize the transmission through the cell, the beam intensity can be measured on the cell itself as well as on the aperture plates. Measured currents actually correspond to that of the ejected secondary electrons produced by the He atoms hitting the metallic cell and plates.

2.2.3 The UHV chamber and the detector system

2.2.3.1 The UHV chamber

The Ultra High Vacuum (UHV) chamber consists of a five-axis manipulator, differential pumping stages, a one-inch magnetron cathode, a sputter ion gun, and a quadrupole mass spectrometer (QMS) as shown in Fig.2.3.

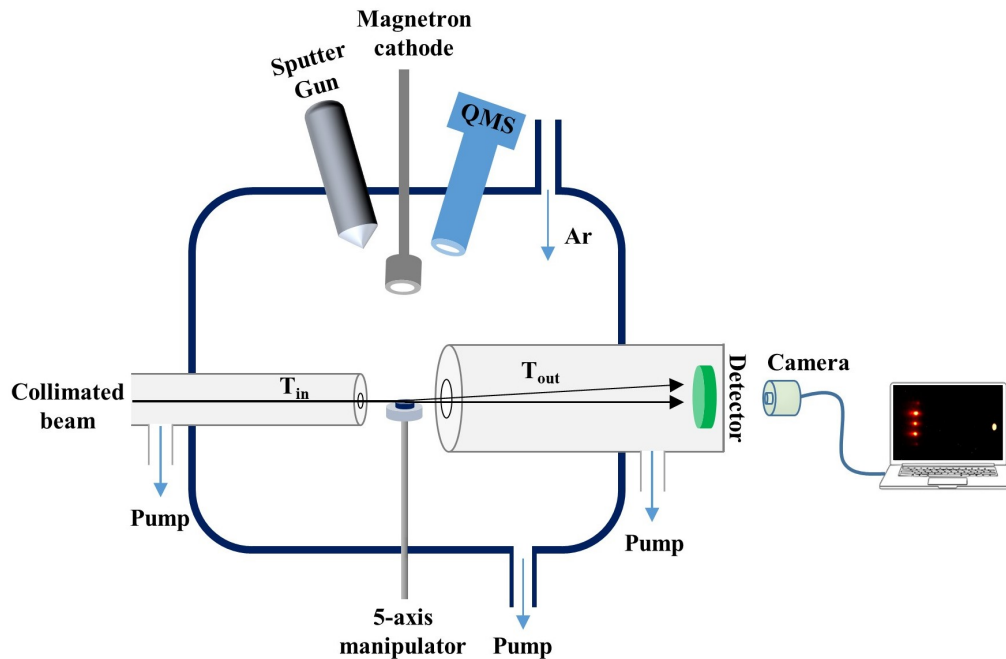


Fig. 2.3: A schematic of the main chamber and the detector with the different components.

The significant evolution of the high-pressure GIFAD setup, with respect to the earlier low-pressure version, is the double differential pumping stages, which permit the operation of the detector below 10^{-5} mbar of pressure while the pressure inside the main chamber is much higher ($\sim 10^{-2}$ mbar).

After passing through the first collimation stage, the neutral atom beam is introduced into the main chamber using an entrance tube (T_{in}) having an aperture of $150 \mu\text{m}$ diameter, thus acting as both second collimation stage, and differential pumping aperture.

A differential pumping system is a scheme of pumping stages used to maintain different vacuum levels along the beam path[60]. The ideal way is to add different pumping stages separated by small apertures, but it makes the whole system quite extensive. An example of a multistage differential pumping system in an X-ray beam line is shown below.

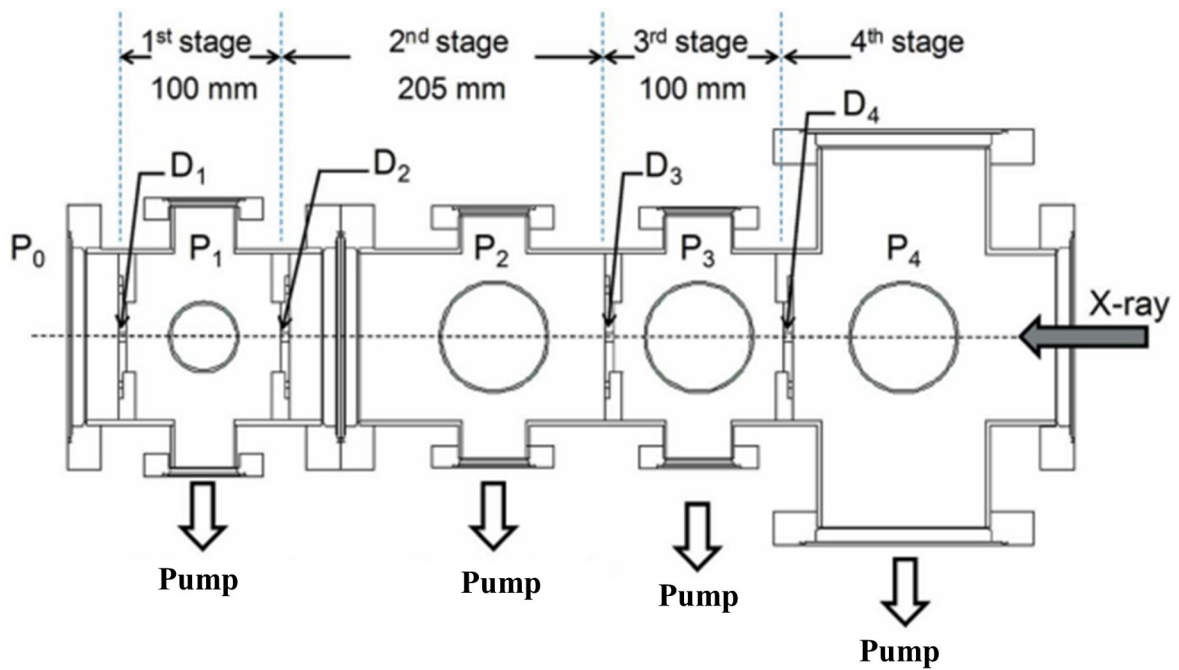


Fig. 2.4: Schematic drawing of the prototype differential pumping system. Taken from [61].

This results in an extended high-pressure zone, which further reduces the beam intensity on the detector. To avoid this, the exit tube (T_{out}) consists of several tubes of different lengths having apertures of 4-10 mm and is introduced between the main chamber and the detector (Fig 2.5-a).

The apertures of the differential pumping tubes are further reduced (Fig.2.5-b) to reduce the conductance between the main chamber and the detector, which helps to maintain the pressure on the detector side below 10^{-5} mbar, while the pressure in the UHV chamber exceeds 10^{-3} mbar. Note that, as shown in Fig.2.5-c, activation of the last pumping tube does not influence the pressure ratio (gain factor). After careful observation, we noticed that the welding of the tube end rings on the CF100 TEE was not leak-tight, which is a manufacturing defect. It is worth mentioning here during the experiments (Fig.2.5-c), no specific care was taken for the pressure measurement (calibration).

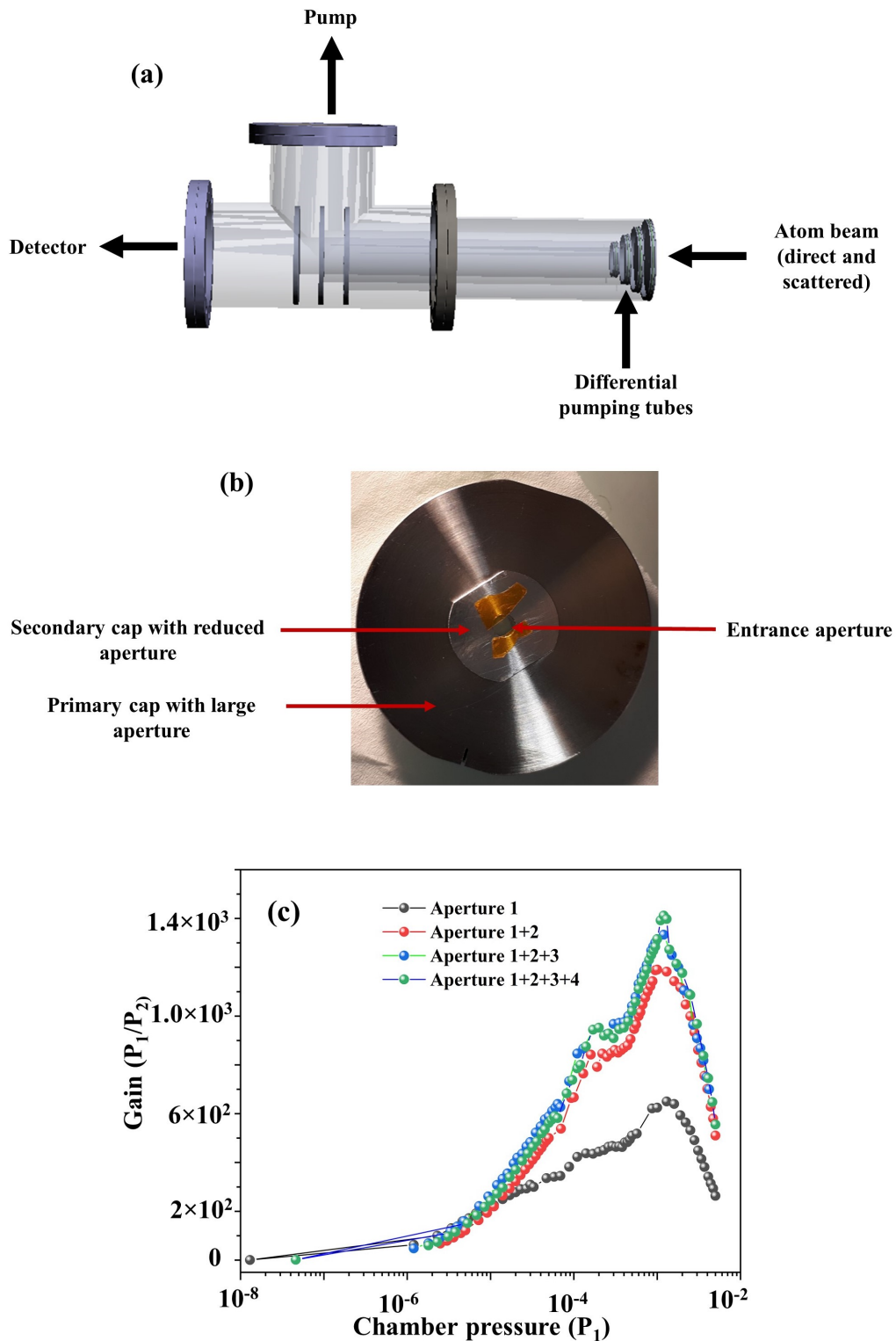


Fig. 2.5: a) Configuration of the multi-tube differential pumping system: each tube is equipped with a cap of having a small aperture. (b) Entrance aperture to the first tube, Kapton tape is used to reduce the aperture size, (c) evolution of the pressure ratio between the UHV chamber and the detector chamber as a function of the number of stages, a stage is considered active when the apertured cap is mounted.

The UHV chamber is equipped with a quadrupole mass spectrometer (QMS) also called a Residual Gas Analyzer (RGA). Here, the Extorr RGA[62] has built with a Pirani and hot cathode gauges and has a measuring range of 300 amu. The hot filament gauge works based on electron impact ionization

of residual gases, which produces an ion current. The Pirani gauges operate at low pressure and uses thermal conductivity of the residual gases. A schematic of the compact Extorr RGA is shown in Fig.2.6. The black box is the command and control unit (CCU).

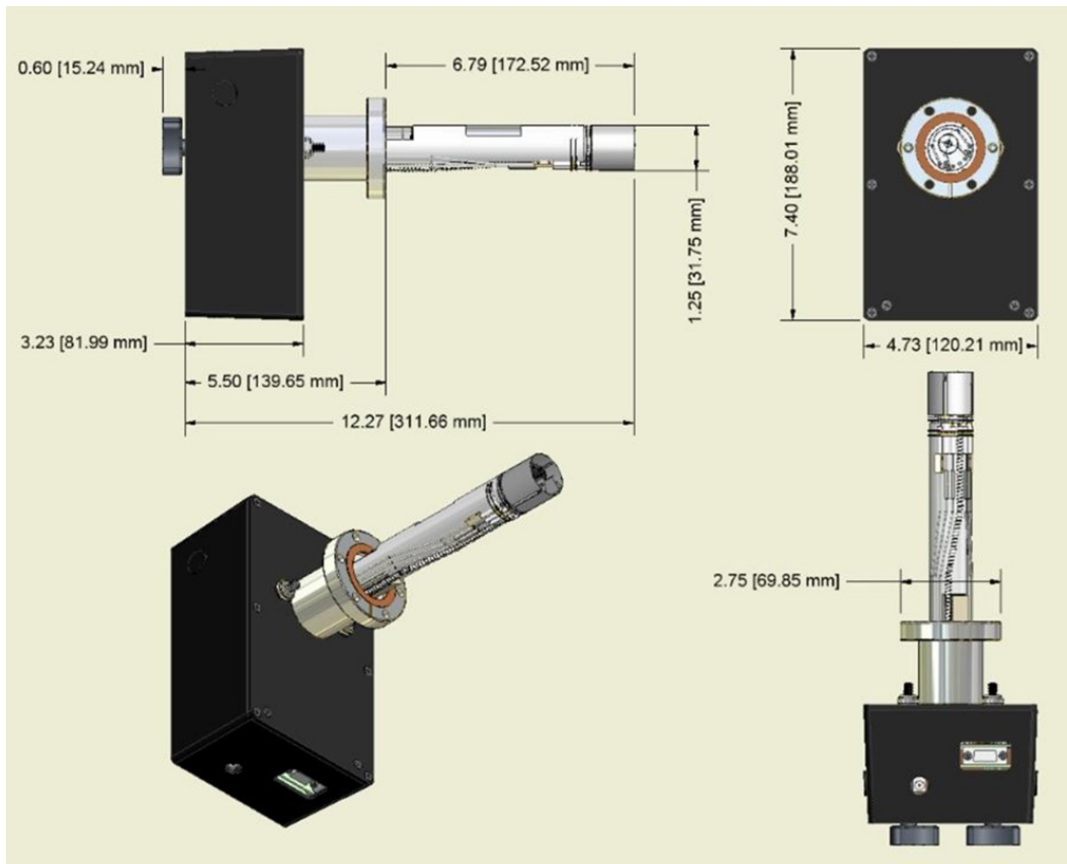


Fig. 2.6: The image of the Extorr RGA with CCU box compatible with DN 40 CF.

To avoid damage of the ionization filament, QMS must be operated below 1 mTorr. A mass spectra measured at 3×10^{-8} mbar of pressure inside the main chamber is shown below in Fig.2.7. Generally, without baking, the maximum partial pressure recorded on QMS is due to the H_2O . After strong baking (up to $150^\circ C$), H_2 dominates over H_2O . Because of the light nature of H_2 , this gas is difficult to pump down using a turbo molecular pump due to their particularly low compression ratio for this gas[63].

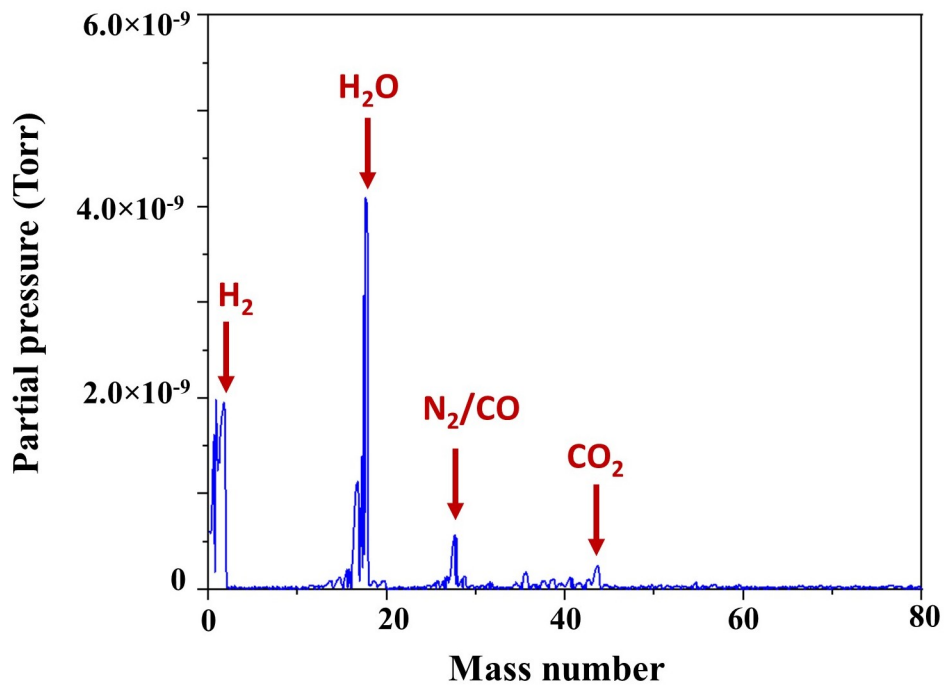


Fig. 2.7: RGA spectra at 3×10^{-8} mbar of pressure. Taken from HP-GIFAD UHV chamber.

The UHV chamber is equipped with an Ion Sputtering GUN, IG 35-DP, a model is generally used for cleaning the sample surfaces or depth profiling with Auger Electron Spectroscopy (AES).

The basic geometry of the configuration is a combination of an ion source and an electrostatic lens configuration to accelerate and focus the beam on the sample. The configuration is shown in Fig.2.8.

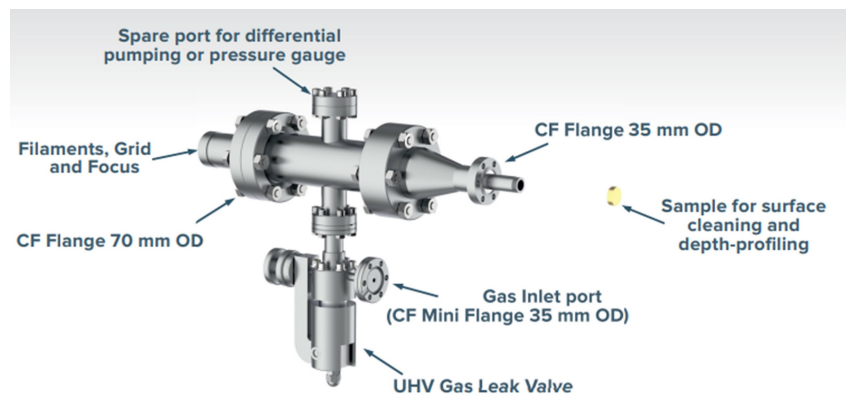


Fig. 2.8: Sputter ion gun configuration with different components. Taken from [64]

The 5-axis manipulator comprises three translational stages, X , Y , and Z , with two angular degrees of freedom θ and ϕ respectively. The θ is the angle of incidence of the He^0 beam with the surface plane, typically in the range ~ 0.3 - 1.5° , and ϕ is the azimuthal angle. The manipulator is mounted horizontally with the sample surface in the vertical plane.

The sample holder has a heating and cooling system. The most widely used method of increasing the sample temperature is radiative heating. Behind the flag-style sample holder plate, a heating filament is

placed which enables a radiative heating behind the sample up to 800°C. The temperature is measured by a thermocouple of type K attached to the sample holder. The filament is sustainable up to 10 A of current.

Another annealing mode for the sample is by e^- bombardment on the sample plate. In this process, a positive bias voltage is applied to the sample, and the filament is heated enough to emit electrons. The electrons acquire the energy from the bias voltage and dissipate it as heat on the sample plate. The e^- bombardment is a rapid and efficient way to increase the temperature of the sample.

However, it has never been used in any experiments in the course of this thesis. The filament, sample holder, and LN₂ feed-through are shown in Fig. 2.9.

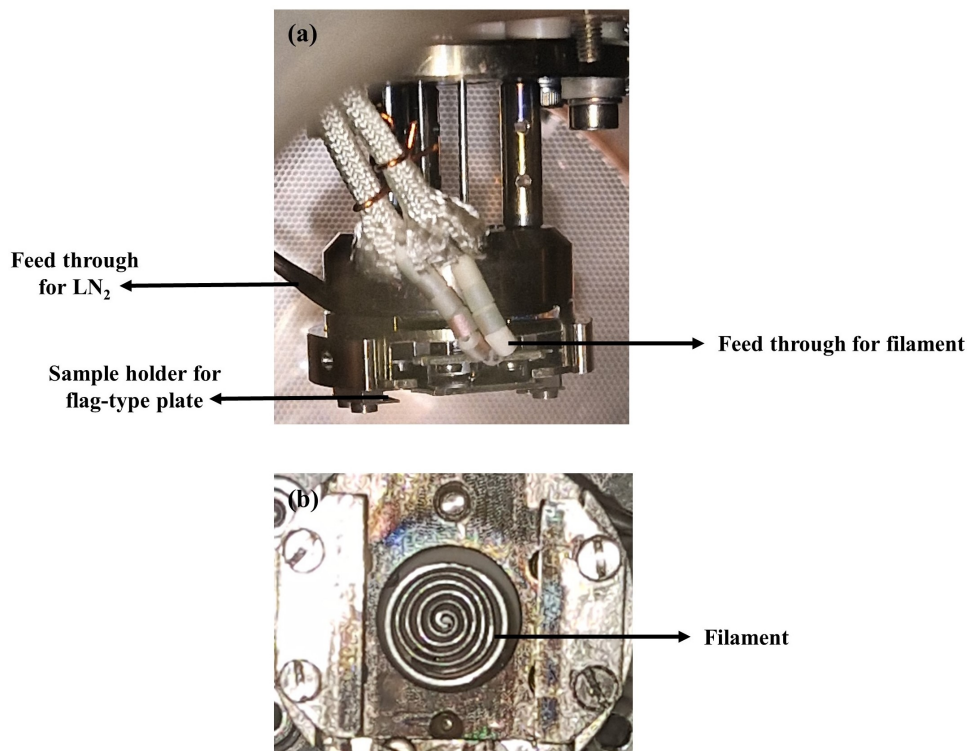


Fig. 2.9: (a) Top view and (b) front view of the UHV side of manipulator.

The UHV chamber is also equipped with a 1 inch magnetron cathode. A balanced MAK sputter source[65] is installed with a Cu target. To protect the sensitive parts (ceramics, wires) of the manipulator, a fixed vertical shield plate is placed between the differential pumping tubes. It has an opening of 3 cm in diameter to let the sputtered species reach the substrate. Another movable shutter, with an opening of 2 cm in diameter, is placed just between the fixed shield plate and the substrate as shown in Fig. 2.10.

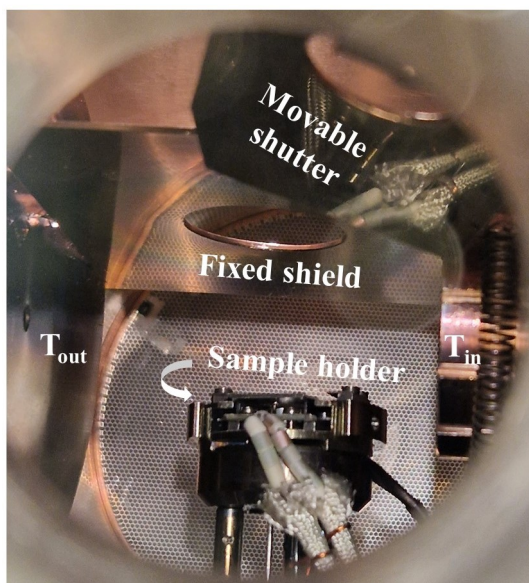


Fig. 2.10: Configuration of the shield and shutter inside the UHV main chamber.

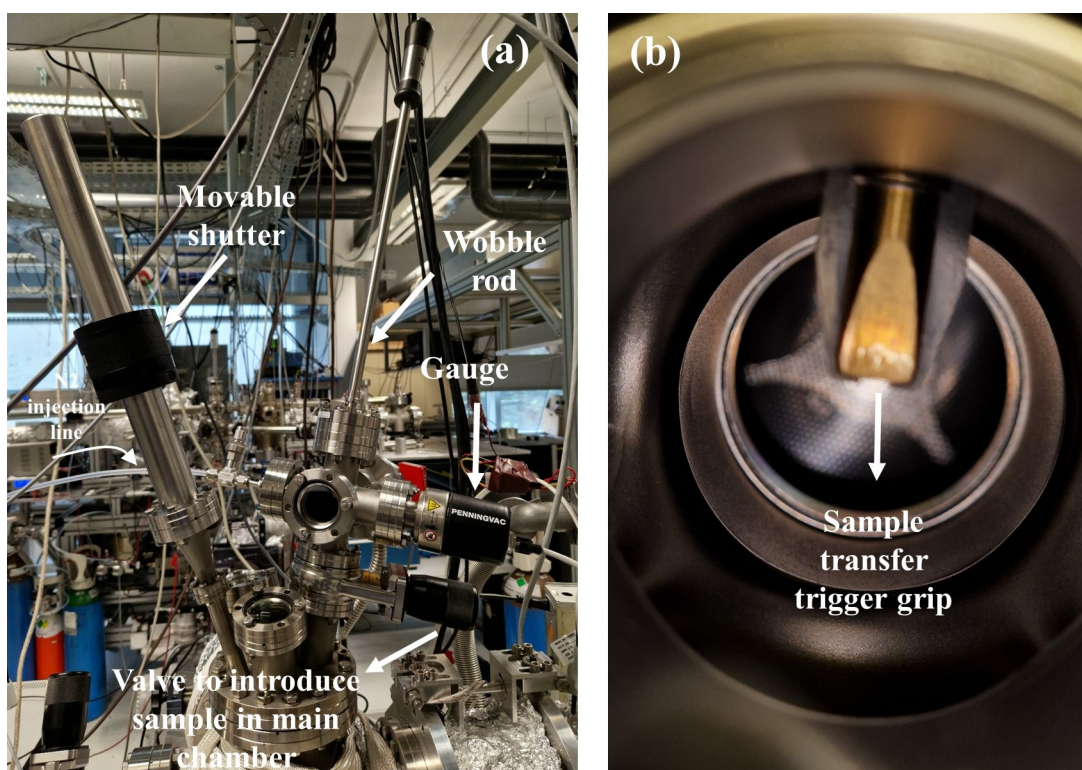


Fig. 2.11: (a) Introduction chamber to transfer the sample, (b) wobble stick trigger grip to hold the sample.

A small introduction chamber has been installed on the top of the main chamber to transfer the sample to the manipulator in UHV conditions (Fig. 2.11). Generally, the sample is introduced into the introduction chamber with continuous venting with dry N_2 . This helps to recover the pressure rapidly after starting the pumps. After getting suitable Ultra High Vacuum conditions, the valve is opened, and the sample is transferred to the UHV chamber.

2.2.3.2 The detector system

The detector system is composed in the vacuum side of two Microchannel Plates (MCP), and a fiberoptic phosphor screen with P20 phosphor mounted to a 8-inch vacuum flange. The fiberoptic is frit-sealed into the flange to form a vacuum seal.

The microchannel plate (MCP) is an array of tiny electron multipliers oriented parallel to each other, as shown in Fig.2.12. The diameter of the channel is $10\mu\text{m}$ order, and the length-to-diameter ratio is 60. The axes of the channels are tilted by $\sim 8^\circ$ with respect to the MCP surface normal.

The MCP detectors are sensitive to single particles (electrons, ions, and neutrons) and photons (X-ray and ultraviolet radiation). When the high energy particle hits the wall of the channel, the secondary electrons are emitted from the surface and produce an avalanche by a cascade process due to a voltage bias (0.5-1 keV) between the faces of MCP. So, each channel can be considered as an electron multiplier, with a gain of 10^2 - 10^4 depending on the bias. The total resistance between the electrodes is $10^9 \Omega$ [66].

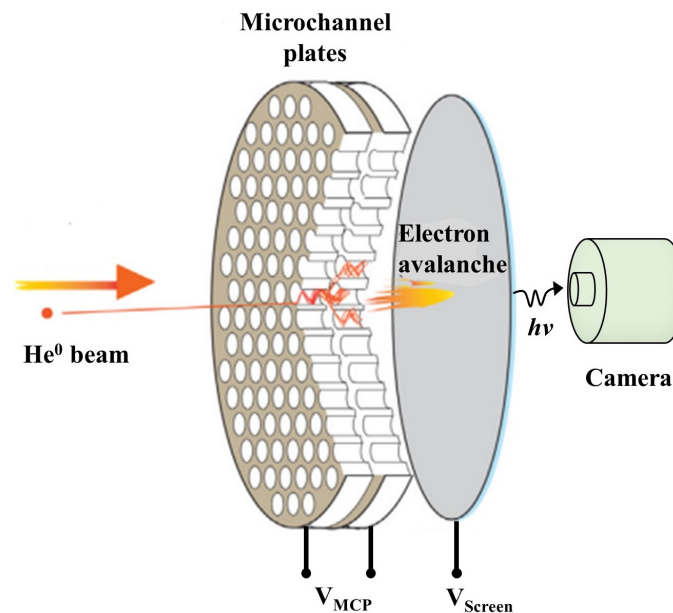


Fig. 2.12: Configuration of the detector comprises of Microchannel Plates and phosphor screen and CCD camera.

When the avalanche electrons from MCPs hit the phosphor screen, they produce photons with a nominal wavelength of 550 nm, at a rate of ~ 0.05 photons/electrons/eV. The operation mode of our detector is $V_{MCP} = 1.7$ kV across the two MCPs, with the front face of the first MCP at the ground and $V_{Screen} = 4$ kV on the phosphor screen. Here, a standard detector by Photonis [67] is used, shown in Fig. 2.13. These detectors are compatible with UHV and bakable up to 300°C .

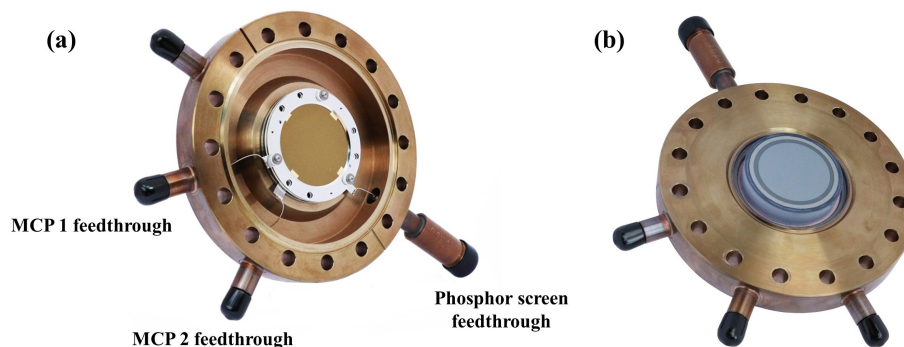


Fig. 2.13: The ‘Photonis’ detector having (a) UHV side and (b) air-side with feed-throughs, the air-side of the fiber optic screen is clearly visible.

2.3 Principles of GIFAD

2.3.1 Scattering geometry

Grazing incidence Fast Atom Diffraction (GIFAD) is a comparatively new surface analysis technique that has been used to characterize different types of material[37, 68] (**Chapter 1**). The energy of the fast He atoms is in the range of 200-5000 eV. Everyone has been taught that an essential aspect of the diffraction phenomenon from surfaces is wavelength matching, meaning that the de Broglie wavelength associated with the particle has to be comparable to the periodicity of the crystal, which is typically in the Angstrom scale. Many examples have shown that this statement does not hold. For instance, the diffraction of MeV energy electrons through thin crystalline samples has been observed[69]. An extreme case comes from the observation made by Klaus Hornberger et al.[70]. Recently, Klaus Hornberger et al.[70] has shown an interference pattern with C_{70} fullerenes using a grating with 991 nm period; here, the ratio between period to wavelength is greater than 2000. In the case of GIFAD, the wavelength of 1 keV He atom is 0.45 pm, which is typically a thousand times smaller than the period of the crystals.

The schematic of the scattering of neutral He atoms in GIFAD from a crystalline surface is shown in Fig. 2.14, which corresponds to the situation where the incident beam is perfectly aligned to a crystalline direction.

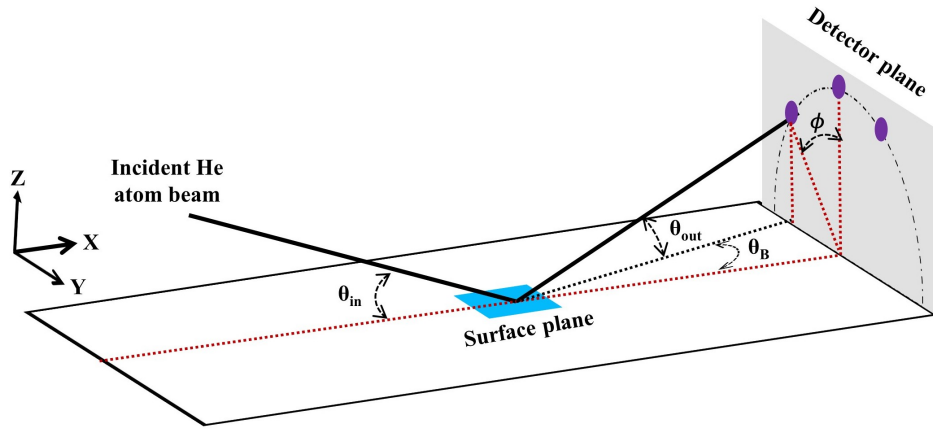


Fig. 2.14: Schematic of scattering geometry in GIFAD.

Here, θ_{in} and θ_{out} are the incidence and polar exit angles. The diffraction spot (in Fig. 2.14, 1st order) is located at an angle θ_B . The angle θ_B is known as Bragg angle, is defined as $\tan\theta_B = \frac{G}{k_{\parallel}}$; $k_{\parallel} = k\cos(\theta_{in}) \sim k$ and $G = \frac{2\pi}{d}$, where d is the periodicity of the crystal. G and k are the reciprocal lattice vector and the scattering vector.

The scattering mechanism is considered along the low index direction of the surface, i.e. there is no misalignment of the He beam with respect to the crystalline direction. Due to the grazing geometry, the velocity parallel to the surface (fast motion) is much higher than the perpendicular component (slow motion); these two components are decoupled from each other.

Suppose the velocity of the neutral atom beam is v and has an energy E . Under grazing conditions, the velocity components are $v_{\parallel} = v \cos\theta_{in}$ and $v_{\perp} = v \sin\theta_{in}$, where θ_{in} is the incidence angle according to Fig.2.14. As θ_{in} is small ($< 1^\circ$), the velocity parallel to the surface is very high compared to the perpendicular direction and these are known as ‘Fast’ and ‘Slow’ motion respectively. The corresponding energy components are $E_{\parallel} = E_0 \cos^2\theta_{in}$ and $E_{\perp} = E_0 \sin^2\theta_{in}$, where $E = E_{\perp} + E_{\parallel}$.

The scattering process is governed by the interaction potential between the He atom and the surface. Consider a 3D corrugated surface, but due to the fast motion of the atoms, He atoms feel an average potential along the propagation direction, thus transforming the 3D corrugated surface to its 2D average, as shown below in Fig.2.15.

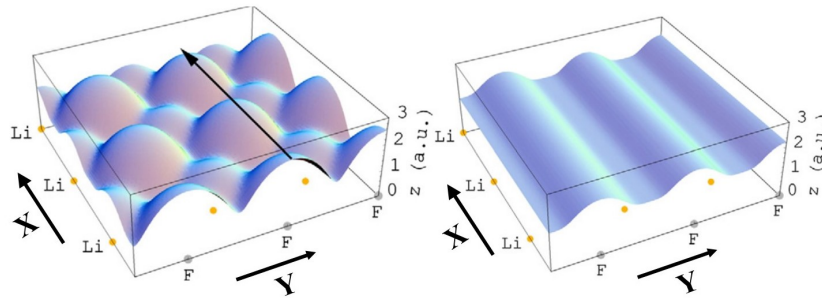


Fig. 2.15: Left side : 3D corrugated surface $V(x, y, z) = 3 \text{ eV}$ of He atom at LiF(001) surface , arrow indicates the direction for averaging of $V(x, y, z)$ along $\langle 110 \rangle$. Right side: 2D corrugated surface of $V(y, z) = 3 \text{ eV}$.

In the above figure (Fig.2.15), it is considered that the diffraction takes place on the corrugated surface, and due to the fast motion of the beam along the x direction, the 3D corrugated surface $V(x, y, z)$ is reduced to its 2D average as shown in Fig. 2.15. So, $V(y, z) = \int_0^{a_x} V(x, y, z) dx = E_{\perp}$, where a_x is the periodic length along the low index direction of the crystal[71].

The slow motion perpendicular to the surface has an impact, considered as ‘soft collisions’ between the incoming He atoms and the surface atoms. At the grazing incidence, the energy normal to the motion (E_{\perp}) is in the range of 1 meV to 1 eV, which prevents the penetration of the He atoms below the first atomic layer. This makes the classical turning point (where the velocity direction is reversed) is $\sim 2\text{-}3 \text{ \AA}$ above the topmost layer of the surface, as shown in Fig.2.16.

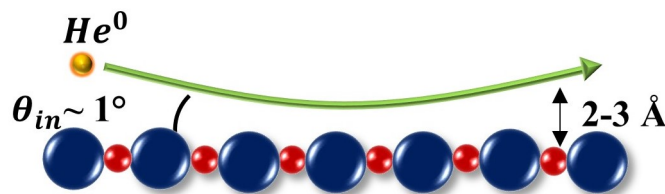


Fig. 2.16: Grazing scattering of He atoms from the topmost layer of the surface. Due to the very low energy in the direction normal to the surface, the atoms are scattered above the first atomic plane.

It has been found that for 60 meV of energy of He atoms in Thermal Energy Atom Scattering (TEAS) from close-packed Cu(111) surface, the turning point is 3 \AA above the surface layer of atomic cores[72, 73], which is larger than the mean amplitudes of the thermal vibration of atoms.

Two contributions characterize the He-surface interaction potential:

1. A long-range, attractive, dispersion force or van der Waals force originating from the induced dipoles.
2. A short-range, repulsive force arising from Pauli's exclusion principle. [74].

2.3.2 Quantitative analysis of the diffraction pattern

It can be seen that the normal energy of the beam can be tuned from a few meV to several eV by changing either energy or the incidence angle.

Here, it is considered that the initial and final momentum of the atoms are $\vec{k}_i(k_{ix}, k_{iy}, k_{iz})$ and $\vec{k}_f(k_{fx}, k_{fy}, k_{fz})$. However, when the beam is aligned along the crystallographic direction, then 'y' component of the incidence wave vector is zero, i.e., $k_{iy} = 0$.

According to Laue condition $\Delta\vec{k} = \vec{k}_f - \vec{k}_i = \vec{G}$, where $\Delta\vec{k}$ the momentum exchange between atoms, \vec{G} is the reciprocal lattice vector of the crystals, which is formed using primitive translation vectors \vec{G}_1 , \vec{G}_2 , and \vec{G}_3 . So, $\vec{G} = h\vec{G}_1 + k\vec{G}_2 + l\vec{G}_3$, where h, k, l are the integer numbers and each choice of $(h k l)$ is called Miller indices.

Now, on the surface, a general translation vector of the reciprocal lattice can be written as $\vec{G}_{hk} = h\vec{G}_1 + k\vec{G}_2$, where h and k are the integers (Miller indices). \vec{G}_1 and \vec{G}_2 are the primitive translation vectors in reciprocal space.

Now, if we consider $\vec{G} = \vec{G}_x + \vec{G}_y$ and $\vec{G}_x = h\vec{G}_1$, and $\vec{G}_y = k\vec{G}_2$, and the diffraction pattern associated with the rows of atoms parallel to the direction of the incident beam. Due to the high velocity along the beam direction (From Fig.2.15, X is the direction of motion), the momentum parallel to the surface is high, which means the energy required to exchange momentum along X direction will be costlier than the Y , which substantially giving the condition $\vec{G}_x = 0$, and the diffraction arises where $\vec{k}_f - \vec{k}_i = \vec{G}_y$ condition is satisfied. Here, $\vec{G}_y = \frac{2n\pi}{a_y} \vec{a}_y$, \vec{a}_y having a periodicity of the lattice according to the low index channeling direction and n is the diffraction order. To resolve the Bragg peak on the detector, the angular resolution of the beam must be less than the Bragg angle, where the Bragg angle is defined as $\theta_B \sim \frac{G_y}{k_{\parallel}}$, where k_{\parallel} is the parallel component of the incidence wave-vector. The Bragg angle is typically ~ 1 -2 mrad in most cases.

As an example for LiF(001) surface along $\langle 100 \rangle$ direction, the periodicity is $a_y = \frac{4.02}{2} = 2.01 \text{ \AA}$ and along $\langle 110 \rangle$ the periodicity is $\frac{4.02}{\sqrt{2}} = 2.84 \text{ \AA}$ as shown in Fig. 2.17-a.

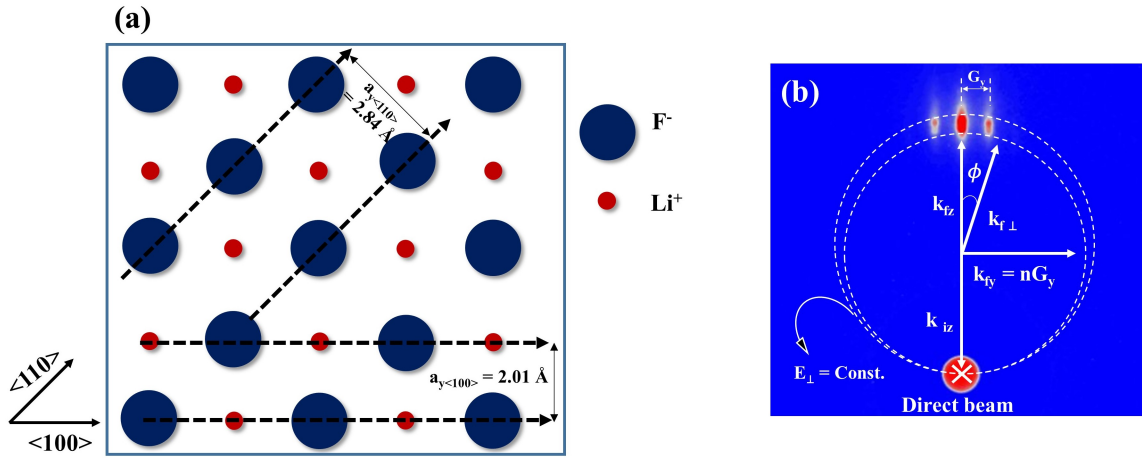


Fig. 2.17: (a) *LiF(001) surface and two directions are shown here, (b) Diffraction of He atoms from LiF(001) surface along $\langle 100 \rangle$ direction.*

The diffraction pattern from the LiF (001) surface is shown in Fig.2.17-b. The image corresponds to the ‘YZ’ plane, and the direct beam does not interact with the surface. Generally, we define the lateral (horizontal profile) and polar distribution (vertical profile) of the diffraction intensities. The lateral and polar profiles are discussed in more detail in **Chapter 3**.

In GIFAD, the parallel atomic channels at the surface behave as a reflective grating for the quantum scattering process. The distance between two Bragg peaks is inversely proportional to the grating width; here, it is the width of the channel or the periodicity of the crystal along the low index direction. So, if the detector is calibrated properly, the surface lattice parameter can be obtained by measuring the peak spacing.

Diffraction intensities are analyzed by considering the Hard Corrugated Wall (HCW) model approximation to obtain the shape of the 2D potential energy surface (corrugation function).

According to the HCW model, the surface is assumed to be an infinite hard wall. So, the potential is defined as[75].

$$V(R, z) = \infty, \text{ for } z \leq Z(R) \quad (2.1)$$

$$V(R, z) = 0, \text{ elsewhere} \quad (2.2)$$

In equation (2.1), (R, z) is the position vector, z is the distance perpendicular to the surface. So, GIFAD is able to provide information about the corrugation of the surface, which will be discussed later.

This is the semi-classical approach and it has been seen that when the surface is relatively flat and smooth, the HCW model is able to give insight into the atom surface interaction as well as on the surface structure[28].

In the HCW model, the interaction takes place on the equipotential surface that perfectly matches with the normal energy of the incident He atom. GIFAD is able to provide information of this 2D Potential

Energy Surface (PES). The intensity distribution of the Bragg peaks is the Fourier transformation of this PES. So, the relative peak intensity of the Bragg peak gives access to the potential profile (Surface corrugation). By considering noble gas atoms as a probe particle, the attractive force is very weak and can be neglected at normal energies above 50 meV. The interaction potential is proportional to the electron density of the surface [76]. As a consequence, the information derived from quantitative analysis of the GIFAD data is similar to that provided by Atomic Force Microscopes (AFM) or Scanning Tunneling Microscopes (STM).

When He atoms scatter from the hard wall, two types of interference take place, inter and intra-channel interference. In Fig. 2.18. shows the trajectories of the He atoms depending on the interaction with the surface corrugation.

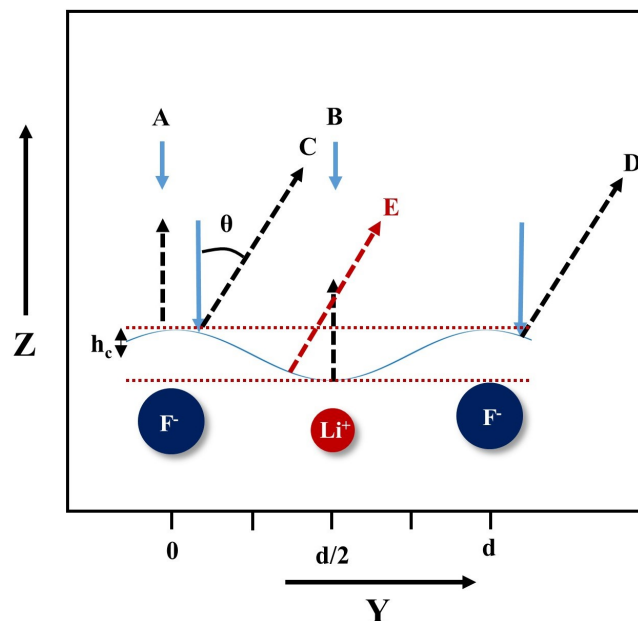


Fig. 2.18: Classical trajectories of deflected atoms after the interaction with the corrugation of the surface. The flat portion of the corrugation (bottom and top points, A and B trajectories), produces zeroth order and the deflection from different slopes gives n th order of the Bragg peaks.

Consider the $\langle 110 \rangle$ direction of the LiF(001) surface (Fig.2.18), where the channel width is defined by the string of F^- atoms. Here, h_c is the corrugation amplitude and d is the period of the crystal. Interference between trajectories C and D gives the Bragg condition, this is called inter-channel interference. On the other hand, intra-channel interference (trajectories C and E) produces a supernumerary rainbow pattern, which is the envelope of the Bragg peaks. Using the analogy of grating diffraction, we can say that the scattering from the unit cell determines the intensity of Bragg peaks. The steepness of the corrugation allows us to see the angular spread of the diffraction. This can be simplified as the number of Bragg peaks directly reflects the steepness of the corrugation function. At a large incidence angle and higher kinetic energy (higher normal energy), only the classical scattering is visible, known as ‘Rainbow Scattering,’ which is a classical analog to the atmospheric phenomenon. The ‘Rainbow’ is a general

concept in the classical scattering process where the deflection function (deflection angle vs. impact parameter) has an extremum. As the normal energy increases, the classical contribution to the scattering process becomes more visible; eventually, intensity maxima appear at the extreme lateral angles, which can be derived from the ‘Rainbow scattering.’ A theoretical study based on Surface-Initial Value representation (SIVR)[77] approximation, considered as a semi-quantum approach to produce the classical trajectories, has shown the effect of the involvement of the number of channels (N) on the Bragg peaks. For N=1, the Bragg peaks disappear, causing only supernumerary maxima due to the pure intra-channel interference[78]

By considering the simplest sinusoidal corrugation, the intensity of each Bragg peak is given by the square of the Bessel function, whose argument depends only on the amplitude of corrugation. The intensity is defined as

$$I_n(G_y) = |J_n(2\alpha)|^2 \quad (2.3)$$

Where I_n is the intensity of n^{th} diffraction order and $J_n(2\alpha)$ is the Bessel function of order n . The parameter α can be expressed as $\alpha = \frac{2\pi h_c}{\lambda_{\perp}}$ [25]; where h_c and λ_{\perp} are the corrugation amplitude and wavelength associated to the perpendicular energy of the He atoms. In this scenario, any corrugation periodic function can be written as the sum of sine or cosine series, as shown in equation 2.4.[79].

$$Z(y) = \sum_{i=1}^n h_i \sin \frac{2\pi i y}{d} \quad (2.4)$$

Here, y and d are the coordinates and the period along the transverse direction of the motion of the atom.

For a non-sinusoidal corrugation, the Intensity is derived from an integral function as,

$$I(G_y) = \left| \frac{1}{a_y} \int_0^{a_y} e^{-iG_y \cdot y} e^{-i\Delta k_z Z(y)} dy \right|^2 \quad (2.5)$$

In equation 2.5, the a_y is the channel width, and $\Delta k_z = \Delta k_{iz} + \Delta k_{fz}$ is the total momentum transfer along the normal direction of the motion of the atoms. This is the eikonal solution of purely elastic scattering[80].

Here is an example of the diffraction spectrum, along $\langle 1-10 \rangle$, $\langle 110 \rangle$, $\langle 100 \rangle$ of the ZnSe(001) surface having $c(2 \times 2)$ reconstructed surface. It is visible from the diffraction images that along $\langle 110 \rangle$, the corrugation is maximum as more Bragg peaks appear, as shown in Fig.2.19.

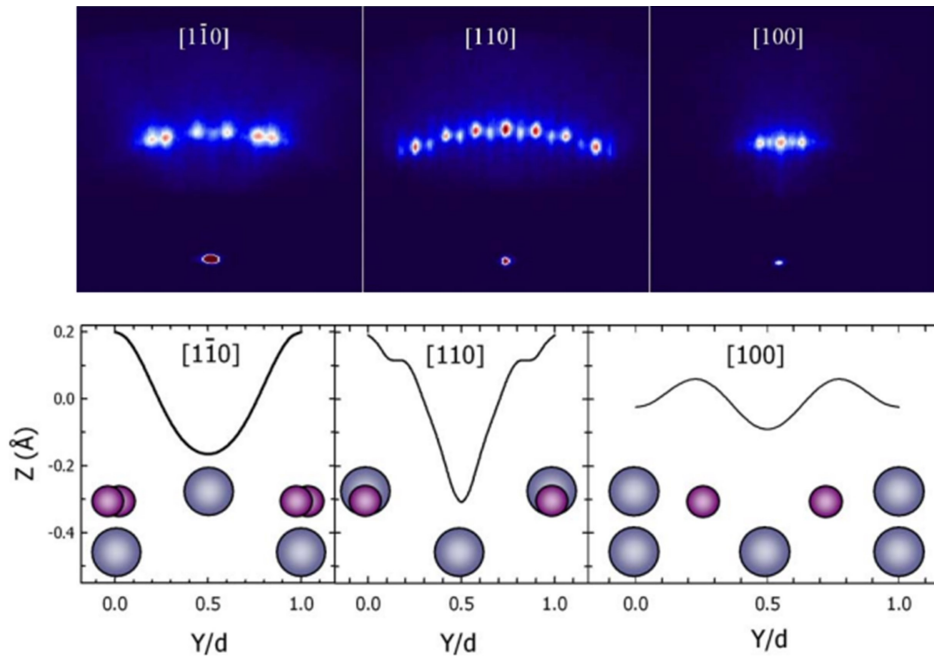


Fig. 2.19: Top: He atom diffraction at 400 eV from $c(2 \times 2)$ reconstructed ZnSe(001), along $\langle 1\bar{1}0 \rangle$, $\langle 110 \rangle$ and $\langle 100 \rangle$. Bottom: Corrugation extracted from diffraction intensities along three directions. Taken from [28]

In Fig. 2.19, the large circles are the Zn, and the small circles are the Se atoms. The interesting fact is that along $\langle 100 \rangle$, the electron density is higher on Se compared to Zn. This fact confirms the surface electron transfer from Zn to Se[81]. So GIFAD probes the electron density of the surface at a distance that is relevant for physico-chemical phenomena (adsorption, chemisorption, etc.), it is able to identify (and quantify with the theoretical support) the possible changes in the surface charge distribution.

By introducing deformation of the surface at the atomic level, like defects on the surface, thermal vibration of the surface atoms, the coherence of atom beam can be destroyed. The atoms on the surface are not ‘frozen’; their thermal displacement reduces the intensity of the diffraction signal, which produces ‘thermal decoherence’. This thermal decoherence is common to all probes (electrons, atoms, X-rays) diffracting from solids, and is described by the factor, known as the ‘Debye-Waller-Factor’ (DWF), which is defined as $DWF = e^{(-|\vec{q}|^2 \cdot \langle |\vec{u}|^2 \rangle)}$, where the parameter $|\vec{q}| = |\vec{k}_f - \vec{k}_i| = 2|\vec{k}_\perp|$ is the scattering vector, and \vec{u} is the thermal displacement of the surface atoms from the equilibrium position[68]. The mean square displacement of the surface atoms depends on the Debye temperature and mass of the atoms i.e. on materials.

In grazing conditions, the DWF expression needs to be modified due to the larger number of scattering centers along the atom trajectory.

The modified DWF in GIFAD can be expressed as $DWF = e^{(-|\vec{q}|^2 \cdot \frac{\langle |\vec{u}|^2 \rangle}{N_s})}$, where N_s is the number of scattering centers along the beam trajectory. By considering simple exponential interaction potential of surface and projectile like $V = V_0 \exp(-\Gamma z)$, where Γ and z are the stiffness constant and distance from

the surface, it can be shown that $N_s \propto \frac{1}{\theta_{in}\Gamma}$; θ_{in} is the incidence angle[82].

Thermal decoherence is always encountered—additionally, the topographic defects (adatoms, molecules, step edges, vacancies)[83] also produce decoherence. Also, the possibility to see the decoherence is due to the collisions with the background gas at a high-pressure regime ($> 10^{-6}$ mbar), where the initial coherent states produced by the surface are lost due to the collisions with the environment (background gas), which is described in detail in the next chapter (**Chapter 3**).

A recent theoretical study based on the SIVR approach has shown the effect of terraces on the diffraction spectrum. For a monolayer terrace, having an outward step produces a diffuse background above the Laue circle, and the inward step produces weaker intensity below the Laue circle (Fig.2.17-b)[84].

2.4 Experimental results

The production of the ion beam and the neutralization processes have been explained in detail in section 2. The experiment was performed with an ionic crystal LiF(001), having F.C.C. structure. The sample was cleaved in the air and immediately transferred into a UHV chamber to mount it on a five-axis manipulator. The sample was further annealed at around 300°C for a few hours in order to get a clean and flat surface. The He atoms having energy of 1 keV scattered from the surface at an angle between 0.76° and 0.78° at room temperature. Argon gas with 99.999% purity was inserted into the chamber using a leak-valve upto 10^{-2} mbar, maintaining the signal-to-noise ratio (SNR) in an acceptable value of $\approx 25:1$.

As shown in Fig.2.20, the length between the two tubes (l_2) is 65 mm, and the sample is placed between the two tubes. Here l_1 is the distance between the exit of the first tube (T_{in}) to the sample surface.

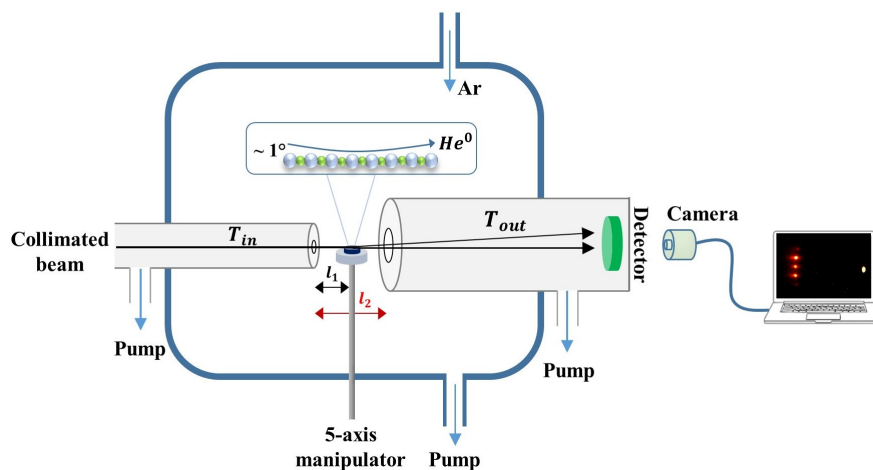


Fig. 2.20: Schematic of the main chamber of HP-GIFAD. The entrance and exit tubes are T_{in} and T_{out} . The distance between them $l_2 = 65$ mm. LiF(001) surface is shown in blue color.

Here the assumption is the pressure drops rapidly across the aperture having no pressure gradient along

the tubes. The mean free path, defined by the distance traversed by an atom between two successive collisions, is in the range of a few cm at 10^{-2} mbar of Ar gas pressure. For fast He atoms, the elastic scattering cross section on Ar has been measured between 40-850 eV [85]. The mean free path is defined as

$$l_{mfp} = \frac{kT}{p\sigma} \quad (2.6)$$

A rough extrapolation shows the measured cross-section of 1 keV He on Ar is 4×10^{-16} cm², which gives a mean free path around 10 cm at 10^{-2} mbar, longer than our system.

The diffraction images are captured along $\langle 100 \rangle$ and $\langle 110 \rangle$ crystallographic directions are shown in Fig.2.21a-d, at base pressure of 10^{-8} mbar and 5.6×10^{-9} mbar, respectively. The diffraction spectrum is obtained by projecting the intensity in between two Laue circles of polar radius $0.78 \pm 0.05^\circ$, which corresponds to a normal energy of 185 ± 23 meV, are shown in Fig.2.21-e. Fig. 2.21-f shows the normalized projected intensities. Interestingly, the normalized diffraction intensity profile remains the same even at high pressure (3.6×10^{-3} mbar).

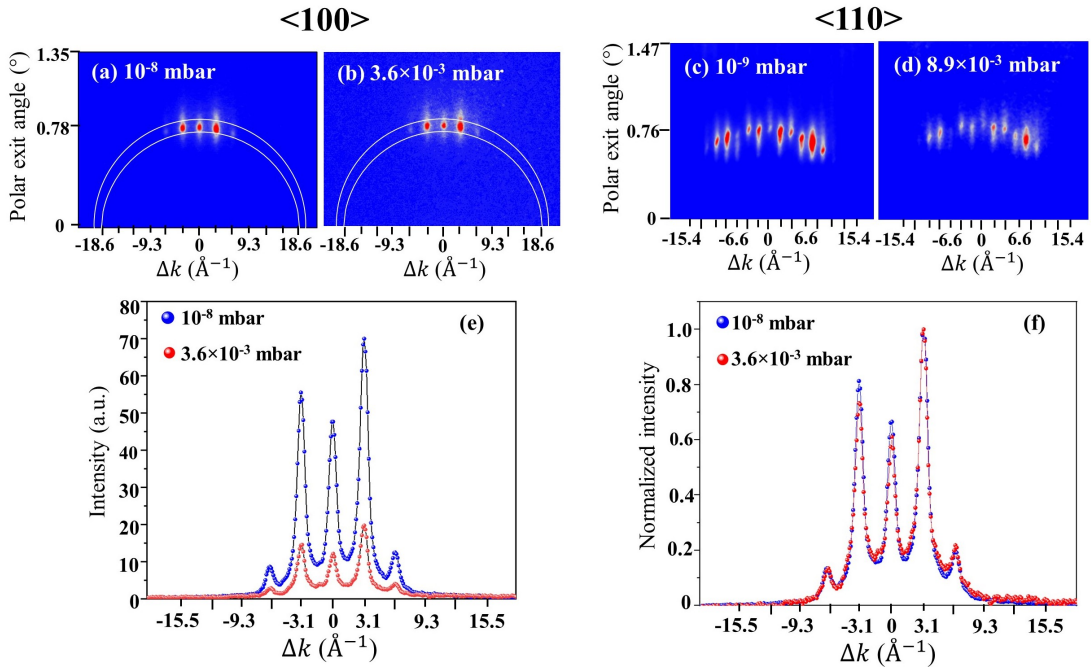


Fig. 2.21: He atom diffraction along the $\langle 100 \rangle$ direction from LiF(001) surface at (a) 10^{-8} mbar and (b) 3.6×10^{-3} mbar and along the $\langle 110 \rangle$ direction at (c) 5.6×10^{-9} mbar, and (d) 8.9×10^{-3} mbar of Ar pressure. (e) shows the projected intensities, from 2.21(a) and 2.21(b), contained between the two Laue circles superimposed on the images. (f) normalized projected intensities from (e).

2.4.1 Analysis of direct beam and scattered beams

It is visible that the diffraction signal has lost almost a factor ~ 3.5 at the pressure of 3.6×10^{-3} mbar with respect to the base pressure (10^{-8} mbar)(Fig.2.21-e). The pressure-dependent attenuation can give information about the attenuation cross section, also helps to compare different scattering processes for the direct and scattered beams. In case of the direct beam, the sample is removed from the beam path

and exposure time of camera is reduced to avoid the saturation of intensity of beam on image.

The direct beam follows a single exponential decay with pressure, and according to the Beer-Lambert's principle the decayed intensity has an expression:

$$I = I_0 \exp(-n\sigma l_2) \quad (2.7)$$

Where I_0 is the intensity measured intensity without gas, l_2 is the path length traversed by the beam, n is the density of the gas and σ is the elastic scattering cross section.

We have used a modified equation to fit the experimental data as follows,

$$I = I_0 \exp\left(-\frac{p}{p_s}\right) \quad (2.8)$$

where $p_s = \frac{kT}{\sigma l_2}$; k and T are the Boltzmann constant and absolute temperature, respectively. The parameter p_s can be obtained by fitting the experimental data, and one can derive the scattering cross-section. The parameter $p_s = 3.9 \times 10^{-3}$ mbar, leading to $\sigma = 1.5 \times 10^{-15}$ cm², assuming fast pressure drop at the entrance and the exit of the tube apertures.

The scattered beam follows a double exponential decay, as shown in Fig.2.22-b. This double exponential decay indicates two regimes of scattering, one gas-phase collision contribution and an additional scattering from the surface adsorbate species (possibly H₂O, CO₂, etc.) due to the contamination of the injected gas. This explanation is further confirmed by the fact that the scatter beam intensity could not be recovered fully after the experiment when the pressure is brought back to its initial value. The diffraction spectrum before and after the experiment is shown in Fig.2.24.

From the double exponential fitting, the decay parameters obtained yield $p_{s1} = 4.2 \times 10^{-3}$ mbar and $p_{s2} = 7.16 \times 10^{-5}$ mbar. It is interesting to note that $p_{s1} \cong p_s$ demonstrates that the direct and scatter beam undergoes a similar scattering process from the surrounding gas.

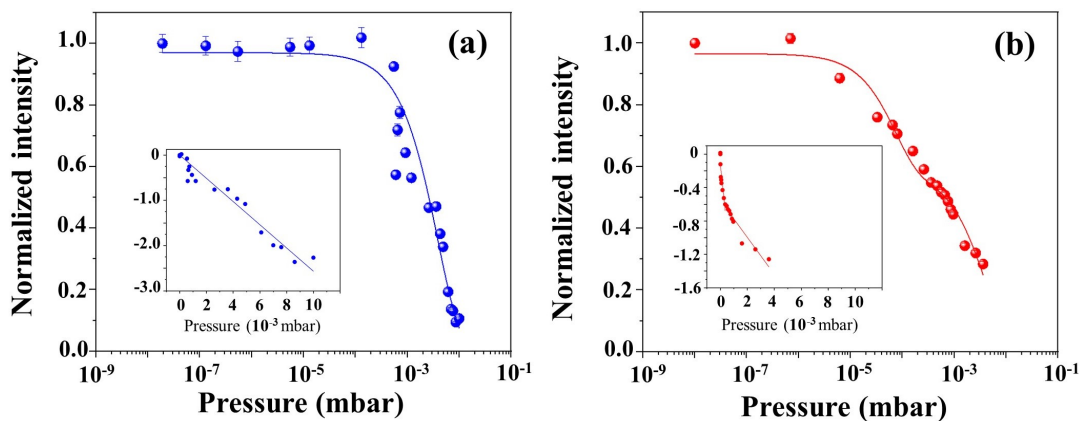


Fig. 2.22: Intensity decay of (a) the direct beam and (b) the scattered beam along the $\langle 100 \rangle$ direction; the semi-log plots are shown in the insets [$\ln(\text{Intensity})$ vs. pressure].

2.4.2 Beam divergence

The divergence of the direct beam refers to the angular measurement and quantifying the dispersion of the beam. The beam divergence has an impact on the visibility of Bragg diffraction from the surface. Ideally, the divergence of the beam must be small to have sufficient transverse coherence length.

Here, the direct beam is modeled as Gaussian distribution, and the divergence of the beam is calculated from the beam diameter. The diameter of the Gaussian beam is defined at an intensity of $\frac{1}{e^2}$ of the peak intensity[86] as shown in Fig.2.23-a.

At the pressure of 10^{-2} mbar, a clear diffraction pattern is still visible, indicating that the collision-induced broadening of the direct beam, along the path l_1 does not have a significant effect on the transverse coherence length. The divergence angle along the full beam path l_2 is almost constant up to $\sim 5 \times 10^{-4}$ mbar and then increases quasi-exponentially as shown in Fig.2.23-b. At 10^{-2} mbar pressure and based on the quasi-exponential behavior, the actual beam divergence at the sample position is that measured at 5×10^{-3} mbar, so only ~ 0.37 mrad as compared to the value of 0.32 mrad measured without the Ar gas. This weak degradation of the beam divergence explains the persistence of a well-contrasted diffraction pattern.

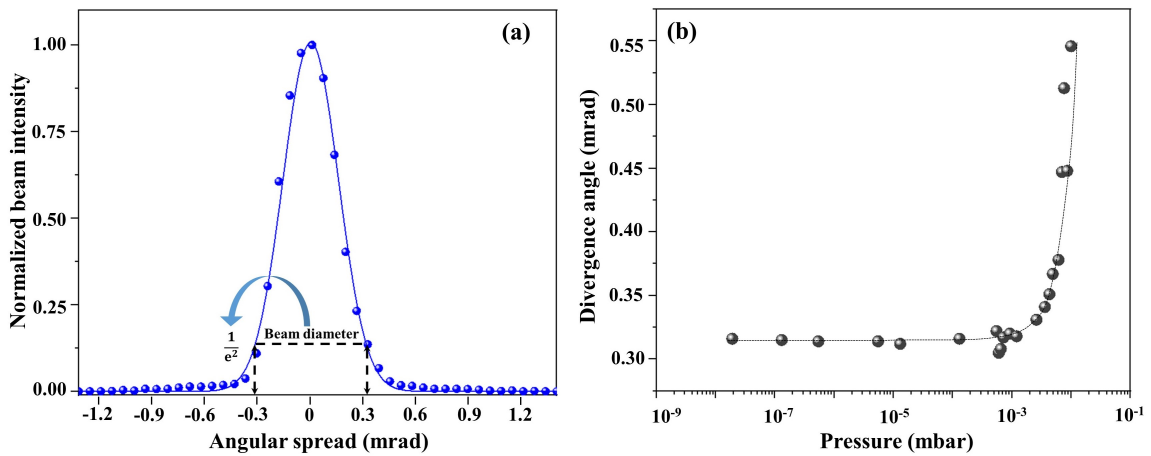


Fig. 2.23: (a) Normalized Gaussian distribution of the direct beam and the horizontal line is the intensity at $\frac{1}{e^2}$ of the maximum intensity. The data corresponds to the base pressure (10^{-8}) mbar, (b) evolution of divergence of the gaussian beam with pressure.

2.4.3 Number of collisions along the path length of beam

It is interesting to know the number of collisions experienced by the He atoms with the Ar gas along their trajectory in the high-pressure region. The mean free path is a function of pressure which can be written as $l_{mfp} = \frac{kT}{p\sigma}$ where k , T , p , and σ are the Boltzmann constant, absolute temperature, pressure, and scattering cross-section. By considering the 1 keV energy of the beam, the scattering cross-section is obtained as $\sigma = 1.5 \times 10^{-15}$ cm² (section 2.4.1.), The mean free path at 10^{-6} mbar of Ar pressure is $l_{mfp} \sim 255$ m, and the time between two successive collisions is $t_{mfp} \sim 1$ ms. The time taken by He

atoms to cross the high-pressure region is $t_{HP} \sim 0.3 \mu\text{s}$. So, the number of collisions is $P = t_{HP} \times \frac{1}{t_{mfp}} \sim 10^{-4}$. This calculation helps to give an estimation of the pressure from where multiple collisions start. This calculation predicts that there will be a single collision (He-Ar) on average at $\sim 4 \times 10^{-3}$ mbar of Ar pressure in the high-pressure zone. The effect is visible on the divergence of the beam (Fig. 2.23-b). The exponential increase of the divergence of the beam is due to the multiple collisions at high-pressure.

2.4.4 Scattered beam intensity before and after the experiments

It has been discussed in section 2.4.1. that the scattered beam intensity follows double exponential decay, one contribution comes from the simple gas phase collisions, i.e., collisions with the background Ar gas, and another is scattering from the physisorbed species. The physisorption phenomenon is further confirmed by checking the scattered beam intensity before and after the experiments.

From Fig. 2.24, it is clear that after the experiment, i.e., when the chamber pressure has been brought back to the base pressure, the surface's reflectivity is lost by almost 40% (Fig.2.24).

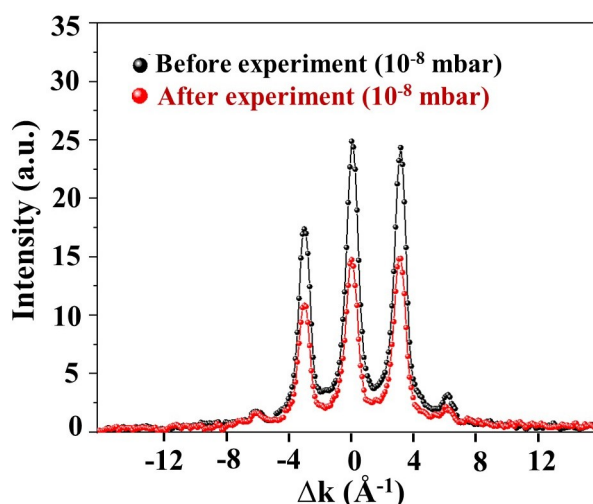


Fig. 2.24: Scattered beam intensity from LiF(001) surface before and after the experiment. Diffraction images were captured at 10^{-8} mbar of pressure.

The physisorbed species behave as defects on the surface, and a large angle scattering of He atoms with them reduces the counts on the detector, and beam intensity is dropped.

2.5 Conclusions and perspectives

Within this chapter, the newly developed high-pressure grazing incidence diffraction setup, operational principles, and experimental findings are discussed. Here we have demonstrated that grazing incidence diffraction of fast He atoms from a clean, crystalline surface can be observed at surrounding Ar gas pressure as high as 10^{-2} mbar. Notwithstanding the fact that, the direct beam intensity has lost 90% of its intensity at this pressure, and that the available differential cross-section for He scattering on Ar[87]

drops by less than a factor of 3 in amplitude between zero and 0.05° scattering angles, the coherence width remains sufficient for preserving diffraction. Interestingly, calculations performed by Karlovets et al.[88] on the elastic scattering of an electron wavepacket on a hydrogen atom show a clear effect of the wave packet transverse size (i.e. transverse coherence width) of the differential cross-section; large angle contributions to the later decreases with increasing transverse coherence width. These results have been further confirmed by Sarkadi et al.[89] on the scattering of 75 keV protons on atomic hydrogen. Although a detailed analysis on the effect of beam coherence on the final beam divergence is well beyond the scope of this work, high beam collimation conditions seem to represent an effective way to prevent decoherence.

This new high-pressure GIFAD configuration, which we name HP-GIFAD, offers many opportunities for the study of surface reactivity and should also represent an alternative diffraction tool for monitoring thin film growth in real-time in high-pressure conditions. For surface structure characterization, the He probe has been selected for its inertness; this key property is also favorable in limiting gas phase interactions with the surrounding species.

Real-time monitoring during thin film growth has always been a challenge. Reflection High Energy Electron Diffraction (RHEED) showed powerful in monitoring film growth in Molecular Beam Epitaxy chambers [90]. In its high pressure version, RHEED has seen its use extended to other deposition modes, such as Pulsed Laser Deposition[91] or Atomic Layer Deposition[33]. In a layer-by-layer growth mode, RHEED provides a direct information of film thickness through oscillations of the reflected intensity [92]. Despite some complex attempts[93], application of RHEED in MS suffers severe limitations because of the stray electromagnetic fields. HP-GIFAD may thus offer an alternative solution for accessing film growth properties (growth mode, crystalline structure, defect density). Due to the extreme GIFAD sensitivity to surface defects, it should provide valuable insight into the influence of plasma parameters on the growing film. However, substrate contamination plays a pivotal role in thin film depositions, and the quality of the film is also affected. So, the UHV approach (leak-free system, baking, selection of materials, etc.) is the best solution to keep the substrate as well as the growing layer free from contamination; this scheme naturally implies the use of a high-purity process gas. This benefit might be decisive for the more challenging case of HiPIMS (High Power Impulse Magnetron Sputtering), a recent variant of Magnetron Sputtering deposition(MSD). HiPIMS produces better films with greater density and crystallinity, but its development is hindered by the complexity related to the large number of adjustable parameters (pulse power, pulse duration, duty cycle, argon gas pressure, oxygen pressure for reactive sputtering, substrate temperature, ion acceleration). So, the HP-GIFAD could be very effective in precisely controlling the growth process in HiPIMS.

Chapter 3

Observation of collisional decoherence using Grazing Incidence Fast Atom Diffraction

Overview

‘Entanglement’ and ‘Quantum decoherence’ address the fundamental problems in quantum information theory and have become an interesting field of research nowadays. The decoherence process can be considered as an entanglement of the quantum system with its environment. Decoherence has been observed in atom interferometers and in macroscopic superconducting circuits, etc. Decoherence from the surface has already been seen using GIFAD (low-pressure GIFAD). The newly developed high-pressure GIFAD system (HP-GIFAD) is suitable for observing decoherence in the gas phase due to its high operational pressure ($\approx 10^{-2}$ mbar). The collisions destroy the coherent states produced by the interaction between He atoms and surface atoms, and in the far field, the interference pattern disappears. In this chapter, the experimental results of collision-induced decoherence are discussed.

3.1 Introduction

The theoretical work of H. Zeh[94] in 1970 opened up a new field of research on quantum decoherence[95]. Decoherence is considered as a quantum noise, that happens due to the transformation of pure states to mixed states due to the entanglement between quantum system and environmental degrees of freedom. Several processes are involved in the different types of decoherence[70, 96] and mathematically in the decoherence process, the off-diagonal elements in the reduced density matrix representation die out[97], and transition happens from quantum to the ‘classical world’(Appendix C). The interaction of the initially prepared quantum states with their environment[98] leads to the loss of information in an irreversible

way. From the classical physics point of view, the environment is considered as a disturbance or noise that perturbs the system. Novel experimental techniques have given the opportunity to see decoherence in QED[99], matter-wave interferometry[100], superconducting systems[101], and ion traps[102].

Decoherence due to collisions has been observed in the Talbot-Lau[70], and Mach-Zehnder interferometer [100], where visibility of the interference fringes is reduced with the background gas pressure. The Talbot length gives an idea about the near field region, where any collision can transfer information about the path information, which introduces decoherence, and one can observe the reduction in fringe visibility. The contrast and the ‘which-way’ information are related to each other; the better distinguish the paths, a less contrasted pattern will appear[103]. The term ‘the path’ or ‘which-way’ refers to the particle’s classical trajectory; accessing this information causes decoherence[104]. However, there is a debate about the relation between the uncertainty principle and decoherence. Decoherence can also be well explained using Heisenberg’s uncertainty principle, where the measurement of the spatial information enhances the uncertainty in momentum space, and the interference pattern disappears—the ‘path’ information is accessible by measurement in the ‘near-field’ region.

Rare gas atoms can be used as ideal probes to understand atom-surface interactions. The neutral scattered beams from the surface exhibit diffraction phenomenon, thereby satisfying the basic quantum principles contained in the de Broglie hypothesis. Therefore, particle-surface interactions in the quantum regime represents a suitable platform for studying decoherence.

The pioneering work of Estermann and Stern[42] based on thermal neutral atom scattering has become a surface analysis technique known as HAS or TEAS. There are different decoherence phenomena that occur in particle-surface scattering. At thermal energies, the coupling to the surface phonons leads to the thermal decoherence, which is the primary source of decoherence. In addition, scattering from surface defects, adsorbates, and at higher energy (in GIFAD) the probability of electronic excitations produces decoherence. Grazing Incidence Fast Atom Diffraction (GIFAD)[25, 29] is a comparatively new surface analysis technique where the neutral atoms having energies between 0.2-5 keV are scattered from the surface at an angle typically below 1° . The grazing geometry makes GIFAD more sensitive to the topmost layer of the surface. The universality of this technique allows one to observe diffraction from metals[105], semiconductors[51], insulators[25], oxides[26] and fragile organic layers[27].

The newly developed high-pressure GIFAD (HP-GIFAD) set-up[106] can operate at high pressure ($\approx 10^{-2}$ mbar), which is suitable to observe the decoherence due to gas phase collisions. Atom diffraction can be well explained due to the quantum scattering of atoms from surfaces where the surface behaves as a diffraction grating that prepares superposed states that produce in a far field an interference pattern (Bragg peaks). The trajectories behind the slits (in transmission mode) produce a ‘quantum carpet’ called the Talbot pattern. This pattern starts to disappear after the near field region and Bragg channels appear

and the trajectories are accumulated along these channels. In the decoherence process, the interaction of the wave packets with its environment produces a random phase shift, and the interference pattern is lost after superposition. Another way of considering decoherence phenomenon is to consider that the momentum transferred to the collision partner can be used to locate the interaction (which ‘path’ information).

In our case, the intensity distribution of the scattered atoms contains the diffraction pattern consists of sharp peaks due to the quantum scattering from the surface, which can be modeled with Lorentzian functions and a classical background, modeled as Gaussian functions. The transition from one to another is controlled by coherent fraction (μ). It is interesting to trace over the parameter μ with pressure to have an idea about the decoherence process

3.2 Experimental results

The experiments have been performed inside an Ultra-High-Vacuum (UHV) system having a base pressure of 10^{-9} - 10^{-8} mbar. A LiF(001) surface was cleaved in the air and transferred immediately to the UHV chamber on the five-axis manipulator system. To get a clean and flat surface the sample was annealed at 300°C for a few hours.

The procedure for producing a neutral He beam has been discussed in **Chapter 2**. To observe decoherence, Ar gas was introduced inside the main chamber, and the intensity distribution of the scattered particles was captured up to 10^{-3} mbar of pressure.

3.2.1 Influence of pressure on the diffraction pattern

3.2.1.1 Lateral profile

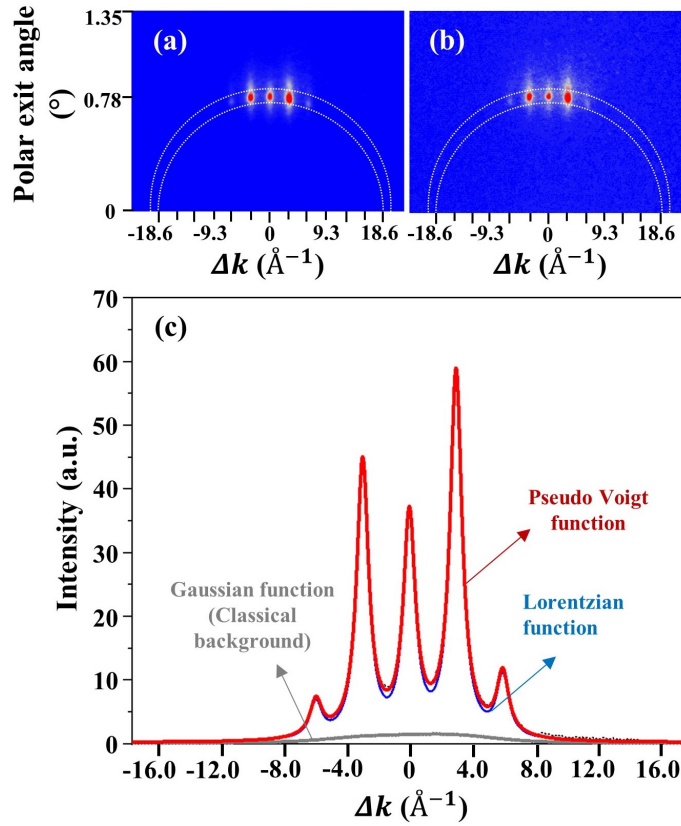


Fig. 3.1: He atom diffraction from LiF (001) surface along the $\langle 100 \rangle$ direction at (a) 10^{-8} mbar, (b) 3.6×10^{-3} mbar and (c) projected intensity of (a) fitted with Pseudo Voigt function.

The diffraction images are shown in Fig.3.1 at (a) 10^{-8} mbar and (b) 3.6×10^{-3} mbar of Ar pressure. The intensity of the diffraction signal at 10^{-8} mbar of pressure is projected along the Laue circles, which is shown in Fig.3.1-c. The fitted intensity profile has two components. One arises from the classical scattering and is modeled as the Gaussian function (G), and the other corresponds to the coherent part of scattering- it is modeled by a Lorentzian function (L), as shown in Fig. 3.1-c. The intensity profile is fitted with multiple Pseudo Voigt (PV_m) functions, which is a good approximation of the Voigt function that results from the convolution of Lorentzian and Gaussian functions expressed as,

$$PV_m(x) = y_0 + \mu \times L_m(x) + (1 - \mu) \times G_m(x) \quad (3.1)$$

where m stands for multiple function (for multiple peaks); $L_m(x)$ and $G_m(x)$ can be expressed as,

$$L_m(x) = \sum_n A_n \left[\frac{2}{\pi} \frac{w_L}{4(x - x_0 - nx_c)^2 + w_L^2} \right] \quad (3.2)$$

$$G_m(x) = \sum_n A_n \left[\frac{1}{w_G} \sqrt{\frac{4 \ln 2}{\pi}} e^{-\frac{4 \ln 2 (x - x_0 - n x_c)^2}{w_G^2}} \right] \quad (3.3)$$

Therefore, the explicit way to express the multiple peak function $PV_m(x)$ is

$$PV_m(x) = y_0 + \sum_n A_n \left[\frac{2\mu}{\pi} \frac{w_L}{4(x - x_0 - n x_c)^2 + w_L^2} + \frac{1 - \mu}{w_G} \sqrt{\frac{4 \ln 2}{\pi}} e^{-\frac{4 \ln 2 (x - x_0 - n x_c)^2}{w_G^2}} \right] \quad (3.4)$$

Where y_0 is the background noise, n is the order number of diffraction peaks (positive and negative with respect to the central peak). A_n is the amplitude of the n^{th} peak, μ is the coherent fraction; w_L and w_G are the Lorentzian and Gaussian width; x , x_0 and x_c are respectively the variable, the position of the 0^{th} order peak, and the peak spacing.

The advantage of using the Pseudo-Voigt function is that the coherent fraction quantifies the relative contribution from coherent scattering, is simply provided by the parameter μ . In this experiment, the idea was to follow the evolution of μ over the pressure. To determine the different possible contributions to decoherence, different zones are considered along the beam trajectory, as depicted in Fig.3.2.

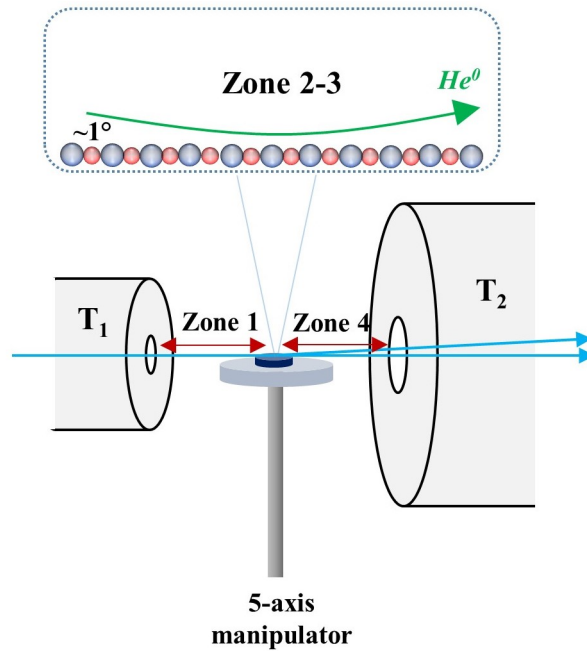


Fig. 3.2: The main chamber of the HP-GIFAD setup with different zones is considered in the discussions. T_1 and T_2 are the entrance and the exit tubes with diameters $150 \mu\text{m}$ and 4mm respectively. The LiF(001) sample is shown in blue color.

In zones 1 and 4, the scattering of the He atoms on the Ar gas leads to the attenuation of the beam intensity. Although zones 1 and 4 could produce decoherence based on the change in coherence length of the primary beam and decoherence from far-field respectively. Zone 2 and 3 are regions where the two processes occur: scattering and decoherence. Zone 2, with a length of 10-50 nm, is where the incoming He atoms exchange momentum with the surface. The collisions with the physisorbed species

on the surface lead to both beam attenuation and decoherence. Zone 3 is comparatively larger than zone 2, $\approx \mu m$ scale, named as near field region where any collision leads to decoherence and the path information can be obtained. The zoom-in view of zones 2 and 3 are shown below (Fig.3.3).

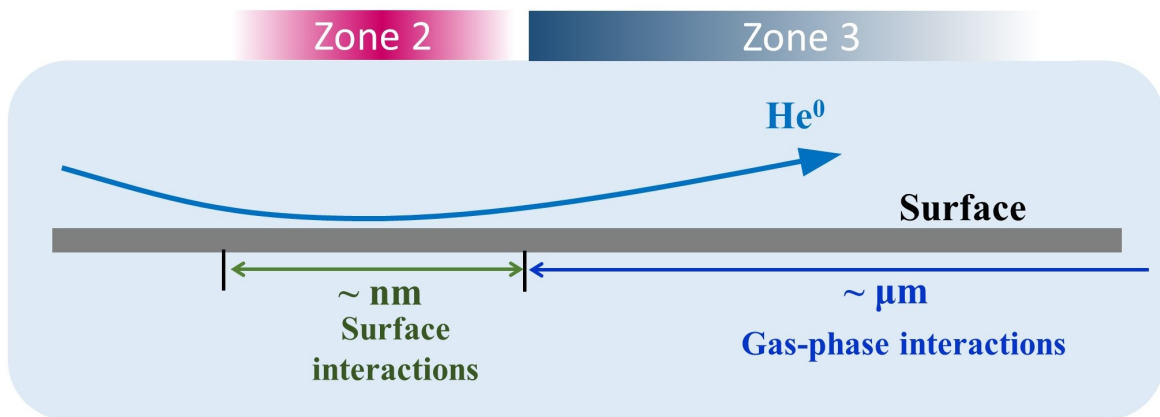


Fig. 3.3: Zoom-in view of zone 2 and 3.

Images, such as those shown in Fig.3.1a-b, were captured at different pressures and fitted with Pseudo Voigt functions according to the expression of 3.4, The decay of the coherent fraction μ over the pressure follows a double exponential function, as a single exponential does not provide a good fit, shown in Fig.3.4.

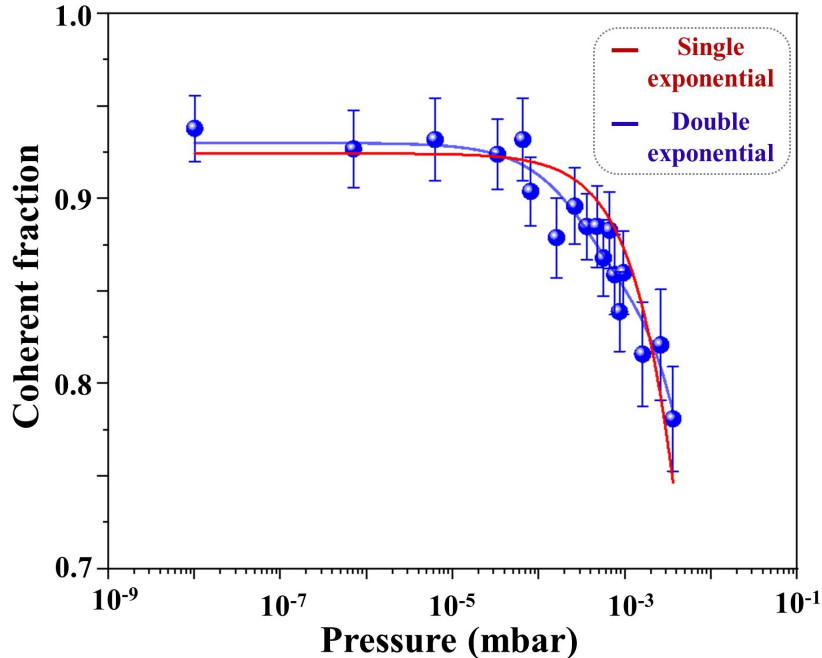


Fig. 3.4: Single and double exponential fitting of coherent fraction data.

One may consider that the quantum states in the momentum space are blurred due to the random momentum change of the He atoms with its environment. The theoretical models on the decoherence theory can well explain the loss of coherence using the decoherence function[107]. The simplest way to represent

the loss of visibility with pressure in the atom interferometers can be modeled as

$$V(p) = V_0 \exp\left(-\frac{p}{p_0}\right) \quad (3.5)$$

Where the loss of coherence with background gas pressure has been described by a single exponential decay with the parameter p_0 , known as ‘decoherence pressure,’ which is related to decoherence cross-section σ_d and scattering length l . The equation 3.5 has the same form of Beer-Lambert[108] type describing the decoherence instead of beam attenuation. In our case, the scattering length is the length of the near field zone.

In our experiment, the decay of the coherent fraction μ with pressure is shown in Fig.3.5-a. The fitting equation can be modeled as

$$\mu(p) = \mu_1 \exp\left(-\frac{p}{p_1}\right) + \mu_2 \exp\left(-\frac{p}{p_2}\right) \quad (3.6)$$

Where μ_1, μ_2 are the amplitudes and p_1, p_2 are known as ‘decoherence pressure.’ The double exponential decay has been considered due to the two different contributions, the interaction of He with background gas (Ar) and with physisorbed species on the surface. Fig.3.4 shows a comparison of fitting of coherent fraction vs. pressure using single and double exponential functions.

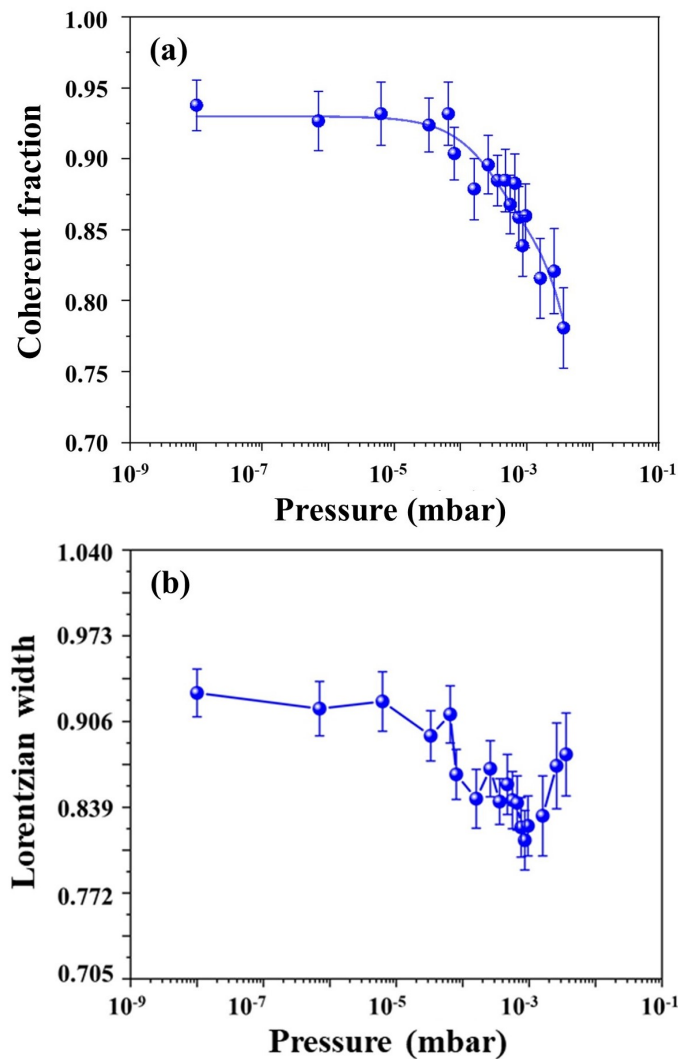


Fig. 3.5: (a) Decay of coherent fraction and (b) behavior of Lorentzian width with pressure. $1\text{\AA}^{-1} = 0.06^\circ = 1.04\text{ mrad}$. Data is shown here for $60\ \mu\text{m}$ slit size.

The Lorentzian width (Bragg peak width) behavior shows an anomalous behavior. It has decreasing and increasing tendencies, as shown in Fig. 3.5-b. More constructive remarks and possible sources of peak narrowing are discussed in the conclusion (section 3.4).

3.2.1.2 Polar profile

The surface atoms are not in frozen positions. In GIFAD, it is considered that the motion of the surface atoms due to the thermal vibration is much slower than the fast He atoms. So, it can be considered that the surface atoms are at rest with respect to the incident He atoms. The elongated streak on the diffraction images (Fig.2.21) can be considered as an inelastic contribution due to the thermal vibration, step edges, or other topographic defects.

The polar distribution of the diffraction pattern consists of a symmetrical Lorentzian profile (L) and two asymmetrical Log-normal (LN) distributions, as shown in Fig.3.6. In this case, two Log-normal functions are used to fit the spectrum where the width of one is larger compare to another (Fig.3.6).

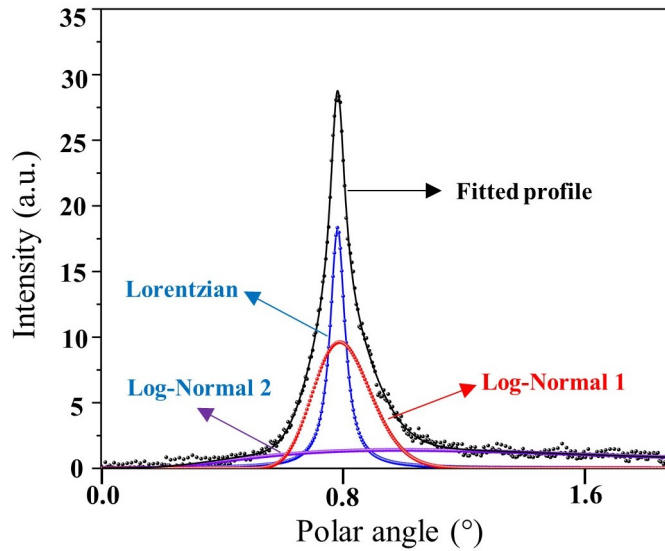


Fig. 3.6: Polar distribution fitted with Lorentzian and Log-normal profile. Spectrum is at 10^{-8} mbar.

Generally, one Log-normal (LN) produces the elongated streaks due to the inelastic contribution to the diffraction and one, much wider, for the classical scattering from defects. The Lorentzian (L) curves describe the elastic diffraction peak.

The Lorentzian function has the expression

$$L = \frac{2B}{\pi} \frac{w_L}{4(x - x_c)^2 + w_L^2} \quad (3.7)$$

Here w_L , B , x_c are the Lorentzian width, amplitudes, and central position of the Lorentzian distribution and Log-normal (LN) has an expression

$$LN = \frac{A}{\sqrt{2\pi}w_n x} \exp\left(-\frac{\ln\left(\frac{x}{x_{c1}}\right)^2}{2w_n^2}\right) \quad (3.8)$$

Where A , w_n , and x_{c1} are the amplitude, width and central position of the Log-normal distribution. So, the fitted function is

$$y(x) = y_0 + \frac{2B}{\pi} \frac{w_L}{4(x - x_c)^2 + w_L^2} + \frac{A_1}{\sqrt{2\pi}w_{n1} x} \exp\left(-\frac{\ln\left(\frac{x}{x_{c1}}\right)^2}{2w_{n1}^2}\right) + \frac{A_2}{\sqrt{2\pi}w_{n2} x} \exp\left(-\frac{\ln\left(\frac{x}{x_{c2}}\right)^2}{2w_{n2}^2}\right) \quad (3.9)$$

x is the variable in the above equations. The camera noise has been considered and parameterized as y_0 , 1, and 2 suffixes are used to show two Log-normal.

We have observed previously (lateral profile) that the Lorentzian contribution to the diffraction pattern along the lateral direction gets narrower as pressure increases up to 10^{-3} mbar, and above this pressure, the width has broadening tendency. As this is unexpected, it is interesting to confirm this behavior along the polar direction. From Fig.3.7, we can see a similar trend, with an even more pronounced decrease as

compared to the lateral direction; this is visible on both the specular and the 1st order peaks.

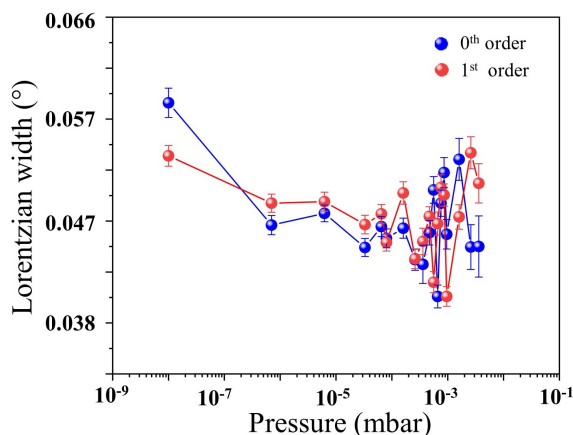


Fig. 3.7: Dependency of the Lorentzian width with Ar pressure along the polar direction

The minimum of the peak width is around $\sim 10^{-3}$ mbar, which is consistent with the lateral profile data set. We can thus conclude that the narrowing of the elastic contribution to the Bragg peaks is a robust observation.

3.2.2 Decoherence from surface

3.2.2.1 Analysis of perylene deposition on Ag(110)

The most successful application of GIFAD is in-situ growth monitoring of thin film growth in UHV [37]. Time evolution of the surface reflectivity, i.e. the relative intensity of the scattered beam, as the simplest parameter measured in real-time, provides rich information on the growth mode (as described in **Chapter 1**). Due to the very grazing geometry, any topographic anomaly (step edges, adatom or molecule, voids, island, etc.) produces a large angle scattering of the incident He atoms, away from the specular direction (Fig.3.8). These atoms do not reach the detector and, therefore produce a loss of the reflected intensity. This latter parameter is then a good measure of the surface flatness. In the layer-by-layer growth mode, we can thus observe an oscillatory behavior of the reflectivity; whenever a new layer is completed, the reflectivity reaches a peak value; a minimum value is reached typically at $(n+\frac{1}{2})$ layer. The number of oscillations in the reflected intensity corresponds exactly to the number of grown layers. In addition to a reduction of the reflectivity, topographic defects also reduce the coherence length of the surface. As a consequence, the coherent fraction in the scattered beam is also reduced.

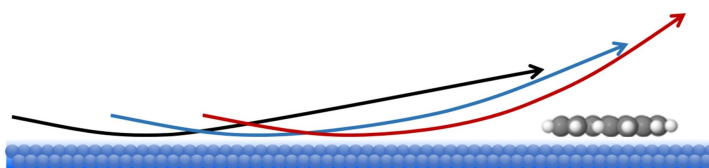


Fig. 3.8: Schematic of He atom scattering from surface adsorbates.

The growth of an organic perylene monolayer on Ag(110) has been studied previously by the group[27]. As observed by many authors[109, 27], the growth does not proceed by nucleation as most often observed for inorganic layers but by continuous densification through a gas-liquid and liquid-crystal phase transition. The relative surface reflectivity evolution with deposition time is shown in Fig.3.9. The He atom beam has a primary energy of 500 eV and is aligned along the $\langle 1-10 \rangle$ crystallographic direction. The reflectivity first decreases at start of deposition until a minimum is reached at 2300 s, which roughly corresponds to a half of a monolayer. As deposition goes on, the voids (bare substrate) between perylene molecules get filled, so that the covered surface represents a continuously increasing fraction. The peak is reached when the perylene monolayer perfectly wets the substrate. For the analysis, we only consider the data between 0 and 1050 sec., where the reflectivity loss is 30% of its initial value as shown by the blue box. This is precisely the region where the diffraction pattern from the substrate remains visible and well resolved.

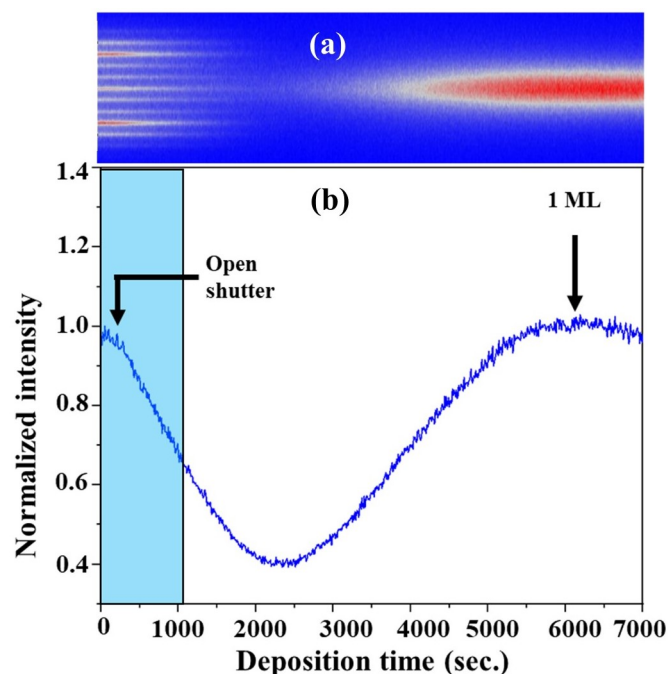


Fig. 3.9: Deposition of perylene on Ag (110) surface. (a) Time evolution of scattered beam intensity from Ag(110) surface along $\langle 1-10 \rangle$ direction during perylene deposition, (b) variation of the reflectivity from the surface over the deposition time. Experiments were performed at 500 eV energy of He atom. ML: Mono Layer.

We follow exactly the same procedure as described in the previous section 3.2.1 for the image treatment and analysis of the diffraction pattern. We then derive the evolution of the coherent fraction (μ) and the peak width (Lorentzian width) with the deposition time. The diffraction spectrum and fitted profile of Ag are shown in Fig.3.10.

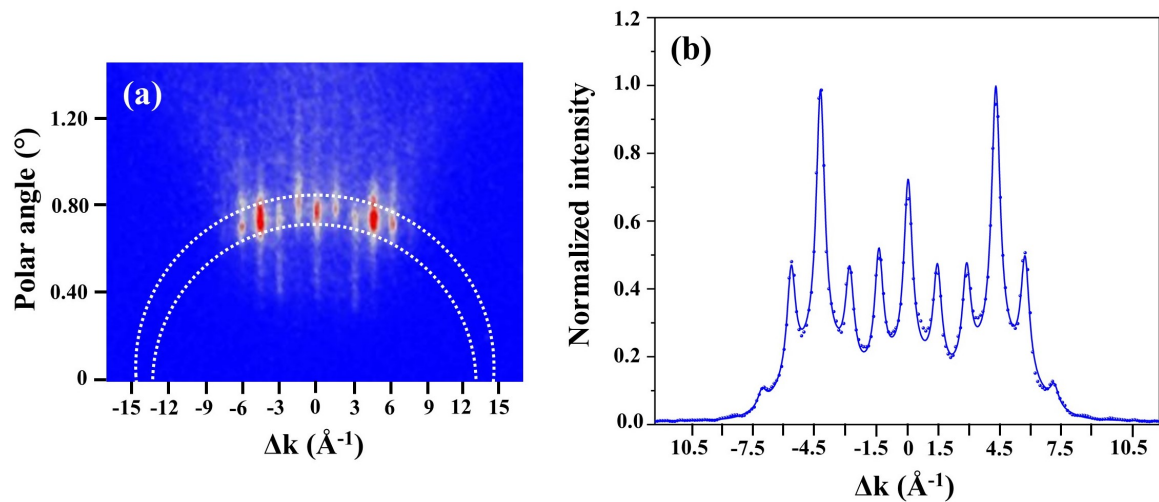


Fig. 3.10: (a) He atom diffraction from Ag(110) along $\langle 1-10 \rangle$ direction, (b) normalized fitted diffraction spectrum projected in between Laue circles.

The $\langle 1-10 \rangle$ direction of Ag is highly corrugated, which can be understood from the diffraction spectrum. We have observed diffraction peaks up to order ± 6 at 150 meV normal energy. As shown in Fig.3.11-a, the coherent fraction (μ) decays over the deposition time, while the Lorentzian peak width of Ag shows an increasing tendency. We conclude that, for perylene adsorbates, a decrease in surface coherence length translates into a decrease of the coherent fraction in the scattered beam and simultaneously a pronounced widening of the elastic contribution (Lorentzian peak) to the diffraction signal.

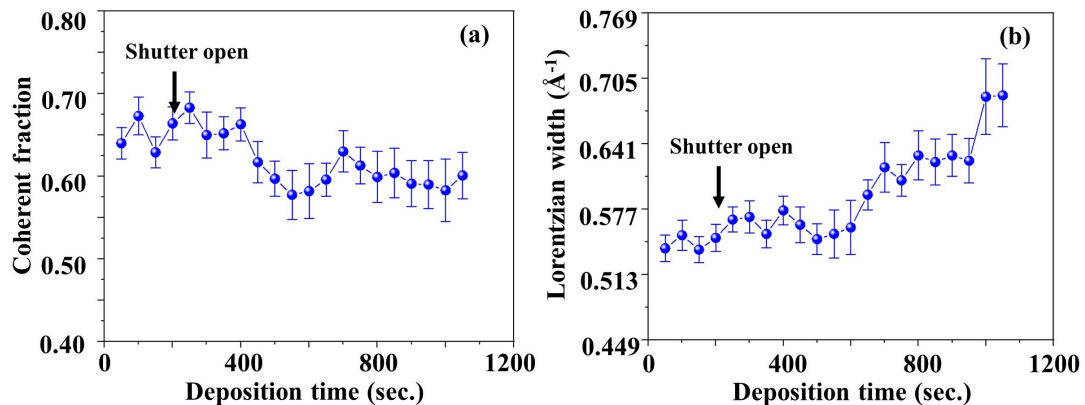


Fig. 3.11: (a) Decay of coherent fraction (b) evolution of Ag peak width with deposition time.

3.2.2.2 Analysis of KCl deposition on Ag(001)

The deposition of the inorganic compound KCl on Ag (001) has been analyzed in order to see the decay of coherent fraction (μ) and the evolution of the Lorentzian width with the deposition time of KCl. For the analysis, the images are considered up to 320 sec., where the reflectivity loss is 30% of the initial value, as shown in Fig.3.12-b. The deposition was started after opening the shutter of the evaporator at 200 seconds, as shown in Fig.

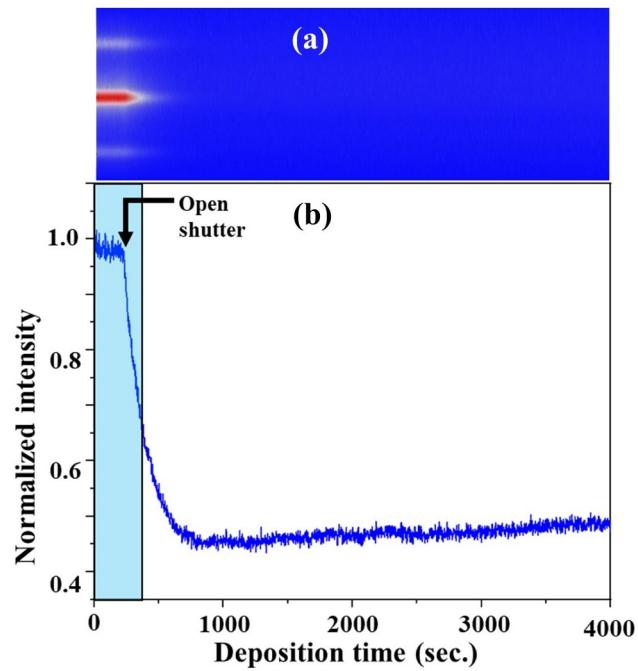


Fig. 3.12: Deposition of KCl on Ag (001) surface. (a) Time evolution of scattered beam intensity from Ag(001) surface along $\langle 110 \rangle$ direction during KCl deposition, (b) variation of the reflectivity from the surface over the deposition time of KCl.

It has been found that the coherent fraction decays over time in a non-linear fashion after opening the shutter, but the broadening of the peak width is not prominent like in the deposition of perylene on Ag(110), as shown in Fig.3.13-a-b. The rapid decrease of the coherent fraction is prominent after 200 sec. after opening the shutter (Fig.3.13-a).

The rapid loss of reflectivity over the deposition time (Fig.3.12-b) is due to the island growth of KCl from the initial stage. As a result, the reflectivity drops rapidly and then stabilizes at a constant level, preventing it from reaching maximum value.

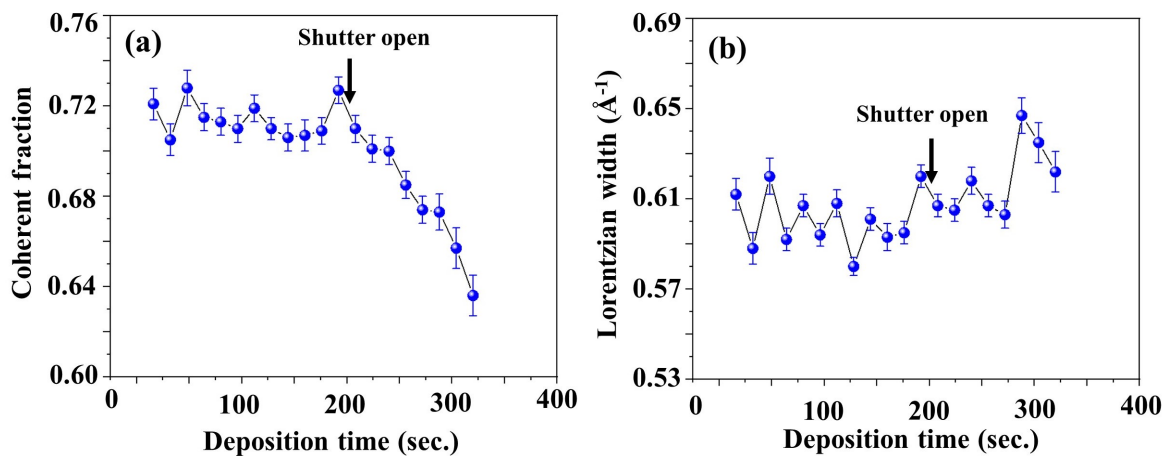


Fig. 3.13: (a) decay of coherent fraction over the KCl deposition time and (b) behavior of the Lorentzian width during the deposition time.

GIFAD can also give insights into the different growth modes of thin film. As already discussed, in the case of perylene deposition, we have seen the recovery of the scattered beam intensity from the surface, which confirms the layer-by-layer or 2D growth mode of perylene on Ag. In the case of KCl deposition on Ag, the growth was in the island or Volmer-Weber or 3D mode.

3.2.3 Decoherence with large slit size

The Lorentzian peak width is directly related to the width of the wavepacket and, therefore, to the transverse coherence width of the primary beam. As explained in **Chapter-2**, the latter can be simply adjusted from the collimation slit at the exit of the neutralization cell; increasing slit size reduces the spatial coherence length, while beam divergence gets larger.

The dependence of the Lorentzian width and the coherent fraction with the slit size is shown in Fig.3.14. We observe that when the slit size is increased by 50%, from 60 to 90 μm , the decay of the coherent fraction is faster (Fig.3.14-b). The fitted parameters are $p_1 = 3.2 \times 10^{-2}$ mbar and $p_2 = 2.9 \times 10^{-4}$ mbar for 60 μm slit width. The parameters are found as $p_1 = 2.6 \times 10^{-2}$ mbar and $p_2 = 8.7 \times 10^{-5}$ mbar in case of 90 μm slit width. The Lorentzian peak width follows a similar trend but with a steeper decrease of $\sim 16\%$ in the case of 90 μm slit size. It is visible from the initial peak width that the beam diameter increases with the increase of slit size. In Fig.3.14-a, the Lorentzian width is normalized to the 90 μm slit width. For both collimation slits, a minimum width is reached at a pressure of 8×10^{-4} mbar, so very close to the onset of the fast increase of the direct beam as shown in Fig.2.23-b in **Chapter-2**.

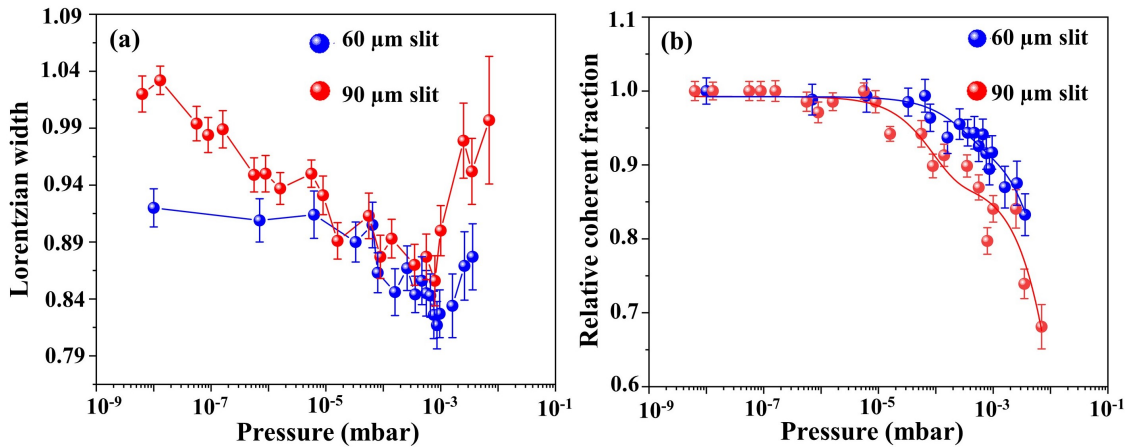


Fig. 3.14: Comparison of the (a) variation of peak width and (b) decay of coherent fraction with pressure with different slit sizes.

3.2.4 Dependency of intensity attenuation and decoherence

The best way to separate the loss of beam intensity and the loss of coherency is to see the dependency between them, as shown in Fig.3.15. Here the data is shown for 60 μm slit.

It is interesting to notice that the beam intensity drops rapidly compared to the coherent fraction. How-

ever, in the experiment with the Mach-Zehnder interferometer[100], the loss of contrast has a non-linear dependency with the attenuation. The interesting finding is that although the beam intensity is 34% of its initial value (66% loss), the coherence loss is only $\sim 14\%$.

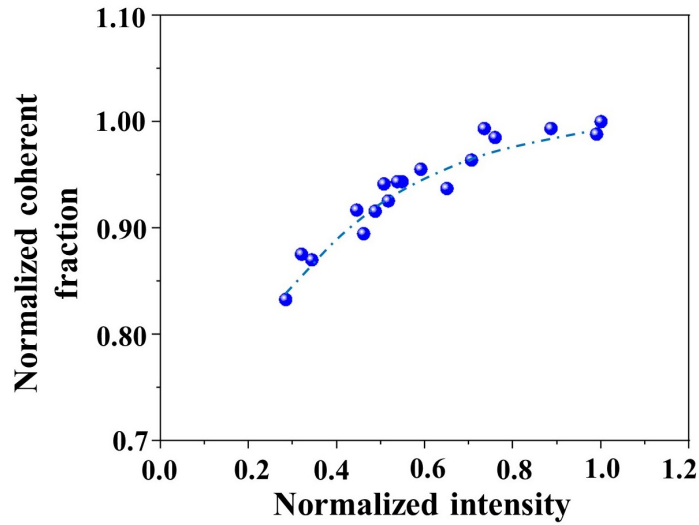


Fig. 3.15: Decay of relative coherent fraction with relative intensity for 60 μm slit width. The dotted line is used to guide the eyes.

This observation can provide the information that most of the scattering contributes to the loss of intensity rather than loss of coherence.

3.3 Near field region- an overview

In classical wave optics, two diffraction regimes can be considered, near-field and far-field diffraction, depending on the effect of Fresnel and Fraunhofer diffraction. The curvature of the wavefront has to be taken into account in the case of Fresnel diffraction. A similar effect is observed in the case of atom optics, but mostly, the far field is considered. The far field is considered when the diffraction pattern is extended well beyond the array of the slits.

The near-field region is interesting due to the ‘self-imaging’ [110] effect, which is a reconstruction of grating periodicity over a certain distance along the beam transmission. This self-imaging of a diffraction mask was discovered by Henry Fox Talbot around 1836, which is known as the Talbot effect. Later, Lord Rayleigh explained this effect theoretically. When the diffraction grating is illuminated with the parallel rays of light The self-image of the grating is observed at an integer multiple of Talbot length (L_T), which depends on the periodicity (d) of the grating and wavelength (λ) of the illuminating source, expressed as $L_T = d^2/\lambda$.

It is also possible to produce the self-imaging effect with an incoherent source [110]. An additional grating downstream from the first one produces sufficient beam coherency. This two grating configuration is known as Talbot-Lau system. This configuration is used in atom interferometry as a lensless imaging

system known as Talbot-Lau interferometer.

In atom diffraction, we consider any diffracting surface behaves as a reflective grating. When this quantum grating is illuminated with continuous wavefronts, the quantum flow behind the grating produces a pattern called ‘quantum carpet’[111]. At the even integer, multiple of Talbot length L_T , the maxima and minima appear according to the slit openings. For the odd integers, it is shifted half of the grating period as shown in Fig.3.16[110].

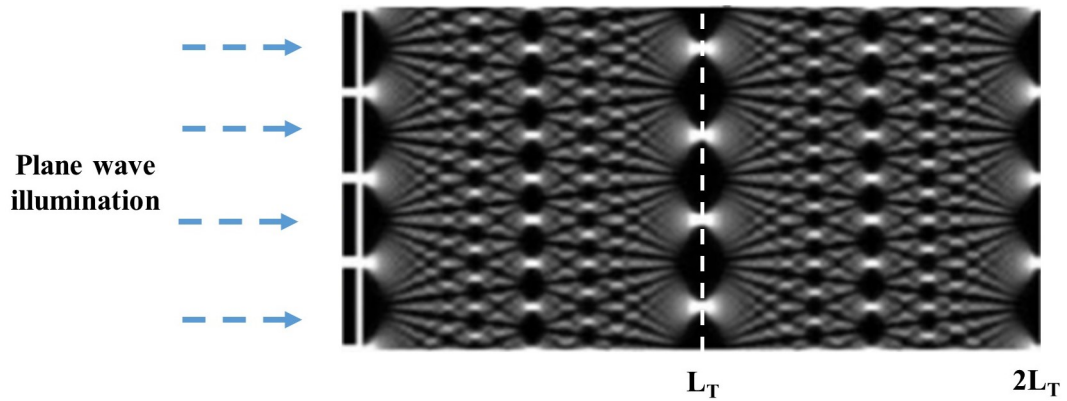


Fig. 3.16: *Optical Talbot effect using monochromatic light and the Talbot carpet. The revival of the images happen at the integer of Talbot length at the right.*

In between, the fractional Talbot images are observed at all rational multiples of Talbot length, like $L = (p/q) \times L_T$, where p and q are the integers. The near field zone is considered up to where this self-imaging is observed (Fig.3.17-f). Near field zone has a dependency on the array of illuminating slits. It has been observed that with the increase of number of slits, the near field zone is extended. Higher number of Talbot orders can be observed with higher number of slits as shown in Fig. 3.17[112].

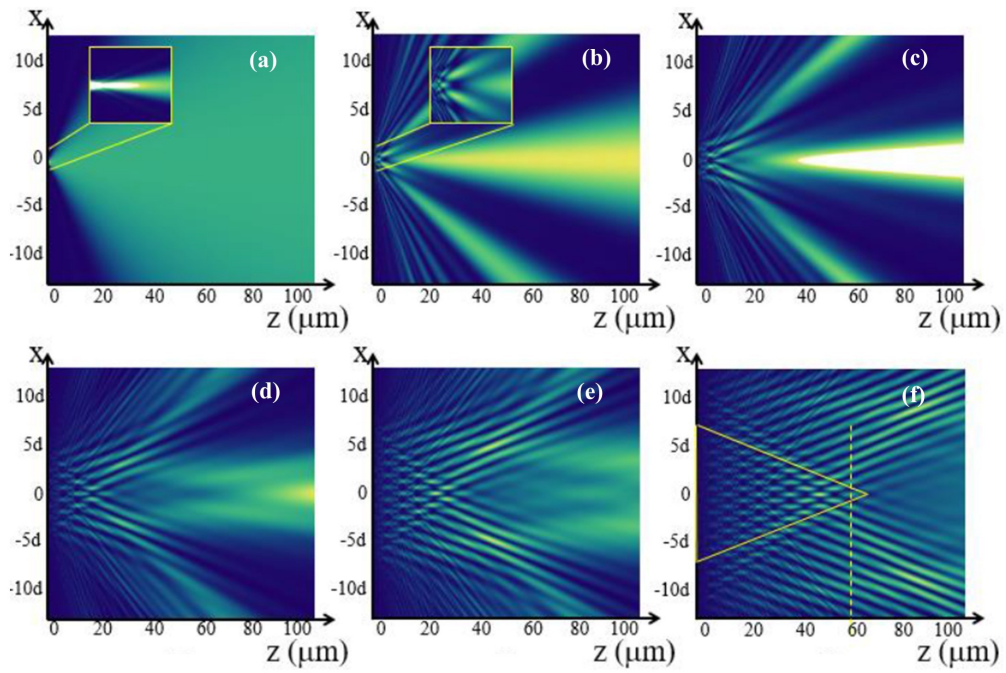


Fig. 3.17: Evolution of near field region with the number of slits, $N=(a)1$, $(b)2$, $(c)4$, $(d)8$, $(e)12$, $(f)20$. Zoom in near field regime is shown in insets (a) and (b) . The triangle area in (f) exhibits the internal area of the near-field interference pattern; the near field region is a few tens of talbot length. Taken from [112].

The above simulation was performed with cold Rubidium 85 (Rb) atoms [112] in single, double and multiple slit diffraction cases. However, a similar effect has been observed in the case of He atom diffraction, where the slits are the Gaussian functions (Fig.3.18).

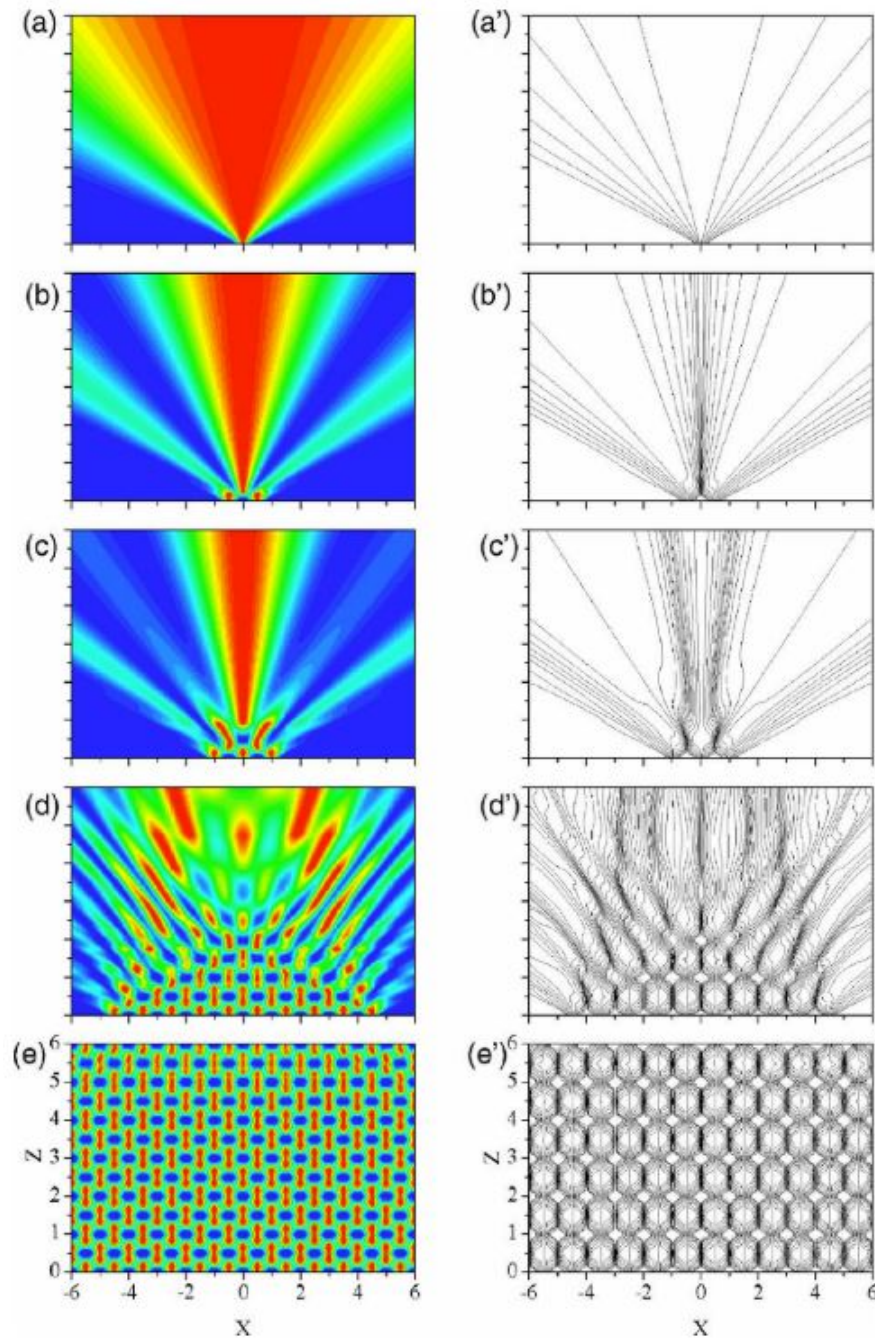


Fig. 3.18: Talbot carpet formation with different number of slits, (a) $N=1$, (b) $N=2$, (c) $N=3$, (d) $N=10$ and (e) $N=50$ are shown in left panel and right side are the quantum trajectories according to the left panels. X is the distance scaled in units of the grating period d , and z is in terms of Talbot length ($2L_T$). Taken from [113].

So, it is visible that this Talbot pattern exists over certain regions. After that, the pattern starts to blur, and the Bragg diffraction channel starts to appear [114].

3.3.1 Decoherence from near field region-Recoiling of Ar atoms

It is interesting to calculate the recoil energy of the Ar atoms after the impact with high-energy He atoms.

Now, the decoherence phenomenon can be understood in this way: after the interaction with Ar atoms,

due to the small angle deflection of the He atoms after the interaction with Ar gas, instead of following specific Bragg peaks, the He atoms collapse away from the Bragg peaks.

By considering He atom scattering from a LiF surface at 1 keV energy, the Bragg angle is $\theta_B = \tan^{-1}\left(\frac{G_y}{k}\right)$, where G_y and k are the reciprocal lattice vector and wave vector respectively. Along $\langle 100 \rangle$ direction of LiF, the reciprocal lattice vector is $G_y = \frac{2\pi}{2.01} \text{ \AA}^{-1} = 3.12 \text{ \AA}^{-1}$, the wavevector is $k = \frac{\sqrt{2mE}}{\hbar} \approx 1380 \text{ \AA}^{-1}$. So the Bragg angle is $\theta_B = 0.129^\circ = 2.2 \text{ mrad}$.

Now, if we consider that He atoms, after the interaction with Ar environment, collapse in between the Bragg peaks, i.e., on the half of Bragg angle $\frac{\theta_B}{2}$, then the energy of scattered He atoms will be 999.99 eV (from appendix B, equation B.4). The recoil energy of Ar atom is 0.01 eV = 10 meV. Although the recoil energy is small, it is possible to see decoherence. Alternatively, the wavelength associated with the recoil energy is less than the period of the crystal.

3.4 Discussions and conclusions

The present work represents a systematic study of decoherence due to collisions from surface adsorbates and in the gas phase. We restrict the discussion to matter-wave diffraction through a grating, material grating or a crystalline surface. Decoherence is supposed to result from the theoretical possibility, by interaction with the environment, to derive which path information. From our understanding, the latter should only be accessible in the near field region (NFR), where the position of the wave packets is unambiguously related to the path[113]. The extension of this NFR is typically a few units of the Talbot length and depends on the number of grating slits that have been illuminated by the incident probe, and therefore on its coherence length (section 3.3). This length L_{NFR} can typically be approximated by:

$$L_{NFR} \sim N_S \times \frac{d^2}{\lambda} \quad (3.10)$$

with N_S is the number of illuminated slits, d and λ are the grating period and the particle wavelength. In our case, the NFR is small, about a μm for 10 illuminated atomic rows. This is a very short distance compared to the travel distance (3 cm in the high-pressure zone) between the surface and the exit tube. Yet, decoherence could be observed if the probability associated to either of the two following processes is orders of magnitude larger than the elastic cross-section:

- [1] The collision-induced deflection exceeds a value comparable to the Bragg angle.
- [2] The momentum imparted to the recoiling target is large enough, i.e., the de Broglie wavelength of the recoiling target is of the same size or smaller than the grating period to localize the collision, even if the center of mass motion is not affected.

For the first case, such a deflection should originate from collisions at large impact parameters, so the

region of the attractive part of the He-Ar interaction potential. For comparison, in interferometric experiments involving fullerene collisions with N_2 , a scattering angle as small as $1 \mu\text{rad}$ was sufficient to reduce the fringe contrast. The long-range Casimir-Polder interaction, responsible for such small scattering angles, is characterized by a cross-section that is 100 times larger than the geometric cross section [115]. In our case, we expect this figure to be much lower since the minimum deflection angle required for blurring the diffraction pattern is of the order of 1 mrad.

For the second case, our configuration (light projectile on a heavy target) is unfavorable for a large momentum transfer to the target atom. Although the recoil energy of the Ar atom is lower than the thermal energy, the fact is that due to the small extension of the near field zone, the decoherence cross-section will be large.

Our strong argument for rejecting the near field zone as being at the origin of the observed decoherence is the data shown in Fig.3.14. According to the above formula, L_{NFR} increases with the number of illuminated ‘slits’ (atomic rows in our case), and therefore proportionally with the coherence width $L_c = \frac{\lambda}{\theta}$, and θ is the divergence angle. Since $L_{NFR}(90 \mu\text{m}) < L_{NFR}(60 \mu\text{m})$, (we could actually quantify N_s and therefore the ratio of $L_{NFR}(90 \mu\text{m}) / L_{NFR}(60 \mu\text{m})$ by measuring the size of the direct beam in both cases (which determines the divergence angle), we should be measuring larger decoherence for the $60 \mu\text{m}$ data, but we observe the reverse. We then conclude that the observed decoherence does not arise from collisions in the near field.

On the other hand, collisions in the far field may produce decoherence-like behavior (in fact, a classical effect) of the diffraction pattern from collisional events leading to small scattering. From the classical point of view, these events that occur at large impact parameters would produce a broadening of the diffraction peaks. Our data shows the reverse effect, a narrowing of the diffraction peaks.

In reference [116], the authors calculate the differential cross section of elastic scattering of non-relativistic electron wave packets from atoms as a function of the transverse size of the wave packet (i.e. the transverse coherence width). The results show that the differential cross section increases substantially, in relative values, at larger impact parameters for larger beams (smaller coherence width). They interpret these findings by the fact that as the transverse size of the wave packet decreases, the density of the particle current increases in the vicinity of the potential center and more particles are scattered at larger angles. This paper suggests that a filtering of the incident wave packets, according to their width, may occur by scattering of gas atoms: the small-sized packets (with smaller coherence width and, therefore, larger beam size) will have a larger probability of being deflected at larger angles.

At last, a form of decoherence can also arise from the differential dephasing experienced by different parts of a wave packet. Although this effect is not qualified as decoherence by Arndt et al. [117] since it does not imply entanglement with the environment, it affects a similar degradation of the diffraction

pattern, so in our case a decrease of the coherent fraction. If we consider the influence of the transverse coherence width, we should expect that such dephasing-induced decoherence would be stronger for larger wave packets. This is opposite to our observation that the 90 μm slits data show more pronounced decoherence than the 60 μm slits data. We can, therefore, exclude collision-induced dephasing for explaining our observations; in addition, this process cannot explain the diffraction peak narrowing.

We should finally comment on the fact that decoherence can be observed from both the near field [70](Talbot-Lau interferometer) and the far field (Mach-Zehnder interferometer)[100]. As shown by the latter authors, the amount of decoherence depends only on the distribution of momentum transfer between the wave packet and the environment particle, whatever the nature of the particle (photon, atom, molecule). Decoherence has been observed using electron matter waves due to the interaction with background gases[118]. However, in this case, the contrast remains the same up to $\sim 10^{-4}$ mbar H_2 pressure, but the intensity is lost significantly. The high-pressure regime ($>10^{-4}$ mbar) could not be studied due to the possible electric discharge on MCPs.

The decoherence experiments with HP-GIFAD show promising results. To understand and interpret more, further experiments need to be carried out with the different gas species, projectile energy, surfaces, and slit sizes.

Chapter 4

Compatibility of GIFAD with High Power Impulse Magnetron Sputtering(HiPIMS)

Overview

Thin films are the key elements of the recent progress in all technological aspects in the recent days. The properties of the thin layers are directly correlated with the growth mechanisms. Several deposition processes, like Physical Vapor Deposition (PVD) and Chemical Vapor Deposition (CVD), are used to grow thin layers. So, controlling the layers during the growth process is essential. Magnetron Sputtering (MS) is one of the most used methods based on PVD-based technology, widely used in academics, R&D, and industry to deposit thin films on a large scale. Several attempts have been made using Reflection High Energy Electron Diffraction (RHEED) to monitor the growth process in MS in real-time. The adaptation of RHEED with MS is still complex due to the interaction of electrons with the electromagnetic (EM) fields. Grazing Incidence Fast Atom Diffraction (GIFAD) has shown its capability to follow real-time growth monitoring in several deposition processes. The high-pressure version (HP-GIFAD) is perfectly suitable for MS due to its operational pressure and neutral projectile. In this chapter, the first steps towards the adaptation of MS (HiPIMS) and GIFAD have been described from scientific and technical points of view.

4.1 Introduction

4.1.1 An introduction of plasma

Plasma is considered a fourth state of matter due to its different properties than the solid, liquid, and gas phases. The term 'Plasma' was first pronounced by Czech physiologist **J.E. Purkinje** in the mid-19th century for a uniform blood fluid, later **Irving Langmuir** in 1928, during his work on mercury arc[119] also referred to this word to define 'viscosity' of the ions in the gas phase, similar to the blood fluid.

Hence, from that time, ‘Plasma’ has been used to indicate ionized gases (or vapors). Plasma contains ions, electrons, and neutral species due to the ionization of the gas. The density of electrons (n_e) inside the plasma is often called plasma density. The plasma obeys the quasi-neutrality principle, i.e., the electron and ion densities (n_i) are equivalent ($n_i \approx n_e$). By considering these parameters, the ionization degree (or fraction) is defined as

$$F_{density} = \frac{n_i}{n_i + n_n} \quad (4.1)$$

where n_n is the density of the neutral species in the volume.

The ions are significantly heavier than electrons. So, they behave differently and follow different distribution functions, which helps to get the estimation of the temperature of the plasma. Suppose T_i and T_e are the ions and electrons temperature; then hot (thermal) plasma is defined as $T_e \approx T_i$ and if $T_e \gg T_i$ is called cold or non-thermal plasma.

Also, from the ionization point of view, cold plasma is weakly ionized ($F_{density} < 0.1$) compared to hot plasma ($F_{density} \approx 1$). In this chapter, we will discuss about magnetron discharge where the electron density $n_e \approx 10^{16} - 10^{19} \text{ m}^{-3}$ and temperature (T_e) ranges from 1-5 eV.

To obtain the plasma, a significant amount of energy must be transferred to the gas, especially to the free electrons, which further ionize the gas. The free electrons mentioned here are caused by cosmic radiation or thermal energy. The easier way is the electrical discharge process. Here, the gas is usually ionized by applying an electric field (a voltage) between two electrodes, and the effect is an electric current passing through it. The free electrons can get the energy from the electric field and collide with neutral gas. Typically, at least three types of collisions are present: elastic-electron and gas particles do not exchange their state, but the energy is exchanged; excitation - where the gas particle passes in an excited state one of its electrons, but it still stays attached to the nucleus; and ionization - when a new electron is ejected from the atom and behind a positive ion is formed. Hence, the ionization processes produce the same amount of electrons and (positive) ions. This is the basic principle of glow discharge.

4.1.2 DC glow discharges

The most common type of discharge is Direct Current(DC) glow discharge, which is generated by applying a strong electric field between two electrodes (cathode and anode), where a gas is confined in a low-pressure chamber[120].

The term DC is used for the unidirectional flow of electric charged species, and the power supply can deliver only one type of polarity of voltage or current. The glow discharge has different regions, as shown in Fig.4.1.

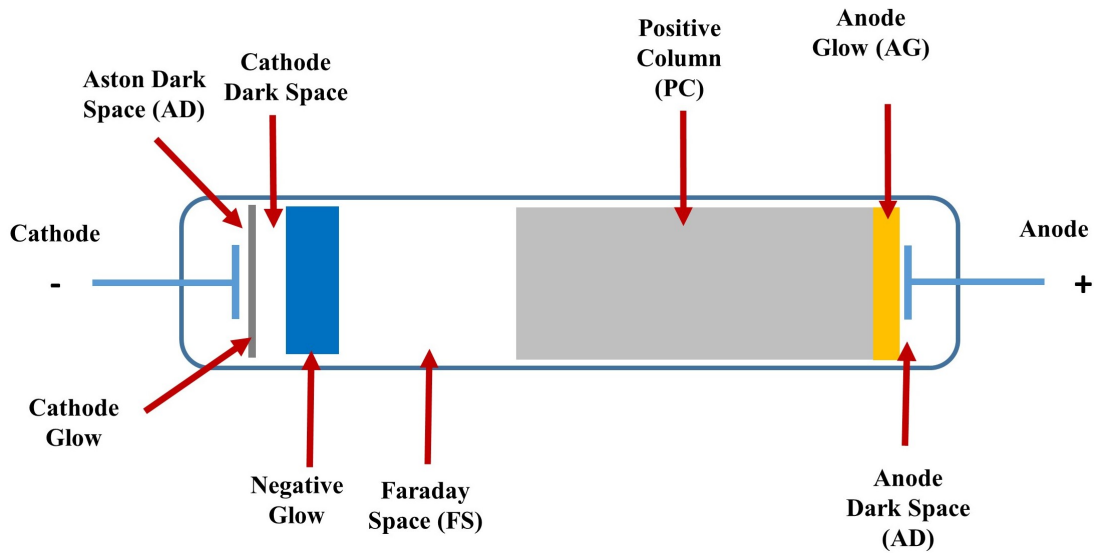


Fig. 4.1: Several regions in the DC glow discharge appears between cathode and anode.

The dark regions near the electrodes are more interesting and are known as ‘sheaths.’ Suppose 1kV is applied on the cathode (Fig.4.2), and the anode is considered as a ground. It has been observed that plasma does not follow a linear dependency of its potential between the electrodes. It is constant in the plasma volume and drops before the electrodes reach their respective potentials. This region has a strong electric field, and electron density is much lower than plasma.

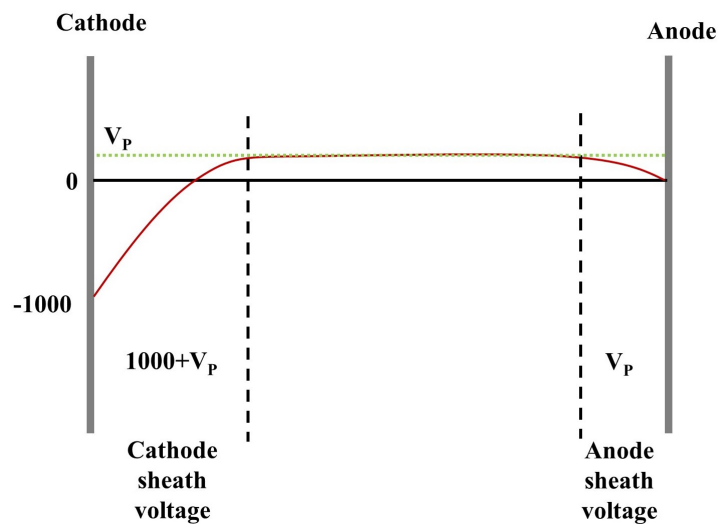


Fig. 4.2: Distribution of voltage in a DC glow discharge. In this hypothetical case, 1000V is applied on the cathode, and the anode is grounded. Here V_p is the plasma potential.

The most interesting region is the ‘Negative Glow’ region, where inelastic collisions(e.g., ionization, excitation, etc.) with gas atoms and electrons dominate.

The process starts with electron impact ionization. In this process, free electrons are accelerated due to the electric field and collide in their path with the gas molecules. Depending on the energy of the

electrons, different mechanisms take place. When considering the Ar environment, gas (Ar) ionization happens when the energy of the electron is 15.7 eV or higher (Fig.4.3-1).



The two electrons (equation 4.2) are accelerated further, and successive collisions produce a cascade effect that helps to maintain the discharge. The multiplication process of electrons in a glow discharge is known as an ‘electron avalanche.’

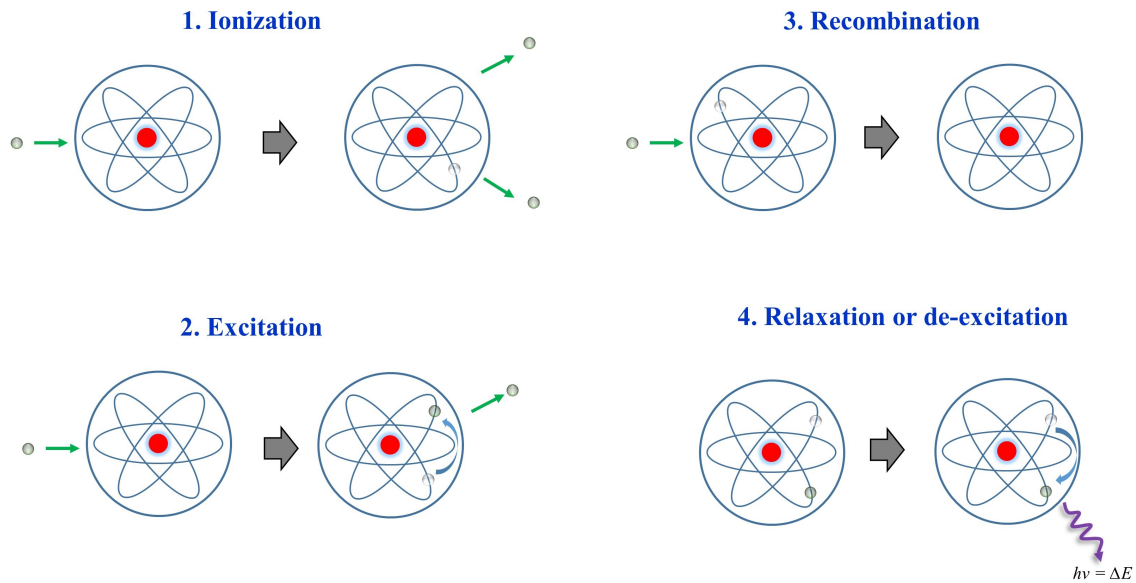


Fig. 4.3: Different inelastic processes are depicted here.

In the plasma, several other inelastic processes can occur. All the processes are summarized in Fig. 4.3. For instance, some electrons also recombine with ions and form again neutral atoms (molecules), which is a normal process in the existence of free ion-electron systems (Fig.4.3-3(Recombination)).

The kinetic energy of these accelerated electrons is sometimes less than the ionization energy; in this case, excitation happens according to equation 4.3.



The lowest excitation energy of Ar is 11.56 eV (Fig.4.3-2), lower than the ionization potential as the energy required to transfer the electron in higher energy levels, which are less tightly bound due to their larger distance from the nucleus. During excitation, the incident electrons transfer their energy (or a fraction of it) to the one bonded electron of the atoms and are deflected (conserving the total momentum of the system).

The name of this discharge process is glow discharge because it produces light. This glow is due to the relaxation or de-excitation of the electronically excited atoms and molecules, which is the inverse of the

excitation process. The electrons in the higher level soon come back to their ground state through one or multiple transitions due to the instability in higher levels. This transition corresponds to the emission of photons specific to the difference in energy levels (ΔE) (Fig.4.3-4). We can see this if the wavelength falls in the visible range (400-700 nm), the corresponding transitions from 3-1.7 eV, respectively.

4.1.3 Electrical breakdown

It's interesting to know how the working gas, which is basically a poor electrical conductor, can be transformed into a good electrical conductor, i.e., plasma.

The electrical breakdown starts with a small number of free electrons inside the chamber due to the background radiation (cosmic rays and other sources) or thermal energy. When a significant but limited potential difference is applied between the electrodes, the electrons can hardly ionize the gas medium through electron impact ionization, producing a weak current (Fig.4.4, A to B in the nA range).

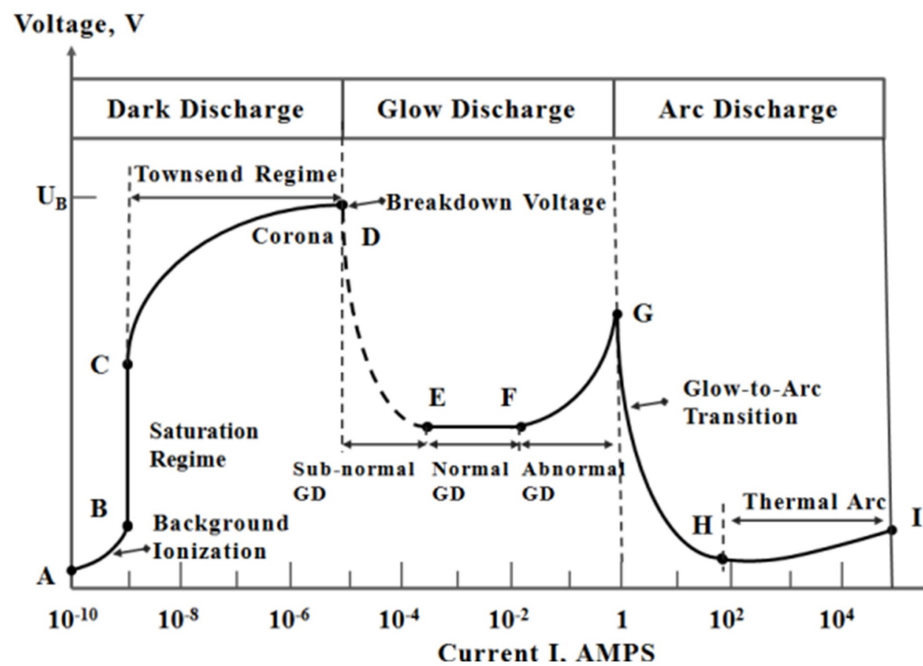


Fig. 4.4: Current-voltage characteristics of direct current (D.C.) electrical discharges. Taken from [121].

Further increase of the voltage does not affect the discharge current, and it saturates, as the number of density charge carriers remains small (from B to C). But the electrons will acquire enough energy if the voltage is increased further and produce new charge carriers by 'avalanche'. This is also called the 'ionization cascade'. This multiplicative process will generate an exponential growth of the discharge current (from C to D). However, the current remains small due to a small fraction of electrons and ionized species. This whole region from A to D is known as 'Dark discharge' as this type of discharge process is invisible to our eyes because very few excited states are produced. Notice that 'dark discharge' is not self-sustained, requiring an additional source of energy (electron photoemission, for instance).

If the voltage increases further, the cascade effect produces a large cloud of positive ions that will drift toward the cathode. The positive ions should liberate secondary electrons from the cathode which further produces an ionization avalanche, and the process can be self-reproduced since the avalanche produces a cloud of ions. It is said that the breakdown occurs, and the discharge switches in a self-sustained regime. This will produce a large current (point E), but the voltage level decreases to a few hundred volts (200-300 V), which depends on different parameters like type of gas, pressure, and the separation of electrodes. It is interesting to note that the breakdown voltage is much higher (see the transition from D to E), and it is Paschen's law according to equation 4.4.

$$U_B = \frac{Bpd}{\ln(Apd) - \ln[\ln(1 + \frac{1}{\gamma_{see}})]} \quad (4.4)$$

In this equation, A and B are the constants related to the gas that is used in discharge and can be found in the literature[122]. γ_{see} is the secondary electron emission coefficient.

The equation 4.4 is interesting as it shows that the same discharge voltage can be obtained by using high pressure (p) and small distance (d) or low pressure (p) and large distance (d). But the fact is that at low pressure, the ionization process is less effective due to the large mean free path of electrons, i.e., the probability of collisions of electrons with neutral is small. In this scenario, a high voltage must be applied to the target. But at high pressure, the mean free path of the electrons decreases, and due to many elastic collisions, the electron's energy decreases, which further reduces the probability of ionization, then higher U_B values are required. In conclusion, U_B increases as p increases. The product pd is known as the 'similarity parameter' of the glow discharges.

From E to F, the voltage is independent of the discharge current as more secondary electrons are emitted due to the ion bombardments. The region is called normal glow discharge region. The voltage is increased further due to the increase of current (from F to G), and the discharge enters into the abnormal regime. Most of the plasma processing is done here, like sputtering and plasma etching. The abnormal regime is more luminous than the normal discharge regime. It corresponds to high voltage-current operation, characterized by high plasma density. But the discharge is still in the glow regime.

With this process, the cathode becomes hot enough to emit thermo-electrons, and the voltage drops again. The discharge makes a transition into the arc regime. In the entire region (from G to I) the voltage drops being typically below 100V and high current discharge forms ($>10A/cm^2$). The high degree of ionization is used here to make cathodic arc deposition [123], a relatively new PVD technology to make films and coatings. However, the serious drawback of this technology (arc-PVD) is the production of droplets, which are not suitable for high-quality coatings.

4.1.4 Interactions of ions with surface

It is interesting to know what happens when the ion is approaching towards the cathode surface. There are different possibilities that can take place as discussed below.

1. Ion scattering: The ion can be reflected from the target and during this time, it can be neutralized in this process. This technique is widely used in surface science, known as Ion Scattering Spectroscopy. The energy of the ions is in the range between 0.5 to 10 keV. Depending on the range of energy, the technique has different abbreviations like LEIS (Low Energy Ion Scattering), MEIS (Medium Energy Ion Scattering), and HEIS (High Energy Ion Scattering).

2. Secondary electron emission: The impact of ions can liberate some electrons from the surface, known as secondary electron emission.

3. Ion implantation: The ion can penetrate inside the target and can be buried inside it. This is known as ion implantation. This technique is used in the surface treatment of steels or in microelectronics. However, the implantation is efficient for energies higher than 10 keV.

4. Ion assistance: The impact of ions can also do structural changes on the surface, called surface rearrangement. Thus, the rearrangement effect can change the stoichiometry in alloy or compound targets or can change the electron energy levels and distributions, this is basically known as radiation damage. When the energy of the ion is well-tuned, the process can be beneficial to the surface. During thin film deposition, the deposited particles obtained a substantial amount of kinetic energy due to energy transfer between the ion and adatoms, and this influenced the nucleation and growth process. This is known as Ion Beam Assisted Deposition (IBAD) or Ion Beam Induced Deposition (IBID). The typical ion energy lies between a few eV to a few tens of keV (generally 200 eV to 40 keV).

5. Sputtering: The ion impact can produce a series of collisions between the colliding atoms and the target atoms, which can help to eject the target atoms from the surface. This process is known as sputtering.

All of these possibilities (except radiation damage or re-arrangement of atoms) are shown in Fig. 4.5.

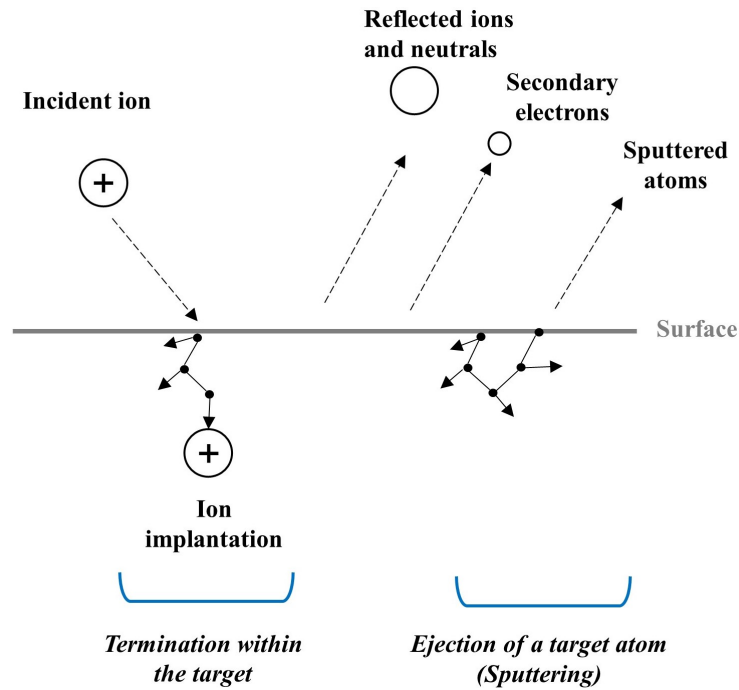


Fig. 4.5: Interactions of an ion with a surface.

4.1.5 The sputtering process

The sputtering is the mechanism of the ejection of the target atoms from the surface due to the cascade effect of collisions between the target ions and the surface atoms. The resulting momentum transfer is the cause of the emission of the surface atoms from the surface if the energy is sufficient to overcome the surface binding energy of the atoms.

Sputtering was first discovered by **W.R. Grove** [124] in 1852 when he was studying the electro-chemical polarity of gases. He named it a ‘dirt effect’ as the sputtered species deposited inside the discharge tube, which was undesirable.

In sputtering, mostly ions are used as they can be easily accelerated through the electric field. These ions can be neutralized easily as soon as it approaches the surface. The neutralization process depends on the projectile-surface system. Neutralization can be Auger neutralization, leading to the emission of one electron. It can be a resonant capture. So, the incident species are primarily energetic neutral.

The series of collisions on the surface produces a collisional cascade effect. This cascade effect can eject atoms from the surface, so at least two collisions are necessary. Otherwise, the energy is lost as heat.

The important parameter in sputtering is the sputtering yield (Y_S), which can be defined as the ratio of the number of atoms sputtered from the target to the number of incident atoms. In most cases, where the metal targets are used (such as Al, Cu, etc.) mostly Ar gas is used as sputtering gas. Generally, a high Y_S value [125] is desired for producing more sputtered species from the target. Sputter yield

is maximum when the incoming and the sputtered species have the same mass due to the maximum momentum transfer. The initial sputtering process is started with the Ar^+ , but after the sputtering of metal atoms (present in the plasma as a gaseous vapor metal species), they are ionized due to the collisions with the electrons. So, these metal ions can participate in the sputtering. Then, two ion species are generally sputtering the target depending on their sputter yield. When the sputter and incident species are the same, the phenomenon is called '*self-sputtering*.'

Today, 'sputtering' is widely used for different purposes like surface cleaning and etching [123] and mainly in PVD technology for the thin film growth processes [126]. When the thin layer is a compound, an option is to introduce a reactive gas (e.g., O_2 , N_2 , CH_4 , etc., often mixed with argon) leading to thin films of oxides, nitrides or carbides.

4.1.6 Magnetron Sputtering

In the DC sputtering process, the electrons are accelerated over the cathode sheath and make collisions with the sputter gas species. So, the path of the electrons is controlled by the electric fields only, and the collision frequency is controlled primarily by the pressure. In this process, high pressure is required to start the ionization process. During 1960 and 70, a magnetic trap was used, in front of the cathode, produced by the permanent magnets placed behind the cathode. This is based upon the concept of the work of Penning around 1930 where he demonstrated magnetically enhanced sputtering. The presence of a magnetic trap helps to ionize the gas and reduce the working pressure (< 4 Pa) and also the voltage applied on the cathode. The magnetron sputtering was introduced first by J.S. Chapin in 1974, which became one of the most important technology for thin film deposition nowadays [127].

The cross electromagnetic field near the cathode produces Hall drift of the electrons and electrons are trapped near the target. The velocity of the electron is

$$v_e = \frac{E \times B}{B^2} \quad (4.5)$$

Where E and B are the electric and magnetic fields. By this way the possibility of recombination of electrons is reduced as they are very far from the anode and chamber walls. This helps to remove cathode material in an efficient way and also to produce secondary electrons from the target even at low operational pressure (< 2 Pa), so that less amount of material is lost to the chamber walls. There are different types of magnetron.

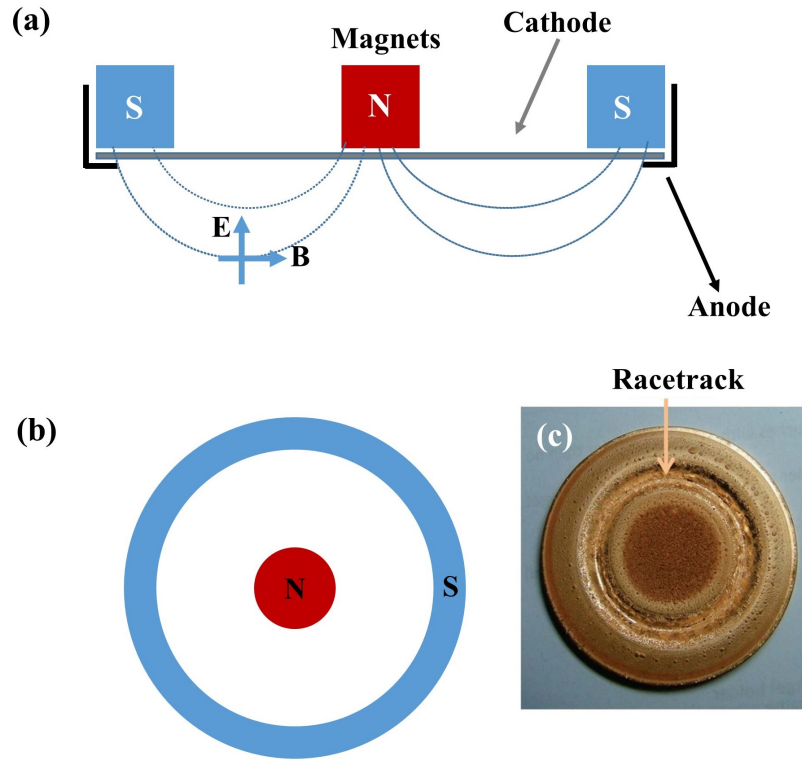


Fig. 4.6: Cross-sectional view of (a) planar circular magnetron and (b) top view with central and annular disc, (c) Cu sputtered target with a race track having heavy erosion. (c) is taken from [128].

In our work we have used a planar circular magnetron configuration, which is often used in thin film deposition in the laboratory. In the planar configuration, permanent magnets or electromagnets are used and placed behind the target. The schematic is shown in Fig. 4.6a-b.

For the planar magnetron, a torus-shaped plasma is observed near the target surface between the inner magnet and outer magnet ring. Thus, ionization probability in this region enhances the erosion of the target species and a race-track is formed. The fact is clear that during sputtering, a small percentage of the target is utilized ($\approx 25\%$) [2].

4.1.7 Direct Current Magnetron Sputtering (DCMS)

Direct Current Magnetron Sputtering is a technique to grow thin films where the target is kept at a negative electric potential between 300-700 V. Ar is used as a working gas in the pressure range of 0.1-1.5 Pa. The discharge current density is a few tens of mA/cm², and the power density is a few tens of W/cm².

In DCMS, the ionization fraction $F_{density}$ of the sputter species is very low, 0.1% or less [129]. The consequence of this is that the positive ions are mainly gaseous species and not the vapor originating from the target materials. In most cases, the sputter species are ionized due to the presence of metastable atoms in plasma (Ar^m), which is called Penning ionization [130]. The bombarding ions on the growing films are then Ar^+ .

The energy of the sputter species is a few eV (with a tail in the energy distribution lying to $\sim 10\text{-}50$ eV). The continuous sputtering in DC mode enhances the erosion of the target. In addition, the target does not get enough time to cool down. Therefore, a cooling system is necessary for this operation to avoid melting and destroying the target, but also especially to preserve the magnets behind the target.

As discussed above, the fraction of ionized sputter species is very low, so, to have some ion bombardment on the substrate, some ions can be guided towards the substrate by using a magnetically unbalanced magnetron. The unbalanced magnetron is a configuration where the outer magnet ring has different strength than the central one. So, the field lines extend towards the substrate, and the electrons can gyrate around those lines. The gyration of electrons helps to drag the ions in the plasma and both charged species are diffused towards the substrate due to the ‘ambipolar diffusion’. By applying a negative potential on the substrate, these ions can not only be attracted towards the substrate, but one can control their energy, and hence film growth conditions can be tuned.

Actually, by applying a negative potential, the ions gain some energy, and when it reaches to the substrate, it enhances the mobility on the surface. The fact is that higher energy of these ions can improve the quality, but at the same time, re-nucleation of the film starts due to sputtering. There are two types of Unbalanced Magnetron (UBM), type I and II. For type I, the residual induction of the central magnet is higher than that of the outer magnet. On the contrary, for type II, the residual induction of the central magnet is lower than the outer magnet. As shown in Fig.4.7-c, not all the field lines are closed between the central and outer magnets; some of them are directed toward the substrate. It has been proved that type II unbalanced magnetron can help to reach the ion current density up to 5 mA/cm^2 , an order of magnitude of conventional balanced magnetron [131].

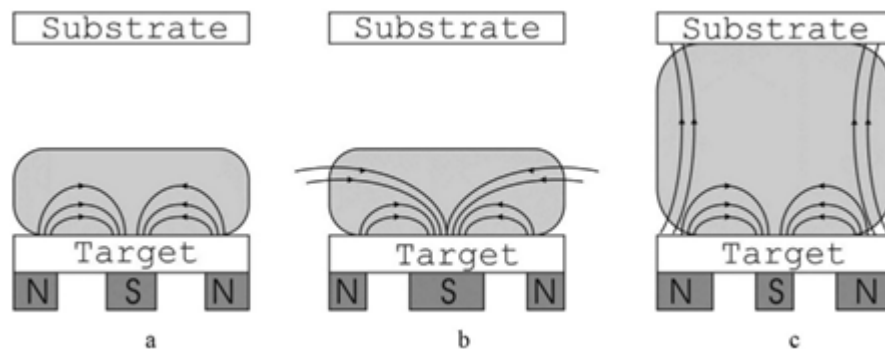


Fig. 4.7: Types of magnetron configurations, a- conventional balanced magnetron, b- unbalanced magnetron I, and c- unbalanced magnetron of the type II. Taken from [132].

4.1.8 High Power Impulse Magnetron Sputtering (HiPIMS)

High Power Impulse Magnetron Sputtering, known as HiPIMS is a variant of Magnetron Sputtering also called High Power Pulsed Magnetron Sputtering (HPPMS). It is a relatively new technology used in academic research and industrial applications. The basic development of HiPIMS started in Russia in

the early 1960s. But the technological advancement happened in the mid-1990s. There are several papers by Vladimir Kouznetsov et al. in 1999 are considered seminal papers on HiPIMS [133, 134, 135].

The basic idea was to increase the plasma density by applying high electrical power but within a limited time duration to avoid the transition to arc discharge. So, the electron density is in the order of 10^{19} - 10^{20} m^{-3} near the target surface. During the pulse, a very high electrical power is generated (approximately a few $\text{kW}\cdot\text{cm}^{-2}$) on the target. This situation is not favorable for running the sputtering process in continuous mode (DC) due to the overheating of the target, among others. The solution consists of applying power in short pulses with a relatively low-duty cycle (typically 1%). In this pulsed mode, the average power remains the same as in DC mode. However, the large power during the pulse enhances the production of metal vapor from the target by sputtering, and further, the ionization fraction of the sputter species and a dense plasma can be obtained.

The duty cycle is calculated by considering the ratio of the pulse duration and the total period of the pulses. The target cooling is related to the average power, not the peak power.

The difference between the DC mode and HiPIMS mode is listed in Table 4.1. The datasets have been taken from the references [134, 136].

Parameter	DCMS	HiPIMS
Target Voltage	300-700 V	500-2000 V
Duty Cycle	100 %	< 5 %
Current Density	up to 4-60 $\text{mA}\cdot\text{cm}^{-2}$	500-5000 $\text{mA}\cdot\text{cm}^{-2}$
Power Density	up to 0.05 $\text{kW}\cdot\text{cm}^{-2}$	0.5-10 $\text{kW}\cdot\text{cm}^{-2}$
Electron Density	10^{15} - 10^{17} m^{-3}	10^{18} - 10^{19} m^{-3}
Electron Temperature	1-5 eV	1-5 eV

Table 4.1: *Typical parameters during DCMS and HiPIMS discharges.*

The discharges in DC and HiPIMS modes are shown in Fig.4.8. The difference in color is due to the dominant excited species in the plasma. For the same metal target, the HiPIMS plasma is considered metal plasma as the metal fraction is much higher compared to the DC mode.

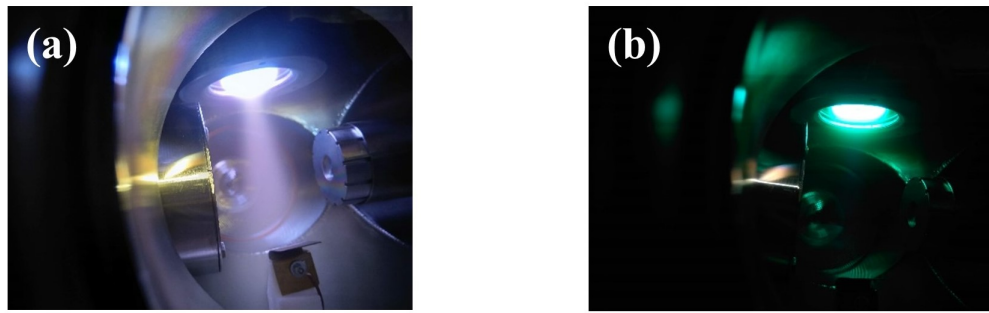


Fig. 4.8: (a) DC mode and (b) HiPIMS mode discharge. Both images were taken in ISMO magnetron reactor mounted on the high-pressure GIFAD chamber. A two-inch Cu target is used here.

The important fact is that the current-voltage characteristics is nonlinear (Fig.4.4). So, a small increase in voltage increases a large amount of current. To avoid any arc formation, the pulse is cut off after several tens of microseconds.

A typical current-voltage characteristic of HiPIMS is shown in Fig. 4.9. Here the pulse width is 20 μs and frequency 200 Hz. The peak voltage and peak current are 640 V and 18 A, respectively. It gives a peak power of 11.5 kW, which is very high in 20 μs duration of time.

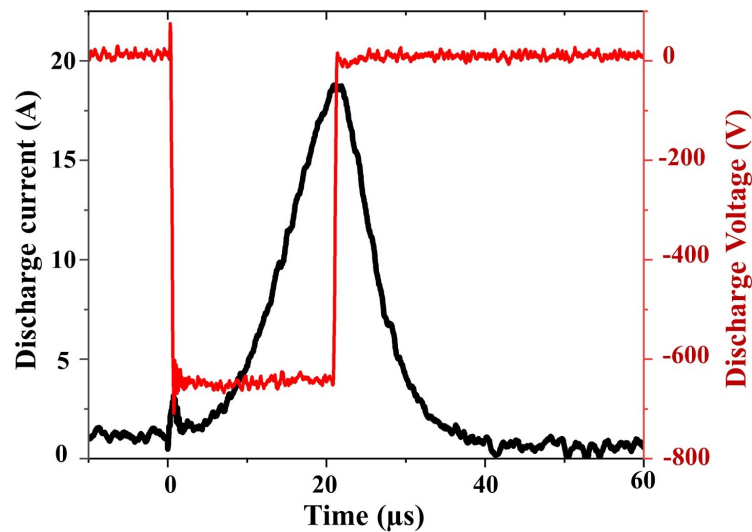


Fig. 4.9: Current-voltage characteristic during the discharge of HiPIMS, Pulse duration 20 μs and frequency 200 Hz. Here an one-inch Cu target is used.

In DCMS, the deposition is assisted with the ions coming from the gas, i.e. the Ar^+ ions, the number of ions of the sputtered species are practically negligible [137]. This is called ‘ion-assisted deposition’. The fundamental goal over the last few years is to increase the ionization fraction of the sputtered species, as the ion flux on the substrate significantly increases the quality of the film. Indeed, the metal ions not only assist the film, but they are part of the deposited material. Hence, in HiPIMS the precursors are energetic neutrals ($\sim \text{eV}$) as a result of the sputtering and very energetic ions (depending on the bias of the substrate, up to $\sim 100 \text{ eV}$). This process is known as IPVD (Ionized Physical Vapor Deposition).

This happens when the deposition flux consists of more ions than neutrals. HiPIMS is one of the IPVD techniques that is widely used to grow thin films with improved adhesion, improved microstructures, and improved coverage of complex-shaped substrate.

The deposition rate in HiPIMS discharge is lower than the conventional DC sputtering mode at the same average power. It has been observed that for Cu and Titanium the deposition rate is reduced to about 50 % compared to the DC mode.

The directionality of ionized sputtered species can be obtained by applying a bias potential on the substrate. This helps to grow a void free and a columnar grain extending from the bottom surface of the substrate, but also, in the case of deposition on 3D complex shaped parts.

It has been discussed that high-pressure GIFAD (HP-GIFAD) is well suited to follow the real-time growth monitoring in Magnetron Sputtering (MS). It has been proven that the quality of the film is much better in HiPIMS compare to the other MS depositions. This motivates to adapt HiPIMS with HP-GIFAD. The HP-GIFAD can give insights to control the film morphology by controlling the large number of growth parameters of HiPIMS.

The challenges of the first adaptation stage have been discussed vividly in the next sections.

4.2 Experimental results

4.2.1 Condition of GIFAD detector in the presence of plasma

In the GIFAD setup, the detector is composed of two Micro Channel Plate (MCP) and a phosphor screen. MCP is generally used to detect particles like electrons, neutrons, and photons (UV and X-rays). The discussion about the detector has been done in **Chapter 2** in an extensive way.

It has been observed that the detector is entirely blind in the presence of plasma, as shown in Fig.4.10 (a). Also, the high noise level is undesirable to prevent MCPs and screens from degradation.

Here the challenging issue is to understand the possible source of noise and eliminate it during the data acquisition. Several experiments have been performed to resolve the problem, and they are explained and analyzed in the next sections.

4.2.2 Possible source of noise on GIFAD detector

It is easy to predict that the possible source of noise could be the species that are present inside the plasma (electrons, ions, or neutrals).

To understand more about the different potential origins of the recorded noise, an electrostatic deflector was designed and placed in front of the detector, mounted on a ConFlat (CF) UHV 5-way cross, as shown in Fig.4.10-b.

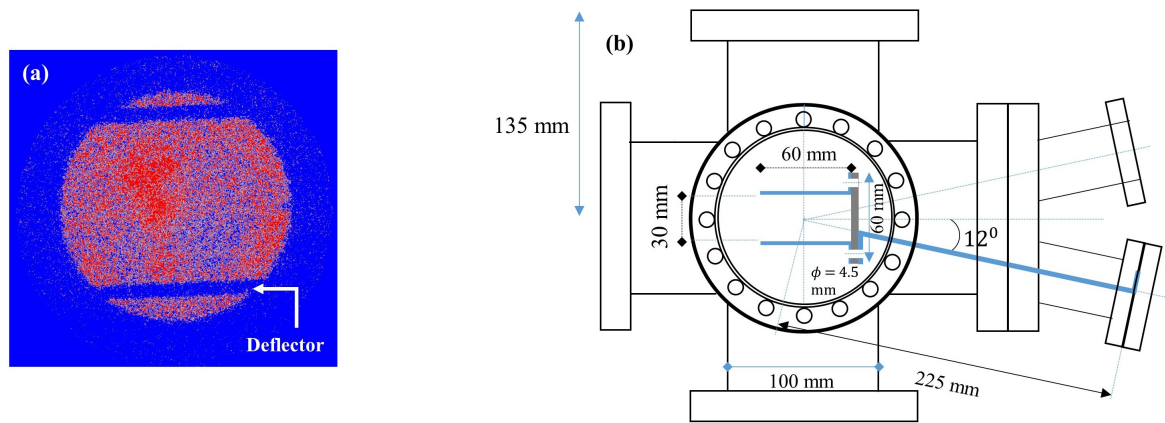


Fig. 4.10: (a) Noise on the detector in the presence of plasma and (b) schematic of the deflector system mounted on the ConFlat (CF) UHV 5-way cross.

The role of the deflector is to deflect the charge species by applying a few volts on the deflector plate. During this test, it was observed that the deflector bias has no influence on the noise, irrespective of its polarity. This confirms that the origin of the noise is not any charged species.

The other possibilities that remain are UV photons or neutral species. As it has been discussed that MCP is also sensitive to UV photons, so during the de-excitation process of the Ar^* , there is a possibility to emit photons (UV). There is an emission of UV/VUV photons having an energy between 3-12 eV [138] during the HiPIMS pulse.

To understand more, another simple experiment was performed. Basically, three different samples are put in front of the detector; one is a square piece of glass that can block the UVs and LiF, which has a large band gap (14.7 eV) [139] and a KCl having a band gap of 8.6 eV [140].

The three samples were attached to deflector plates as shown in Fig.4.11-a.

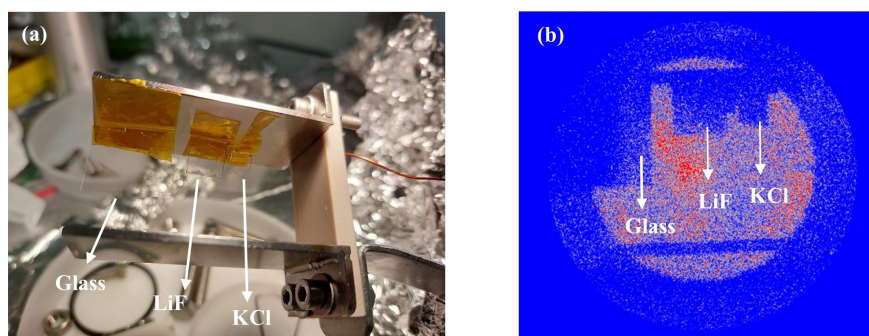


Fig. 4.11: (a) Three different samples attached on the deflector plate, (b) Noise on the detector.

The noise on the detector in the presence of plasma is shown in Fig.4.11-b. All of the three samples can cut off the noise on the detector. This experiment confirms that these species are not UV photons, as KCl and LiF block them. So, the possibility remains that the neutrals are present inside the plasma can produce noise on the detector.

To have a deep understanding, it is essential to know whether the noise appears during the pulse or in the off time, between the pulses (afterglow). Hence, the detector was pulsed according to the frequency of the HiPIMS pulse, and a delay was generated between the HiPIMS pulse and the detector ON time. So, the detector time-gate was opened after the pulse to avoid the noise i.e., in the afterglow period. The results due to the delay have been discussed extensively in the following section.

4.2.3 Effect of delay between detector ON time and HiPIMS pulse on noise

The time-gate of the detector (ON time) is adjusted at $300 \mu\text{s}$, and the delay between the pulse and detector is changed from $100 \mu\text{s}$ to 4.5 ms , as shown in the schematic of Fig.4.12.

The data has been taken for two different HiPIMS pulse widths, $40 \mu\text{s}$ and $50 \mu\text{s}$, maintaining the same peak power during the pulse. The results are shown in Fig.4.13.

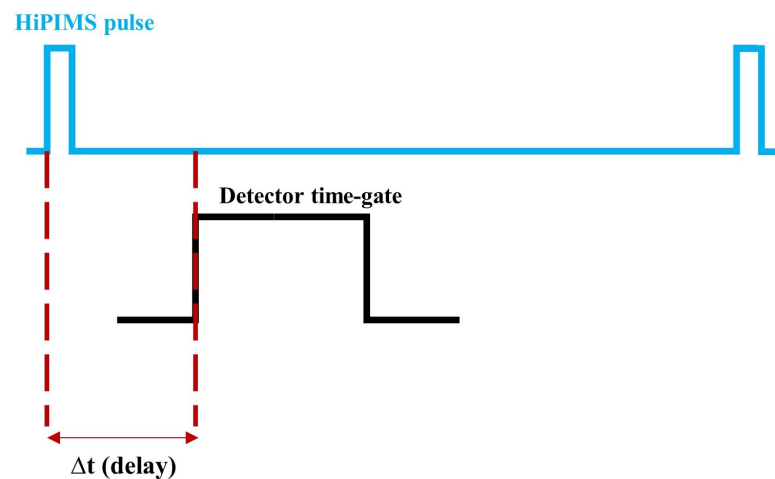


Fig. 4.12: Schematic of HiPIMS pulse and delay between the pulse and the detector time gate.

The interesting fact from Fig.4.13 is that with the time delay between HiPIMS pulse and time gate, the noise drops rapidly, but the noise presents a bounce starting from 1 ms and that reaches a maximum at 2 ms , then decays. As said, the experiment is performed with two different pulse widths, $40 \mu\text{s}$, and $50 \mu\text{s}$, respectively, having the same peak power in the pulses. It has been observed that for $40 \mu\text{s}$ pulse width, the maximum noise level at 2 ms is lower than the $50 \mu\text{s}$ HiPIMS pulse width. The low noise level at 2 ms for $40 \mu\text{s}$ pulse width is due to the low average power. During this experiment, the peak power was maintained almost at the same level in both cases (peak Voltage $\sim 660 \text{ V}$ and peak current $\sim 10 \text{ A}$). However, the average power was modified due to changes in the pulse width. The average power was modified from $\sim 26 \text{ W}$ to 33 W due to the change of pulse width from $40 \mu\text{s}$ to $50 \mu\text{s}$.

It is easy to get an idea about the energy of the neutral species from Fig.4.13. Suppose that the Ar neutrals are the cause of this noise, and they arrive on the detector at 2 ms . The distance from the main chamber to the detector is $\approx 1 \text{ m}$. So, these neutrals should be about 50 meV of energy if they are responsible for the noise. This kinetic energy is insufficient to allow them to emit electrons from MCP channels.

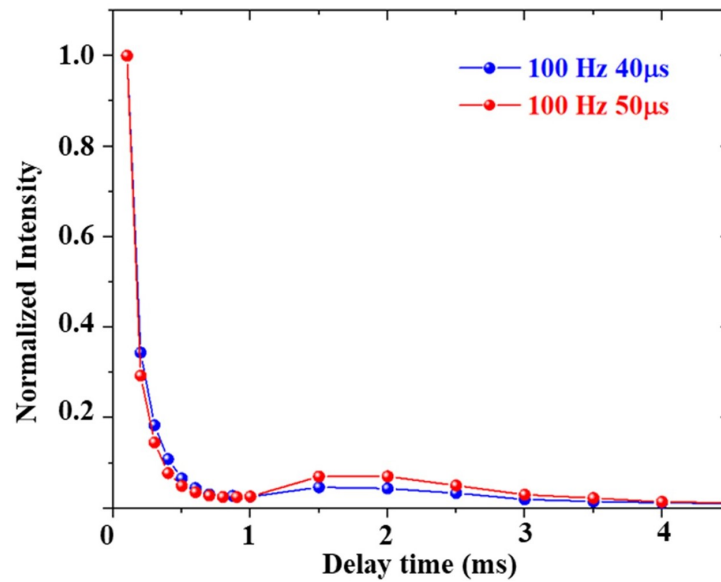


Fig. 4.13: Variation of noise with the delay between HiPIMS pulse and detector time-gate.

This observation can draw conclusions that some long-lived reactive species (i.e. having internal energy) from the plasma reach the detector between two pulses. The thing that remains for a noble gas like Ar is the metastable atoms (Ar^m), present inside the plasma and surviving a long time after the HiPIMS pulse is OFF, during the afterglow. This is the possible reason, even if the metastable atoms have low kinetic energy. Still, the internal energy is sufficient to emit electrons from MCP channels (without photon emission when they reach the detector plate) and start the electron multiplication process during the de-excitation process. Generally, Ar has two metastable states having the energy of 11.72 eV and 11.55 eV [141]. However, the metastable states can be quenched due to the collisions, or depending on the angle of collisions, it can get a directional velocity towards the detector. Also, there is a probability of ionization of Ar if the collision species are two Ar^m atoms (so called pooling ionization). But the latter situation is very rare, especially during the afterglow.

4.2.4 Direct beam condition

The ignition pressure for HiPIMS plasma is $\approx 10^{-2}$ mbar, which mainly depends on the frequency and the pulse width. It is observed that the discharge current is sensitive to the ignition pressure.

It has been observed that for 100 Hz and 20 μs pulse width, the ignition pressure is $\approx 2 \times 10^{-2}$ mbar. At this pressure, more than 80% of the intensity of the direct beam is lost due to collisions with the background gas.

After the ignition of plasma, there is an additional drop in beam intensity due to the interactions with the plasma species. The beam is $\approx 40\%$ reduced further (Fig.4.14-a). The direct beam intensity drops sufficiently, which alternatively reduces the scattered beam intensity. These conditions inevitably perturbed the suitable conditions to observe diffraction from the surface.

In order to keep the surface adsorbate-free over a long time and to have sufficient intensity of scattered beams, the ignition pressure must be reduced.

The idea is hidden in the early stage of the ignition process. We know that some free electrons are needed to start the ignition process (maybe from background radiation or other sources). Then cascade process takes time to ignite the ionization of the gas. The question can be asked, ‘What will happen if a sufficient amount of electrons are free inside the system from the early stage?’

This condition is suitable to ignite the plasma even at low pressure, as these electrons are trapped near the target due to the magnetic field.

A hot filament near the cathode is the ideal source to provide some extra electrons to the system. In the next stage, to ignite the plasma at lower pressure, we kept a tungsten (W) filament ON during the experiment. It has been observed that the discharge current is sensitive to the filament current.

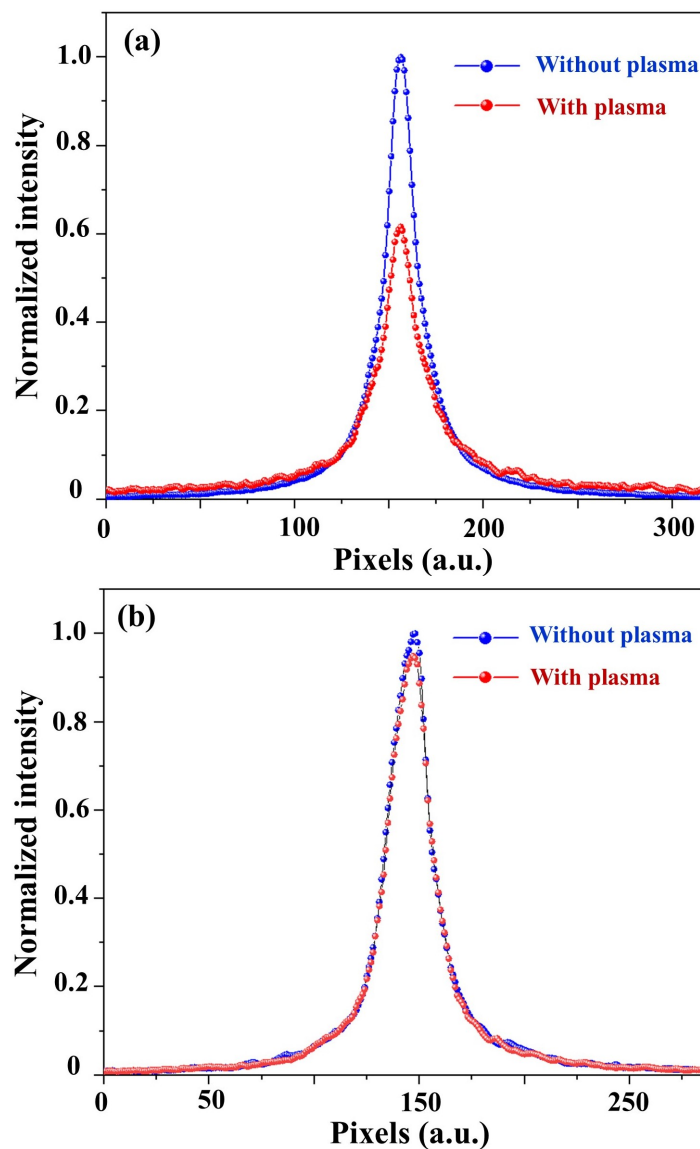


Fig. 4.14: Condition of the He atom beam with and without plasma, (a) without the filament the ignition pressure is 2.2×10^{-2} mbar and (b) with filament the pressure is 3.2×10^{-3} mbar.

Due to the low pressure, the plasma density is also low, which subsequently reduces the interaction of the incoming He atom beam with plasma particles, as shown in Fig.4.14-b. In this situation, the drop of the beam intensity is $\sim 4-5\%$ in the presence of plasma (Fig.4.14-b).

4.3 Conclusions and discussions

All these basic experiments help to find some suitable condition to progress toward the real-time growth monitoring. The conditions should be

1. The operational pressure must be lower than 10^{-2} mbar, to preserve the intensity of scattered beams and also to get rid of the contamination on the substrate.
2. Noise must be avoided during the acquisition of images. The possible way is to decrease the operational voltage on MCP, which also reduces the gain. Therefore, this can't be a suitable solution. However, it is possible to subtract the noise from the captured images but the long exposure damages the detector.

A suitable condition can be achieved by increasing the delay between the HiPIMS pulse and the detector time gate. From Fig. 4.13., it is observed that after 3 ms, the noise is sufficiently low on the detector. To have enough intensity of the scattered beam, the detector window must be enlarged. This can be done by decreasing the frequency of the pulse.

The filament is an 'extraordinary' idea to ignite plasma at a lower pressure (even < 0.2 Pa). At this stage, the filament is quite far from the target plane in the chamber. So, to ignite the plasma, sufficient power is cost (4 A, 20 V) by the filament. The long runtime of the filament also increases the temperature of the substrate, which has been observed during the experiment. The sample temperature is increased a few degrees. Also, a high current on the filament produces an arc inside the chamber (depending on the ground position). To avoid this, the filament must be kept near the target plane to trap the electrons easily and operate at a low current.

Also, from Fig.4.13, it is clear that the noise at 2 ms is lower for short pulses. So, the ideal condition would be (a) low frequency (≤ 100 Hz), (b) short pulses (20-30 μ s), and (c) low operational pressure to have enough intensity and low noise level on the detector.

A lower frequency and lower pulse width reduce the deposition rate. This will be interesting to see the effect of these above-mentioned deposition parameters on the film morphology.

Chapter 5

Ongoing work and future perspectives

Overview

The properties of a thin film of a given material depend on the thin film deposition parameters. It is always interesting to monitor and control the growth parameters in real-time, as they have a direct influence on material properties. To facilitate this endeavor, several *in-situ* techniques have evolved over the decade, as discussed in **Chapter-1**. Among them, GIFAD has shown its effectiveness in following the growth process in real-time in MBE deposition systems. In particular, we attempt to show with this thesis work that the HP-GIFAD system is ‘exceptionally’ suitable for monitoring the real-time growth in Magnetron Sputtering (MS). Here, the center of interest is the HiPIMS mode of deposition due to a large number of deposition parameters, and it typically yields a better quality film with a much higher deposition rate compared to MBE. In this chapter, the first experimental results of the deposition of metallic film (Cu) using HiPIMS on an insulator substrate (NaCl) are presented and discussed.

5.1 Introduction

Thin films have been an attractive field of research over a few decades due to their fundamental and technological aspects. It has been discussed already in **Chapter-1** about the Thin Film Photovoltaics (TFPV), anti-reflection coatings, etc. Besides this, thin films are widely used in medical applications.

Human beings are often encountered with microorganisms like viruses, bacteria, etc. For the last few years, studies have been going on in developing antimicrobial thin films. It has been seen that metallic nanoparticles have antibacterial properties like Ag or ZnO[142]. Due to the global spread of the Covid-19 pandemic in 2019, it was essential to develop vaccines and medicines. Also, during this time, the development of transparent antimicrobial film coating on the touch panel in the modern cash counter, mobile, and laptops had drawn attention. Among them, TiO₂ is one of the promising candidates as it has both photocatalytic and antibacterial properties[143].

There are several ways to grow thin films (Chapter 1). Among them, Magnetron Sputtering (MS) is a widely used method in industrial and academic research. Over the last two decades, the sputter deposition of thin films on large-area substrates has shown its unexceptional growth. Generally, sputtering is getting more and more attention in the present market and taking over the place of evaporation techniques. The reason is to be able to coat all kinds of materials, including high-melting temperature binary, ternary compounds, and multicomponent alloy systems. The good control of stoichiometry and the uniform thickness ($\Delta d < 2\%$) over a large area coating ($\sim 1 \text{ m}^2$)[144] makes it suitable to use in high-tech applications.

High Power Impulse Magnetron Sputtering (HiPIMS) is a cutting-edge technology, that is used to deposit better quality films (low roughness and highly adhesive). In today's world, industries are looking for an advanced coating technique to boost their product performance, and this is one of the reasons for using HiPIMS in the industry. It is really interesting to know that Apple is using HiPIMS to coat the iPhones. For an example, iPhone 12 Gold model is coated with HiPIMS, which makes it superglossy and wear-resistant. Also, HiPIMS is widely used in medical applications to coat orthopedic implant materials (CrN/NbN coating)[145].

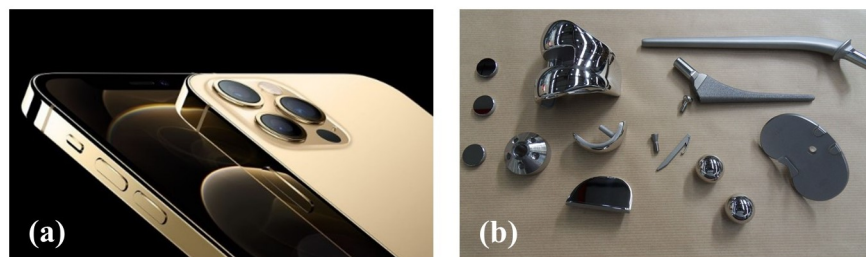


Fig. 5.1: (a) iPhone 12 gold coated with HiPIMS, (b) hip and knee replacement materials coated using HiPIMS deposition[Taken from Sheffield Hallam University webpage].

Deposition of metallic films has a considerable interest in the industry. Metals like Rh and Pd are involved in catalytic processes, Cu films are widely used in the glass industry for colored window planes, Cr coatings are corrosion resistant, etc. Many studies were carried out on the deposition of Cu films on air-cleaved NaCl (111) and (100) by evaporation method [146], and also by sputtering [147]. The epitaxial growth of Cu on NaCl (100) could be achieved by thermal evaporation at an oblique angle of incidence ($75^\circ \pm 5^\circ$)[148]. In the next section, we present the preliminary results of the deposition of Cu on NaCl(001) substrate is demonstrated with the preliminary results.

5.2 Experimental results and discussion

The first test was made on a NaCl(001) substrate cleaved in air. The HiPIMS pulse was set at $30 \mu\text{s}$ width and 100 Hz of frequency. The delay between the pulse and detector time gate was set at 2.4 ms as the

time period of the HiPIMS pulse is 10 ms. Due to the instabilities, the gate was opened slightly less than 7.6 ms, ~ 7.4 ms in every 10 ms. Diffraction from NaCl was observed along $\langle 110 \rangle$ direction, as shown below in Fig.5.2. The shutter was opened for ~ 8 minutes duration for the deposition. Here, a 1-inch Cu target is used as a cathode.

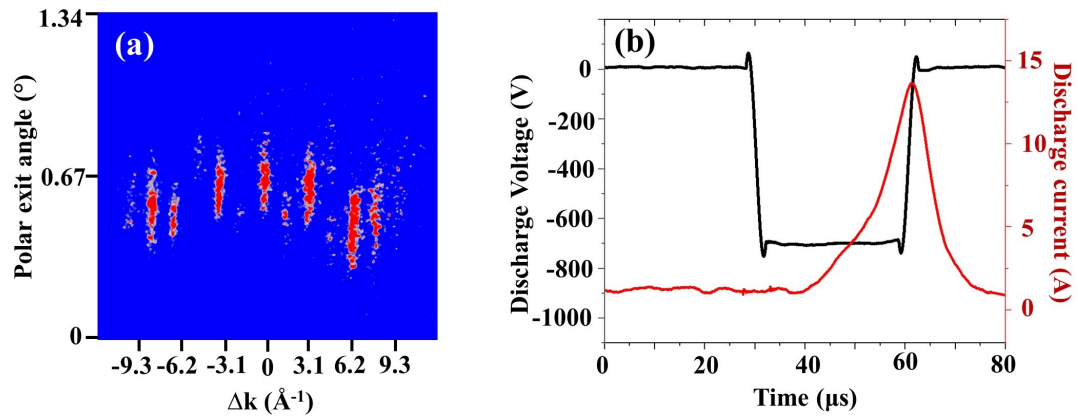


Fig. 5.2: (a) Diffraction of He atoms at 500 eV energy from NaCl(001) surface along $\langle 110 \rangle$ direction. (b) HiPIMS discharge voltage and current pulse waveforms for Cu deposition (700 V, pulse width 30 μ s).

It has already been explained in the previous chapter that using a hot filament, the ignition pressure can be lowered. Here, 4A filament current is used to ignite at 3.2×10^{-3} mbar of Ar pressure, which is 10 times lower than the pressure without filament. The discharge voltage is 700V, and the peak current ~ 13.5 A (Fig.5.2-b).

It has been discussed in **Chapter 2** (Fig.2.10) that a movable shutter is placed between the target and the substrate to control the deposition. We observed that the diffraction pattern from NaCl disappeared as soon as the shutter was opened between the target and substrate, and it was not recovered during the deposition. However, at the end of the deposition, mild annealing ($\sim 150^\circ\text{C}$) produces a nice specular diffraction spot at a relatively low (394 eV) beam energy, as shown in Fig. 5.3b-c.

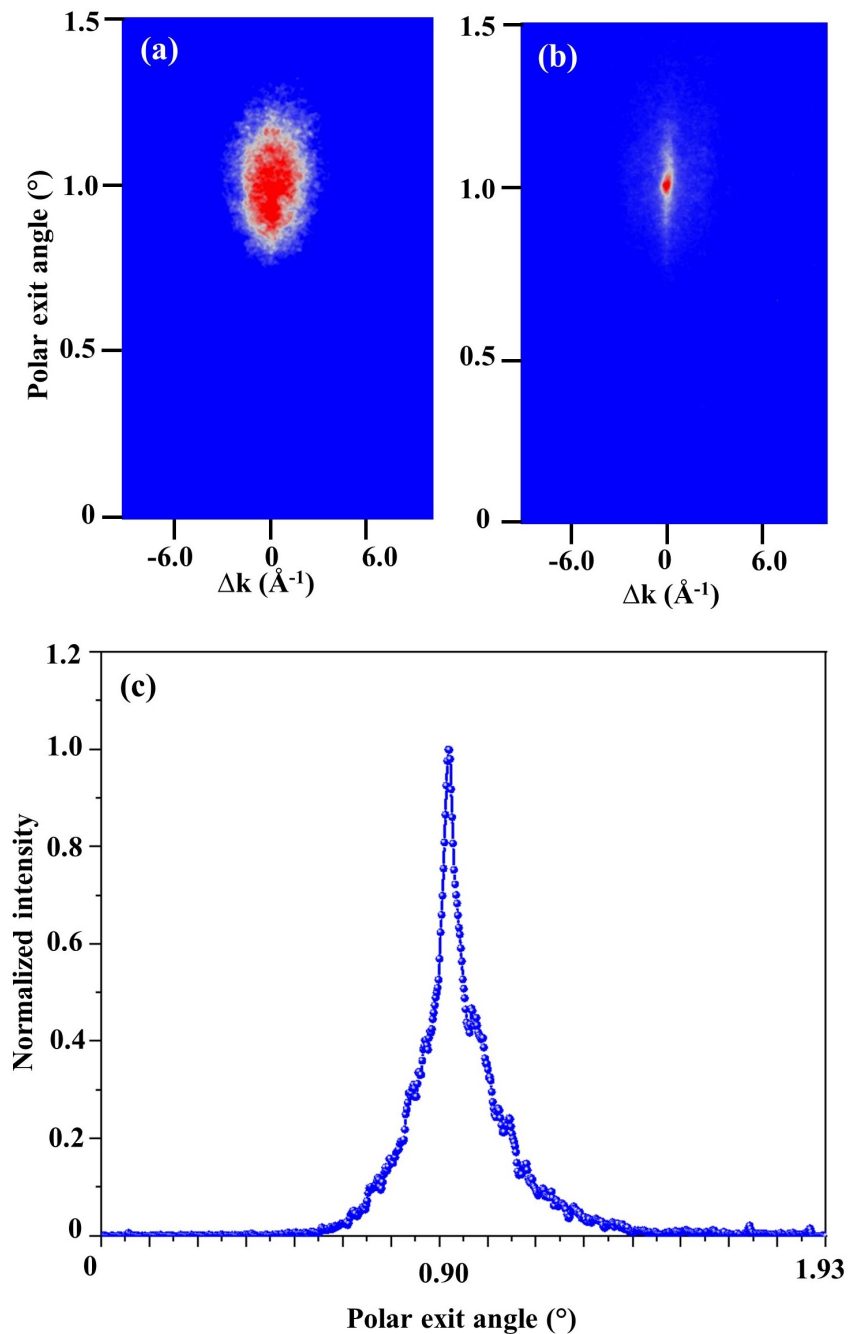


Fig. 5.3: (a) Intensity distribution observed after deposition and annealing at 150 °C at (a) 894 eV of energy and (b) at 394 eV of energy, (c) is the projection of (b) along the polar direction shows a sharp peak, considered as an elastic peak.

It is quite fascinating to see such a sharp (elastic) peak due to the scattering of He atoms from metal surfaces. At the lowest energy (394 eV), we clearly observe an elastic contribution to the intensity distribution. This elastic contribution is visible in the polar projection (Fig. 5.3-c) as a sharp peak on top of a log-normal distribution (see chapter polar profile fitting procedure in **Chapter 3**). This sharp peak is very rarely observed on metals and is a clear signature of a very good surface flatness. We conclude that the annealing of the deposited film produces a very smooth overlayer that wets the substrate. At energies higher than 394 eV, inelastic processes related to electronic excitations suppress the elastic peak.

The rapid loss of reflectivity opens up the possibility of island growth of Cu on NaCl from the initial stages. The He atoms are scattered from the islands at a large angle and go out of the specular cone, and intensity drops substantially on the detector. In order to slow down the deposition process, in the next experiments, the pulse width and frequency of pulse are further reduced, to have a large time period of HiPIMS pulse. A small pulse width reduces the deposition time, which is the favorable case here.

In the next experiment, deposition was performed with $20\ \mu\text{s}$ pulse length with a frequency of 50 Hz. The target and substrate were kept the same, and just the deposition parameters (pulse width, frequency, and average power) were changed. Here, the sample was aligned along the high-index direction to have enough intensity of the scattered beams. To ensure sufficient intensity of the scattered beams, 2 keV beam energy was used, and the detector gate width was set to 13.2 ms with a 3.2 ms delay with respect to the HiPIMS pulse.

The scattered beam intensity drops rapidly after opening the shutter, but as a difference from the previous experiments, post-deposition annealing did not help to get a smooth surface as no specular spot was observed. This implies that the growth process from the initial stage is island-type, which leads to a very rough surface. The reflectivity and the scattered beam intensity on the detector at different stages are shown below in Fig.5.4 and 5.5.

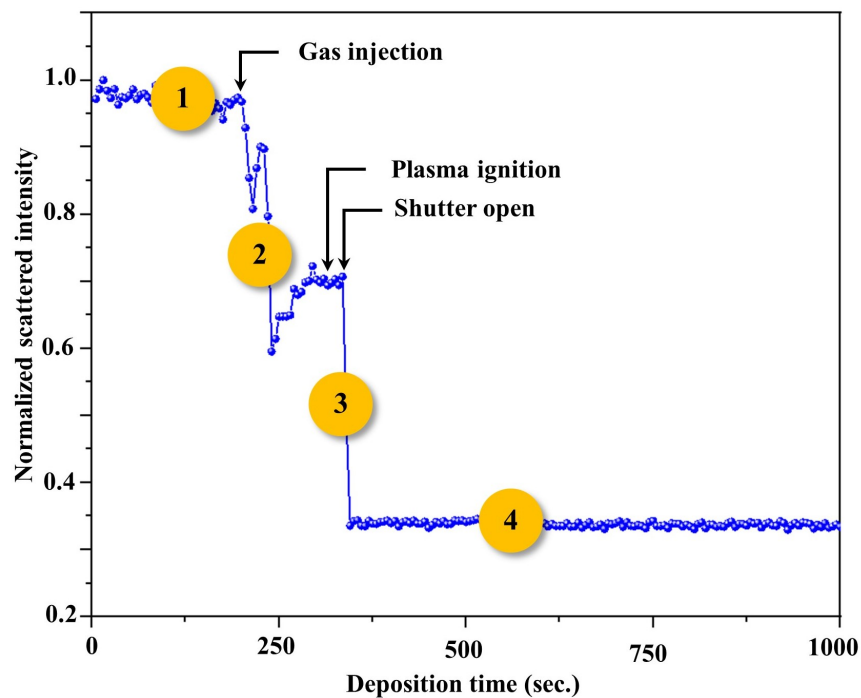


Fig. 5.4: Normalized scattered beam intensity over the deposition time of Cu.

Different regions are considered to understand in a better way. Region 1 is the initial stage, and 2 is the region where the Ar gas was inserted in the main chamber. After stabilizing the Ar pressure inside the chamber, the plasma was ignited. 3 is the region where the shutter was opened to start the deposition, and 4 is the region where the deposition process was continued. Although region-4 shows some intensity,

this is purely related to the noise on the detector.

The scattered beam signals are shown below in Fig.5.5.

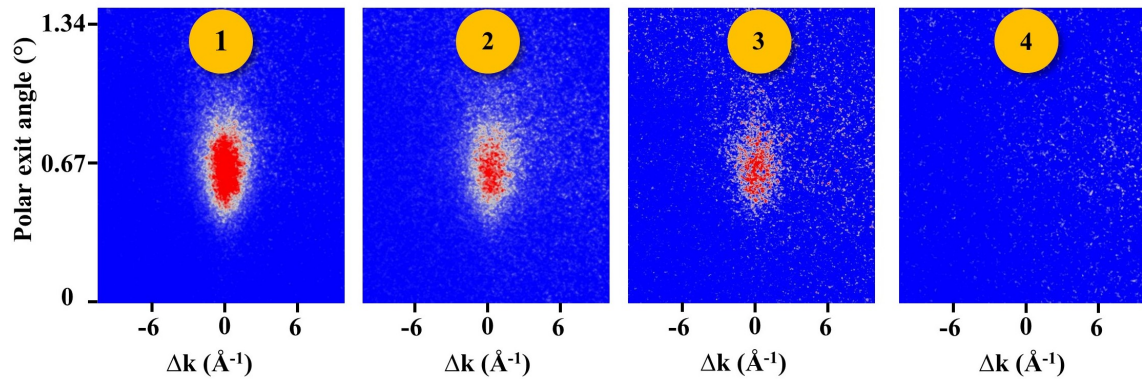


Fig. 5.5: Scattered beam intensity at different stages according to the reflectivity curve (Fig.5.4).

To shed light on the origin of the surface roughness, experiments with a Scanning Electron Microscope were performed at 5 keV of e^- energy. Islands are visible clearly in Fig.5.6. It shows the existence of a rough surface and explains well the disappearance of the scattered beam intensity.

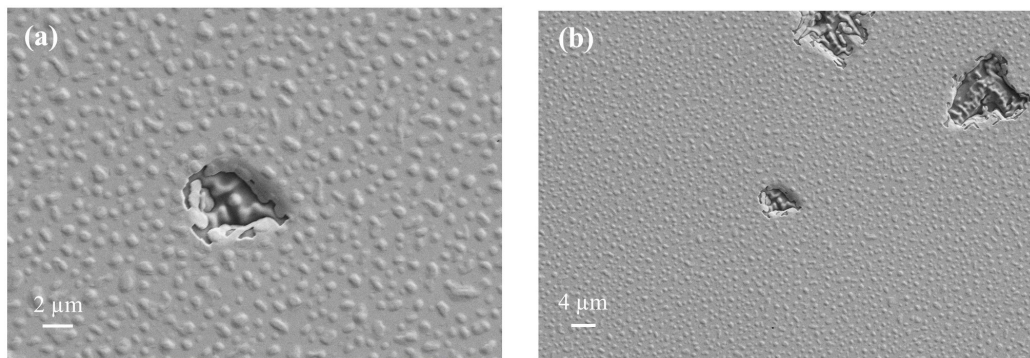


Fig. 5.6: (a) and (b) are the SEM images at two different magnifications. Magnification of (a) is \sim twice of (b).

5.3 Conclusions and perspectives

The first attempt to deposit Cu films on NaCl substrate shows promising results. The similarity in both cases (20 μ s and 30 μ s pulse widths) is the dealing with island growth instead of layer growth. Due to this, the He atoms scatter at a large angle from the islands, and reflectivity diminishes and disappears rapidly (Fig.5.4). In both cases we are completely unaware of the growth rate as the film thickness was not measured after the deposition.

An interesting issue that can be checked is the influence of substrate bias on growth. The previous experiments have been performed in a condition where the substrate was grounded. The bias voltage on the substrate can be helpful to provide additional mobility upon arrival on the substrate surface, which

can be helpful for having a better growth condition.

The other possibility could be an interrupted growth and check the substrate surface just after a single pulse. The other issue here is the reflected beam intensity on the detector. The beam intensity can be improved by the usage of a 'pulsed gas valve' synchronized with a HiPIMS pulse by injecting the gas over a time slightly greater than pulse width to ignite the plasma, and make it off during the pulse-off time. This reduces the He scattering from the background gas and is possible to have enough intensity on the detector.

The interesting finding is the elastic peak from the Cu surface. Generally, it is highly unexpected to have this from a metallic surface. This signifies the existence of a clean and flat region on the Cu surface, where He atoms don't undergo any energy loss during the interaction with Cu atoms. In the context of insulating materials, the band gap effectively inhibits any excitation process from the surface. However, in the case of metals, the overlapping nature of valence and conduction bands enhances the possibility of electronic excitation even in grazing conditions. If the first experiment is reproducible then it could provide a good method for producing extremely flat metal surfaces. To avoid mild annealing, performed after the growth, a bias voltage on the substrate, by providing additional surface mobility for the incident Cu ions. This can help to achieve flat film by making a layer-by-layer growth.

Another interesting future perspective could be the growth of functional oxide materials, such as TiO_2 and VO_2 , with a focus on epitaxial growth, strain-induced by lattice mismatch in real-time using GIFAD.

Chapter 6

Conclusions and perspectives

The work presented in this thesis primarily focuses on developing a new GIFAD system to make it compatible with Magnetron Sputtering (MS) deposition technique to follow thin film deposition in real-time. The entire work has been summarized into four main chapters.

The thesis started with a brief introduction chapter (Chapter 1), which can give insights into the importance of surfaces and interfaces, different thin film deposition methods, and the necessity of real-time monitoring of thin film growth.

The second chapter provides information about developing a new GIFAD setup (HP-GIFAD), different components, and the first experimental evidence of diffraction signal at high pressure, which validates the proof of concept of HP-GIFAD. We can get an idea about the scattering cross-section and mean-free path from the experimental results. We can understand the role of surface adsorbates in the scattered beam intensity decay, which contributes an additional contribution to the scattered beam intensity decay. Due to the scattering, the effect on the primary beam divergence is also observed in this study. The boundary between single and multiple collision regimes is also identified based on the collision frequency.

The High-pressure GIFAD can also serve as an ideal platform to study gas-surface interaction for poorly reactive systems. The high operational pressure is effectively suited for monitoring thin film growth in several deposition systems that work at high pressure, for example, PLD, CVD, and MS. Our center of interest is MS, which is described in the following chapters.

The third chapter addresses the fundamental issues related to wavepacket interaction with the surrounding gas (up to 10^{-2} mbar). This chapter explains the transition from quantum scattering from the surface toward classical scattering due to collisions with the injected gas. We have observed the loss of coherence, known as ‘quantum decoherence.’ In this study, we observed the decoherence due to collision with the Ar gas. We have introduced the concept of ‘near-field’ and ‘far-field’ diffraction, borrowed from wave optics to explain the origin of decoherence. We understand the effect of transverse coherence length (size

of wavepacket) on decoherence. Systematically, we have described the origin of decoherence, gas phase collisions, and the role of surface adsorbates. Alongside decoherence, we have discovered the anomalous behavior of diffraction peak width. The narrowing of diffraction peak width with gas pressure is highly unexpected and exciting. It can open novel scientific discussion. The experimental results are promising, and we have put forth several speculations to explain our experimental findings and one of them could be the ‘filtering process’ of wavepackets based on their transverse width.

The novel experimental results on decoherence motivate further to continue the experiment by changing several parameters (beam energy, different slits, etc.). We can also explore interaction potential by changing the diffraction probe or the gas target. The surface contamination and its influence on decoherence can be separated by building a localized gas cell near the surface. In this condition, the scattered beam interaction with gas can be localized. Also, by fine-tuning the position of the gas cell, we can choose a specific Bragg diffraction channel (specific Bragg peak).

The fourth chapter describes the basic concepts in plasma physics, ion-surface interaction, and different Magnetron Sputtering deposition methods. This chapter describes the challenges to adapting HP-GIFAD with MS. The fundamental problem we encountered in our case was the detector noise issue in the presence of plasma. In this chapter, we tried to understand the noise source by performing simple and interesting experiments. The experiment with the delay of the detector describes clearly that the metastable Ar is the cause of the noise. We have described the strategy to avoid this noise by maintaining the required delay between the HiPIMS pulse and the detector time-gate. At this stage, we are dealing with a substantial scattered beam intensity loss due to the high operational pressure (plasma ignition pressure). The usage of a hot ‘filament’ was an outstanding idea to ignite the plasma at ten times lower pressure. This helps to preserve the atom beam intensity to have a good diffraction signal from surface.

In this chapter, we identified the suitable conditions to follow the real-time growth of thin films using MS and HP-GIFAD. A low operational pressure, frequency, and pulse width could be adequate to proceed further.

Chapter 5 shows the first experimental result of real-time growth monitoring of Cu film on NaCl substrate. In this chapter, two experiments are described, and both of them show the 3D growth of thin layers from the initial stage. These studies found that high average power is suitable for having a flat metallic film in addition to post-deposition annealing.

These experiments further motivate us to find suitable conditions for having layer-by-layer or 2D growth. The role of surface bias during deposition could be effective in providing additional mobility of the adatoms after reaching the substrate surface. This can be beneficial in having layer growth instead of 3D island growth. After achieving layer-by-layer growth conditions, the experiment could be extended toward the reactive sputtering. The growth of VO_2 or TiO_2 with high crystalline quality will be a fasci-

nating future perspective. The beam intensity can be further improved by introducing a pulse gas valve, synchronized with HiPIMS pulse. In this scenario, the sputtered gas can be injected over a time slightly greater than the HiPIMS pulse. We already have seen that noise on the detector is unavoidable in DC conditions. So, we are limited only to HiPIMS deposition mode. However, we can try to quench the Ar metastable before reaching the detector. In this case, we can use a laser to excite the metastable species, and by deexcitation, we can prevent them from creating noise on the detector by the Penning mechanism. This can open the pathway to adapt HP-GIFAD with all MS deposition methods.

Appendix A

Comparison between LEED, RHEED, TEAS, GIFAD: wavelength, energy, incidence angle

Low Energy Electron Diffraction (LEED), Reflection High Energy Electron Diffraction (RHEED), Thermal Energy Atom Scattering (TEAS), and Grazing Incidence Fast Atom Diffraction (GIFAD) are considered sensitive techniques. In GIFAD and TEAS the projectile is neutral, which is scattered from the surface.

It is always important to have a brief knowledge of the techniques in terms of energy and incidence angle. In the table, a comparison is given.

	<i>Probe</i>	<i>E</i> (eV)	θ_{inc}°	<i>E</i> _⊥ (meV)	λ_{\perp} (Å)
LEED	e^{-}	30-200	90	$\sim 10^4$ - 10^5	~ 1
RHEED	e^{-}	$\sim 10^3$ - 10^4	< 5	10^3 - 10^5	0.5-10
TEAS	He	10^{-3} - 10^{-1}	5-90 (with respect to surface)	1-100	0.5-5
GIFAD	He	200-5000	< 2	1-1000	0.1-5

Table A.1: Comparison table of LEED, RHEED, TEAS and GIFAD. Taken from [71]

Appendix B

Binary elastic collision

A binary or two-body collision approximation (BCA) is mostly used to describe the ion scattering phenomenon from a surface. Depending on the energy of the projectile, the technique can be called Low Energy Ion Scattering (LEIS) or Medium Energy Ion Scattering (MEIS).

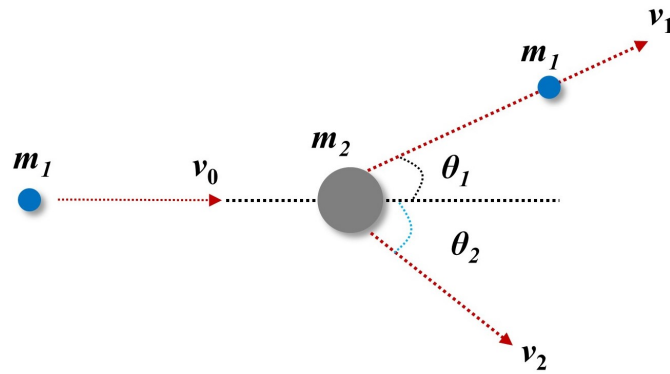


Fig. B.1: Schematic of a binary collision. The blue dot is the projectile, and gray dot is the target atom.

In binary collisions, it is considered that the impact of the projectile is only on one single atom, which is stationary. By considering energy and momentum conservation, the collision mechanism is considered an elastic process.

By considering the mass of projectile m_1 which is moving with a velocity v_0 hits the stationary target of mass m_2 . The initial kinetic energy of the projectile is given as $E_0 = \frac{1}{2}m_1v_0^2$. The energies of the particles after the collision are $E_1 = \frac{1}{2}m_1v_1^2$ and $E_2 = \frac{1}{2}m_2v_2^2$, where v_1 and v_2 are the final velocities of the projectile and the target particle.

By considering the conservation of energy

$$\frac{1}{2}m_1v_0^2 = \frac{1}{2}m_1v_1^2 + \frac{1}{2}m_2v_2^2 \quad (\text{B.1})$$

From the conservation of momentum, one can write

$$m_1 v_0 = m_1 v_1 \cos \theta_1 + m_2 v_2 \cos \theta_2 \quad (\text{B.2})$$

$$0 = m_1 v_1 \sin \theta_1 + m_2 v_2 \sin \theta_2 \quad (\text{B.3})$$

By solving these equations, one can get the expression of the energy of the scattered projectile

$$E_1 = E_0 \left(\frac{\cos \theta_1 \pm \sqrt{(m_2/m_1)^2 - \sin^2 \theta_1}}{1 + m_2/m_1} \right) \quad (\text{B.4})$$

Here θ_1 is the angle between the incoming and ongoing trajectories of the projectile, also known as scattering angle.

So, the recoil energy of the target is

$$E_2 = E_0 - E_1 = E_0 \left(1 - \frac{\cos \theta_1 \pm \sqrt{(m_2/m_1)^2 - \sin^2 \theta_1}}{1 + m_2/m_1} \right) \quad (\text{B.5})$$

Appendix C

Density matrix

The most general representation of a quantum system can be written in terms of ‘density matrix’ representation (ρ). It is also an operator called a ‘density operator.’ It has been constructed in such a way that it contains the classical and quantum probabilities. This is often used to understand the entanglement between two sub-systems.

Suppose there are two quantum states $|\psi_1\rangle$ and $|\psi_2\rangle$ having probabilities p_1 and p_2 . If A is observable, then expectation value of A will be

$$\langle A \rangle = \sum_i p_i \langle \psi_i | A | \psi_i \rangle \quad (\text{C.1})$$

now we can write $\langle \psi_i | A | \psi_i \rangle = \text{tr} [A | \psi_i \rangle \langle \psi_i |]$ Now, equation C.1 can be written as

$$\langle A \rangle = \text{tr} [A \sum_i p_i | \psi_i \rangle \langle \psi_i |] \quad (\text{C.2})$$

The density matrix is defined as

$$\rho = \sum_i p_i | \psi_i \rangle \langle \psi_i | \quad (\text{C.3})$$

The density matrix of a system is produced by the superposition of two states $|0\rangle$ and $|1\rangle$. For pure state ψ , it can be written as $|\psi\rangle = a |0\rangle + b |1\rangle$; in this case the density matrix can be written as

$$\rho = |\psi\rangle \langle \psi| = \begin{pmatrix} |a|^2 & ab^* \\ a^*b & |b|^2 \end{pmatrix} \quad (\text{C.4})$$

The existence of off-diagonal elements defines a certain amount of coherence of the states. Due to the interaction of the system with its environment, the off-diagonal elements slowly die out with time, and the system makes a transition from quantum to classical. This is the basis of ‘quantum decoherence’.

References

- [1] C. B. Duke. The birth and evolution of surface science: Child of the union of science and technology. *Proceedings of the National Academy of Sciences of the United States of America*, 100(7):3858–3864, 2003.
- [2] J. E. Greene. Review article: Tracing the recorded history of thin-film sputter deposition: From the 1800s to 2017. *Journal of Vacuum Science Technology A: Vacuum, Surfaces, and Films*, 35:05C204, 2017.
- [3] Tai Chang Chiang. Superconductivity in thin films. *Science*, 306(5703):1900–1901, 2004.
- [4] Hans J. Recent advances in the recording physics of thin-film media. 32:R147–R168, 1999.
- [5] Changhyun Ko and Shriram Ramanathan. Observation of electric field-assisted phase transition in thin film vanadium oxide in a metal-oxide-semiconductor device geometry. *Applied Physics Letters*, 93(25):252101, 2008.
- [6] Hemant Kumar Raut, V. Anand Ganesh, A. Sreekumaran Nair, and Seeram Ramakrishna. Anti-reflective coatings: A critical, in-depth review. *Energy and Environmental Science*, 4(10):3779–3804, 2011.
- [7] Anas Ghailane, Mohammed Makha, Hicham Larhlimi, and Jones Alami. Design of hard coatings deposited by HiPIMS and dcMS. *Materials Letters*, 280:128540, 2020.
- [8] S. K. Deb. Thin-film solar cells: an overview. *Renewable energy*, 8:375–379, 1996.
- [9] N. J. Dudney and B. J. Neudecker. Solid state thin-film lithium battery systems. *Current Opinion in Solid State and Materials Science*, 4(5):479–482, 1999.
- [10] Guoyu Ding, Yifan Zheng, Xun Xiao, Huiyuan Cheng, Guodong Zhang, Yifeng Shi, and Yuchuan Shao. Sustainable development of perovskite solar cells: keeping a balance between toxicity and efficiency. *Journal of Materials Chemistry A*, 10:8159–8171, 2022.
- [11] John R. Arthur. Molecular beam epitaxy of compound semiconductors. *Surface Science*, 299-300(C):818–823, 1994.

- [12] Maria Mateev, Thomas Lautenschläger, Daniel Spemann, Annemarie Finzel, Jürgen W. Gerlach, Frank Frost, and Carsten Bundesmann. Systematic investigation of the reactive ion beam sputter deposition process of SiO₂. *European Physical Journal B*, 91(2):1–8, 2018.
- [13] R. P. Netterfield, P. J. Martin, C. G. Pacey, and W. G. Sainty. Ion-assisted deposition of mixed TiO₂ - SiO₂ films. 1809:1805–1809, 1989.
- [14] František Lofaj, Lenka Kvetková, Petra Hviščová, Maroš Gregor, and Milan Ferdinandy. Reactive processes in the high target utilization sputtering (HiTUS) W-C based coatings. *Journal of the European Ceramic Society*, 36(12):3029–3040, 2016.
- [15] André Anders. A review comparing cathodic arcs and high power impulse magnetron sputtering (HiPIMS). *Surface and Coatings Technology*, 257:308–325, 2014.
- [16] James A. Greer. History and current status of commercial pulsed laser deposition equipment. *Journal of Physics D: Applied Physics*, 47(3), 2014.
- [17] J. A. Greer. High quality YBCO films grown over large areas by pulsed laser deposition. *Journal of Vacuum Science Technology A: Vacuum, Surfaces, and Films*, 10:1821–1826, 1992.
- [18] Hirofumi Takikawa. Review of cathodic arc deposition for preparing droplet-free thin films. *Proceedings - International Symposium on Discharges and Electrical Insulation in Vacuum, ISDEIV*, 2(4):525–530, 2006.
- [19] Eva Pellicer, Aida Varea, Salvador Pané, Bradley J. Nelson, Enric Menéndez, Marta Estrader, Santiago Suriñach, Maria Dolors Baró, Josep Nogués, and Jordi Sort. 983-991 Nanocrystalline electroplated Cu-Ni: Metallic thin films with enhanced mechanical properties and tunable magnetic behavior. *Advanced Functional Materials*, 20(6):983–991, 2010.
- [20] Xingyan Xu, Changrong Xia, Shouguo Huang, and Dingkun Peng. YSZ thin films deposited by spin-coating for IT-SOFCs. *Ceramics International*, 31(8):1061–1064, 2005.
- [21] R. S. Sonawane, B. B. Kale, and M. K. Dongare. Preparation and photo-catalytic activity of Fe-TiO₂ thin films prepared by sol-gel dip coating. *Materials Chemistry and Physics*, 85(1):52–57, 2004.
- [22] Luzhao Sun, Guowen Yuan, Libo Gao, Jieun Yang, Manish Chhowalla, Meysam Heydari Gharahcheshmeh, Karen K. Gleason, Yong Seok Choi, Byung Hee Hong, and Zhongfan Liu. Chemical vapour deposition. *Nature Reviews Methods Primers*, 1(1), 2021.
- [23] R. S. Balmer, J. R. Brandon, S. L. Clewes, H. K. Dhillon, J. M. Dodson, I. Friel, P. N. Inglis, T. D. Madgwick, M. L. Markham, T. P. Mollart, N. Perkins, G. A. Scarsbrook, D. J. Twitchen, A. J.

- Whitehead, J. J. Wilman, and S. M. Woollard. Chemical vapour deposition synthetic diamond: Materials, technology and applications. *Journal of Physics Condensed Matter*, 21(36), 2009.
- [24] D.J. O’Conor, B.A. Sexton, and R. St. C. Smart. *Surface Analysis Methods in Materials Science*. ISBN = 9783642074585, Springer-Verlag Berlin Heidelberg GmbH.
- [25] P. Rousseau, H. Khemliche, A. G. Borisov, and P. Roncin. Quantum Scattering of Fast Atoms and Molecules on Surfaces. *Physical Review Letters*, 98(1):016104, jan 2007.
- [26] A. Schüller, D. Blauth, J. Seifert, M. Busch, H. Winter, K. Gärtner, R. Włodarczyk, J. Sauer, and M. Sierka. Fast atom diffraction during grazing scattering from a mgo(001) surface. *Surface Science*, 606:161–173, 2012.
- [27] A. Momeni, E. M. S. Casagrande, A. Dechoux, and H. Khemliche. Ultrafast crystallization dynamics at an organic–inorganic interface revealed in real time by grazing incidence fast atom diffraction. *The Journal of Physical Chemistry Letters*, 9:908–913, 2018.
- [28] H. Khemliche, P. Rousseau, P. Roncin, V. H. Etgens, and F. Finocchi. Grazing incidence fast atom diffraction: An innovative approach to surface structure analysis. *Applied Physics Letters*, 95(15), 2009.
- [29] Diffraction of Fast Atomic Projectiles during Grazing Scattering from a LiF(001) Surface. *Physical Review Letters*, 98(1):016103, 2007.
- [30] J. Seifert, M. Busch, E. Meyer, and H. Winter. Surface structure of alanine on cu(110) via grazing scattering of fast atoms and molecules. *Phys. Rev. B*, 89:075404, Feb 2014.
- [31] A. Schüller, D. Blauth, J. Seifert, M. Busch, H. Winter, K. Gärtner, R. Włodarczyk, J. Sauer, and M. Sierka. Fast atom diffraction during grazing scattering from a mgo(001) surface. *Surface Science*, 606(3):161–173, 2012.
- [32] Dave H.A. Blank, Guus J.H.M. Rijnders, Gertjan Koster, and Horst Rogalla. In-situ monitoring during pulsed laser deposition using RHEED at high pressure. *Applied Surface Science*, 127-129:633–638, 1998.
- [33] Radko Bankras, Jisk Holleman, Jurriaan Schmitz, Marko Sturm, Andrey Zinine, Herbert Wormeester, and Bene Poelsema. In situ reflective high-energy electron diffraction analysis during the initial stage of a trimethylaluminum/water ALD process. *Chemical Vapor Deposition*, 12(5):275–279, 2006.
- [34] Hiroyuki Fujiwara, Michio Kondo, and Akihisa Matsuda. Real-time spectroscopic ellipsometry studies of the nucleation and grain growth processes in microcrystalline silicon thin films. *Physical Review B - Condensed Matter and Materials Physics*, 63(11):1–9, 2001.

- [35] Ajaib Singh, Susanne Schipmann, Aakash Mathur, Dipayan Pal, Amartya Sengupta, Uwe Klemradt, and Sudeshna Chattopadhyay. Structure and morphology of magnetron sputter deposited ultrathin ZnO films on confined polymeric template. *Applied Surface Science*, 414:114–123, 2017.
- [36] Dmitri Litvinov, Roy Clarke, Charles A. Taylor, and Darryl Barlett. Real-time strain monitoring in thin film growth: Cubic boron nitride on Si(100). *Materials Science and Engineering B: Solid-State Materials for Advanced Technology*, 66(1):79–82, 1999.
- [37] P. Atkinson, M. Eddrief, V. H. Etgens, H. Khemliche, M. Debiossac, A. Momeni, M. Mulier, B. Lalmi, and P. Roncin. Dynamic grazing incidence fast atom diffraction during molecular beam epitaxial growth of GaAs. *Applied Physics Letters*, 105, 2014.
- [38] Gabor A. Somorjai and Yimin Li. Impact of surface chemistry. *Proceedings of the National Academy of Sciences of the United States of America*, 108(3):917–924, 2011.
- [39] Andrew Zangwill. *Physics at Surfaces*. Cambridge University Press, ISBN = 9780511622564., 1988.
- [40] John H. Sinfelt. Role of surface science in catalysis. *Surface Science*, 500(1-3):923–946, 2002.
- [41] *kSA 400 Analytical RHEED System Product Specifications*; <https://k-space.com/product/400-rheed/>.
- [42] I. Estermann and O. Stern. Beugung von Molekularstrahlen. *Zeitschrift für Physik*, 61(1-2):95–125, 1930.
- [43] B. J. Hinch, C. Koziol, J. P. Toennies, and G. Zhang. Evidence for quantum size effects observed by helium atom scattering during the growth of Pb on Cu(111). *EPL*, 10(4):341–346, 1989.
- [44] M. J. Cardillo, C. S.Y. Ching, E. F. Greene, and G. E. Becker. Molecular-Beam Apparatus for the Study of Gas-Surface Interactions. *J Vac Sci Technol*, 15(2):423–428, 1978.
- [45] K. H. Rieder and T. Engel. Atomic beam diffraction from solid surfaces. *Nuclear Instruments and Methods*, 170(1-3):483–487, 1980.
- [46] G. A. Bocan, H. Breiss, S. Szilasi, A. Momeni, E. M. Staicu Casagrande, M. S. Gravielle, E. A. Sánchez, and H. Khemliche. Anomalous KCl(001) Surface Corrugation from Fast He Diffraction at Very Grazing Incidence. *Physical Review Letters*, 125(9):96101, 2020.
- [47] G.A. Bocan and M.S. Gravielle. GIFAD for He/KCl(001). Structure in the pattern for $\langle 110 \rangle$ incidence as a measure of the projectile-cation interaction. *Nuclear Instruments and Methods in Physics Research, Section B: Beam Interactions with Materials and Atoms*, 421:1–6, 2018.

- [48] H. Winter, A. Schüller, J. Seifert, J. Lienemann, S. Wethekam, and M. Busch. Fast atom diffraction at surfaces. *Journal of Physics: Conference Series*, 388, 2012.
- [49] Patrick Rousseau, Hocine Khemliche, Nenad Bundaleski, Pierre Soullisse, Anouchah Momeni, and Philippe Roncin. Surface analysis with grazing incidence fast atom diffraction (GIFAD). *Journal of Physics: Conference Series*, 133, 2008.
- [50] G. A. Bocan, H. Breiss, S. Szilasi, A. Momeni, E. M. Staicu Casagrande, E. A. Sánchez, M. S. Gravielle, and H. Khemliche. Dynamical effects as a window into van der Waals interactions in grazing-incidence fast He-atom diffraction from KCl(001). *Physical Review B*, 104(23):1–10, 2021.
- [51] M. Debiossac, A. Zugarramurdi, H. Khemliche, P. Roncin, A. G. Borisov, A. Momeni, P. Atkinson, M. Eddrief, F. Finocchi, and V. H. Etgens. Combined experimental and theoretical study of fast atom diffraction on the $\beta_2(2\times 4)$ reconstructed GaAs(001) surface. *Physical Review B - Condensed Matter and Materials Physics*, 90(15):1–13, 2014.
- [52] Daniel R Frankl. SURFACE SCIENCE LETTERS COMMENTS ON “COHERENCE Daniel R. FRANKL. 84:485–488, 1979.
- [53] J. T. Gudmundsson. Physics and technology of magnetron sputtering discharges. *Plasma Sources Science and Technology*, 29(11), 2020.
- [54] P. Bílková, B. Mitu, V. Marotta, G. Mattei, S. Orlando, and A. Santagata. Reactive pulsed laser deposition of zinc oxide thin films. *Applied Physics A: Materials Science and Processing*, 79(4-6):1061–1065, 2004.
- [55] Niclas S. Mueller, Anthony J. Morfa, Daniel Abou-Ras, Valerio Oddone, Tymoteusz Ciuk, and Michael Giersig. Growing graphene on polycrystalline copper foils by ultra-high vacuum chemical vapor deposition. *Carbon*, 78:347–355, 2014.
- [56] Hongfu Sun, Chengyu Wang, Shihong Pang, Xiping Li, Ying Tao, Huajuan Tang, and Ming Liu. Photocatalytic TiO₂ films prepared by chemical vapor deposition at atmosphere pressure. *Journal of Non-Crystalline Solids*, 354(12-13):1440–1443, 2008.
- [57] T. Ojima, T. Tainosho, S. Sharmin, and H. Yanagihara. RHEED oscillations in spinel ferrite epitaxial films grown by conventional planar magnetron sputtering. *AIP Advances*, 8(4), 2018.
- [58] William Lichten. Resonant charge exchange in atomic collisions. *Physical Review*, 131(1):229–238, 1963.
- [59] R. S. Gao, L. K. Johnson, D. A. Schafer, J. H. Newman, K. A. Smith, and R. F. Stebbings. Absolute

- differential cross sections for small-angle He^+ -He elastic and charge-transfer scattering at keV energies. *Physical Review A*, 38(6):2789–2793, 1988.
- [60] M. Renier and A. Draperi. A differential pumping system for one of the ESRF ultra-high vacuum beamlines. *Vacuum*, 48(5):405–407, 1997.
- [61] Y. Tamenori. Development of a differential pumping system for soft X-ray beamlines for windowless experiments under normal atmospheric conditions. *Journal of Synchrotron Radiation*, 17(2):243–249, 2010.
- [62] *Instruction Manual: Extorr XT Series RGA; Model- XT300(M)*, 2006.
- [63] *Compression ratio of turbopumps*, <https://www.pfeiffer-vacuum.com/filepool/file/tips-and-tricks/compression-ratio-of-turbopumps>.
- [64] *User Manual: IONEC - Ion Sputter Gun MODEL IG35-DP with exchangeable apertures Precision Power Supply : Model IG35-DP*; <http://www.ocivm.com>.
- [65] *Owner's operation and maintenance manual of the precautions to assure the proper operation of your MAK Source, Model-L130A01CF, MeiVac Inc.*, 2006.
- [66] Joseph Ladislav Wiza. Microchannel plate detectors. *Nuclear Instruments and Methods*, 162(1-3):587–601, 1979.
- [67] *Photonis advanced performance detector*, <https://www.photonis.com/products/advanced-performance-detectors>, 2019.
- [68] M. Busch, A. Schüller, S. Wethekam, and H. Winter. Fast atom diffraction at metal surface. 603(3):L23–L26, 2009.
- [69] Pengfei Zhu, Y. Zhu, Y. Hidaka, L. Wu, J. Cao, H. Berger, J. Geck, R. Kraus, S. Pjetrov, Y. Shen, R. I. Tobey, J. P. Hill, and X. J. Wang. Femtosecond time-resolved MeV electron diffraction. *New Journal of Physics*, 17(6), 2015.
- [70] Klaus Hornberger, Stefan Uttenthaler, Björn Brezger, Lucia Hackermüller, Markus Arndt, and Anton Zeilinger. Collisional decoherence observed in matter wave interferometry. *Phys. Rev. Lett.*, 90:160401, 2003.
- [71] Maxime Debiossac, Peng Pan, and Philippe Roncin. Grazing incidence fast atom diffraction, similarities and differences with thermal energy atom scattering (TEAS). *Physical Chemistry Chemical Physics*, 23(13):7615–7636, 2021.
- [72] Anton Tamtögl, Adrian Ruckhofer, Davide Campi, William Allison, and Wolfgang E. Ernst.

- Atom-surface van der Waals potentials of topological insulators and semimetals from scattering measurements. *Physical Chemistry Chemical Physics*, 23(13):7637–7652, 2021.
- [73] M. Minniti, C. Díaz, J. L. Fernández Cuñado, A. Politano, D. MacCariello, F. Martín, D. Farías, and R. Miranda. Helium, neon and argon diffraction from Ru(0001). *Journal of Physics Condensed Matter*, 24(35), 2012.
- [74] M. Mayrhofer-Reinhartshuber, P. Kraus, A. Tamtögl, S. Miret-Artés, and W. E. Ernst. Helium-surface interaction potential of Sb(111) from scattering experiments and close-coupling calculations. *Physical Review B - Condensed Matter and Materials Physics*, 88(20):1–11, 2013.
- [75] L. Füstöss and G. Varga. Simple hard corrugated wall model computations. *Vacuum*, 40(1-2):47–50, 1990.
- [76] N. Esbjerg and J. K. Nørskov. Dependence of the He-Scattering Potential at Surfaces on the Surface-Electron-Density Profile. *Physical Review Letters*, 45(10):807–810, 1980.
- [77] M. S. Gravielle and J. E. Miraglia. Semiquantum approach for fast atom diffraction: Solving the rainbow divergence. *Physical Review A - Atomic, Molecular, and Optical Physics*, 90(5):1–6, 2014.
- [78] María Silvia Gravielle, Jorge Esteban Miraglia, and Leandro Frisco. Coherence-length effects in fast atom diffraction at grazing incidence. *Atoms*, 6(4):1–16, 2018.
- [79] H. Winter and A. Schüller. Fast atom diffraction during grazing scattering from surfaces. *Progress in Surface Science*, 86(9-10):169–221, 2011.
- [80] J. R. Manson, Hocine Khemliche, and Philippe Roncin. Theory of grazing incidence diffraction of fast atoms and molecules from surfaces. *Physical Review B - Condensed Matter and Materials Physics*, 78(15), 2008.
- [81] W. Chen, A. Kahn, P.Soukiassian, P.S.Mangat, J. Gaines, C.Ponzoni, and D.Olego. ZnSe(100) surface: Atomic configurations, composition, and surface dipole. *Phys. Rev. B*, 49(15):790–794, 1994.
- [82] Patrick Rousseau, Hocine Khemliche, Nenad Bundaleski, Pierre Soullisse, Anouchah Momeni, and Philippe Roncin. Surface analysis with grazing incidence fast atom diffraction (gifad). *Journal of Physics: Conference Series*, 133(1):012013, oct 2008.
- [83] D. Farías, M. Patting, K. H. Rieder, and J. R. Manson. Scattering of He atoms from surface defects by grazing-angle diffraction beams. *Physical Review B - Condensed Matter and Materials Physics*, 65(16):1654351–16543511, 2002.

- [84] L. Frisco and M. S. Gravielle. Terrace effects in grazing-incidence fast atom diffraction from a LiF(001) surface. *Physical Review A*, 106(6):1–8, 2022.
- [85] David N. Ruzic and Samuel A. Cohen. Total scattering cross sections and interatomic potentials for neutral hydrogen and helium on some noble gases. *The Journal of Chemical Physics*, 83(11):5527–5530, 12 1985.
- [86] Mikis Mylonakis, Saurabh Pandey, Kostas G. Mavrikis, Giannis Drougakis, Georgios Vasilakis, Dimitris G. Papazoglou, and Wolf von Klitzing. Simple precision measurements of optical beam sizes. *Applied Optics*, 57(33):9863, 2018.
- [87] D. E. Nitz K. A. Smith R. S. Gao, L. K. Johnson and R. F. Stebbings. Absolute differential cross sections for small-angle elastic scattering in helium - rare-gas collisions at kev energies. *Physical Review A*, 36(7):1–6, 2018.
- [88] D. V. Karlovets, G. L. Kotkin, and V. G. Serbo. Scattering of wave packets on atoms in the born approximation. *Physical Review A - Atomic, Molecular, and Optical Physics*, 92, 2015.
- [89] L. Sarkadi, I. Fabre, F. Navarrete, and R. O. Barrachina. Loss of wave-packet coherence in ion-atom collisions. *Physical Review A*, 93(3):1–6, 2016.
- [90] W. Patrick Mccray. MBE deserves a place in the history books. *Nature Nanotechnology*, 2(5):259–261, 2007.
- [91] Dave H.A. Blank, Guus J.H.M. Rijnders, Gertjan Koster, and Horst Rogalla. In-situ monitoring by reflective high energy electron diffraction during pulsed laser deposition. *Applied Surface Science*, 138-139(1-4):17–23, 1999.
- [92] G. Lehmpfuhl, A. Ichimiya, and H. Nakahara. Interpretation of RHEED oscillations during MBE growth. *Surface Science*, 245(1-2), 1991.
- [93] J. T. Gudmundsson, N. Brenning, D. Lundin, and U. Helmersson. High power impulse magnetron sputtering discharge. *Journal of Vacuum Science Technology A: Vacuum, Surfaces, and Films*, 30(3):030801, 2012.
- [94] H. D. Zeh. On the interpretation of measurement in quantum theory. *Foundations of Physics*, 1(1):69–76, 1970.
- [95] Maximilian Schlosshauer. Quantum decoherence. *Physics Reports*, 831:1–57, 2019. Quantum decoherence.
- [96] Alexander A. Milner, Aleksey Korobenko, John W. Hepburn, and Valery Milner. Effects of ultra-fast molecular rotation on collisional decoherence. *Physical Review Letters*, 113(4):1–5, 2014.

- [97] Klaus Hornberger and John E. Sipe. Collisional decoherence reexamined. *Physical Review A - Atomic, Molecular, and Optical Physics*, 68(1):16, 2003.
- [98] E. Joos and H.D. Zeh. The emergence of classical properties through interaction with the environment. 59:223–243, 1985.
- [99] Claus Kiefer. Quantum Electrodynamics and Quantum Gravity. *Physical Review D*, 46(4), 1992.
- [100] Hermann Uys, John D. Perreault, and alexander D. Cronin. Matter-wave decoherence due to a gas environment in an atom interferometer. *Physical Review Letters*, 95(15):2–5, 2005.
- [101] G. Ithier, E. Collin, P. Joyez, P. J. Meeson, D. Vion, D. Esteve, F. Chiarello, A. Shnirman, Y. Makhlin, J. Schrieffer, , and G. Schön. Decoherence in a superconducting quantum bit circuit. *Physical Review B - Condensed Matter and Materials Physics*, 72(13):1–22, 2005.
- [102] M. O. Terra Cunha and M. C. Nemes. Towards an understanding of decoherence in ion traps. *Physics Letters, Section A: General, Atomic and Solid State Physics*, 329(6):409–413, 2004.
- [103] Berthold Georg Englert. Fringe visibility and which-way information: An inequality. *Physical Review Letters*, 77:2154–2157, 1996.
- [104] C. P. Sun, D. L. Zhou, S. X. Yu, and X. F. Liu. Quantum decoherence from adiabatic entanglement with external one or a few degrees of freedom. *European Physical Journal D*, 13:145–155, 2001.
- [105] Grazing incidence diffraction of keV helium atoms on a Ag(110) surface. *Physical Review Letters*, 101(17):1–4, 2008.
- [106] A. Mukherjee, A. Momeni, A. R. Allouche, E. M. Staicu Casagrande, T. Minea, and H. Khemliche. Grazing incidence fast atom diffraction in high-pressure conditions. *Surfaces and Interfaces*, 37:102754, 2023.
- [107] K. Hornberger, S. Gerlich, P. Haslinger, S. Nimmrichter, and M. klaus. Colloquium: Quantum interference of clusters and molecules. *Reviews of Modern Physics*, 84:157–173, 2012.
- [108] P. Dehmer and L. Wharton. Absolute total scattering cross sections for ^7Li on He, Ne, Kr, and Xe. *The Journal of Chemical Physics*, 57:4821–4835, 1972.
- [109] C. Seidel, R. Ellerbrake, L. Gross, and H. Fuchs. Structural transitions of perylene and coronene on silver and gold surfaces: A molecular-beam epitaxy LEED study. *Physical Review B - Condensed Matter and Materials Physics*, 64(19):1954181–19541810, 2001.
- [110] Jianming Wen, Yong Zhang, and Min Xiao. The talbot effect: recent advances in classical optics, nonlinear optics, and quantum optics. *Advances in Optics and Photonics*, 5:83, 2013.

- [111] M. Berry, I. Marzoli, and W. Schleich. *Quantum carpets, carpets of light*. 2001, https://www.worldscientific.com/doi/abs/10.1142/9789813221215_0018.
- [112] S. Srisuphaphon, W. Temnuch, S. Buathong, and S. Deachapunya. Matter-wave interferometry from near-field to far-field diffraction. *Journal of Physics: Conference Series*, 1380, 2019.
- [113] A. S. Sanz and S. Miret-Arts. A causal look into the quantum talbot effect. *Journal of Chemical Physics*, 126:1–11, 2007.
- [114] A. S. Sanz, F. Borondo, and S. Miret-Artés. Causal trajectories description of atom diffraction by surfaces. *Physical Review B - Condensed Matter and Materials Physics*, 61:7743–7751, 2000.
- [115] Klaus Hornberger and John E. Sipe. Collisional decoherence reexamined. *Phys. Rev. A*, 68:012105, 2003.
- [116] D. V. Karlovets, G. L. Kotkin, and V. G. Serbo. Scattering of wave packets on atoms in the born approximation. *Phys. Rev. A*, 92:052703, 2015.
- [117] Markus Arndt, Stefan Gerlich, and Klaus Hornberger. *Experimental Decoherence in Molecule Interferometry*. Springer International Publishing, 2022.
- [118] G. Schütz, A. Rembold, A. Pooch, W. T. Chang, and A. Stibor. Electron matter wave interferences at high vacuum pressures. *Measurement: Journal of the International Measurement Confederation*, 68, 2015.
- [119] Irving Langmuir. Oscillations in ionized gases. *Proceedings of the National Academy of Sciences*, 14:627–637, 1928.
- [120] Brian Chapman. Glow discharge processes. *John Wiley and Sons, Inc*, 1980.
- [121] Li Fan, Jiao Junkai, Luo Haiyun, Du Juan, and Lin Feng. Preliminary Study of Glow Discharge Plasma on the Static Pressure Measurement. pages 1–7, 2017.
- [122] Michel A. Liberman and Allan J. Lichtenberg. *Principles of Plasma Discharges and Materials Processing*. A JOHN WILEY SONS, INC PUBLICATION, 2005.
- [123] Paul A. Lindfors, William M. Mularie, and Gottfried K. Wehner. Cathodic arc deposition technology. *Surface and Coatings Technology*, 29:275–290, 1986.
- [124] W. R. Grove. On the electro-chemical polarity of gases. *Philosophical Transactions*, 142:87–101, 1852.
- [125] Peter Sigmund. Recollections of fifty years with sputtering. *Thin Solid Films*, 520:6031–6049, 2012.

- [126] Jeon G. Han. Recent progress in thin film processing by magnetron sputtering with plasma diagnostics. *Journal of Physics D: Applied Physics*, 42, 2009.
- [127] G. Bräuer, B. Szyszka, M. Vergöhl, and R. Bandorf. Magnetron sputtering - milestones of 30 years. *Vacuum*, 84:1354–1359, 2010.
- [128] S. Mondal and S. Bhattacharyya. Performance of a size-selected nanocluster deposition facility and in situ characterization of grown films by x-ray photoelectron spectroscopy. *Review of Scientific Instruments*, 85:065109–065109, 06 2014.
- [129] I. Petrov, A. Myers, J. E. Greene, and J. R. Abelson. Mass and energy resolved detection of ions and neutral sputtered species incident at the substrate during reactive magnetron sputtering of ti in mixed ar+n 2 mixtures. *Journal of Vacuum Science Technology A: Vacuum, Surfaces, and Films*, 12:2846–2854, 1994.
- [130] J. T. Gudmundsson, D. Lundin, G. D. Stancu, N. Brenning, and T. M. Minea. Are the argon metastables important in high power impulse magnetron sputtering discharges? *Physics of Plasmas*, 22, 2015.
- [131] Dmitriy A. Golosov. Balanced magnetic field in magnetron sputtering systems. *Vacuum*, 139:109–116, 2017.
- [132] P.J Kelly and R.D Arnell. Magnetron sputtering: a review of recent developments and applications. *Vacuum*, 56(3):159–172, 2000.
- [133] Rieschl et al. METHOD OF HIPIMS SPUTTERING AND HIPIMS SPUTTER SYSTEM, n°US009624572B2 . 2017.
- [134] K. Macák, V. Kouznetsov, J. Schneider, U. Helmersson, and I. Petrov. Ionized sputter deposition using an extremely high plasma density pulsed magnetron discharge. *Journal of Vacuum Science Technology A: Vacuum, Surfaces, and Films*, 18:1533–1537, 2000.
- [135] Vladimir Kouznetsov, Karol MacÁk, Jochen M. Schneider, Ulf Helmersson, and Ivan Petrov. A novel pulsed magnetron sputter technique utilizing very high target power densities. *Surface and Coatings Technology*, 122:290–293, 1999.
- [136] Daniel Lundin and Kostas Sarakinos. An introduction to thin film processing using high-power impulse magnetron sputtering. *Journal of Materials Research*, 27:780–792, 2012.
- [137] C. Christou and Z. H. Barber. Ionization of sputtered material in a planar magnetron discharge. *Journal of Vacuum Science Technology A: Vacuum, Surfaces, and Films*, 18:2897–2907, 2000.
- [138] E. J. Iglesias, A. Hecimovic, F. Mitschker, M. Fiebrandt, N. Bibinov, and P. Awakowicz.

- Ultraviolet/vacuum-ultraviolet emission from a high power magnetron sputtering plasma with an aluminum target. *Journal of Physics D: Applied Physics*, 53, 2020.
- [139] A. P. Mills and William S. Crane. Emission of band-gap-energy positrons from surfaces of lif, naf, and other ionic crystals. *Physical Review Letters*, 53:2165–2168, 1984.
- [140] Roberto Núñez-González, R. Aceves, José Luis Cabellos, and Alvaro Posada-Amarillas. Effect of substitutional cu atoms on the electronic and optical properties of KCl: A dft approach. *Materials Today Communications*, 22, 2020.
- [141] G. D. Stancu, N. Brenning, C. Vitelaru, D. Lundin, and T. Minea. Argon metastables in HiPIMS: Validation of the ionization region model by direct comparison to time resolved tunable diode-laser diagnostics. *Plasma Sources Science and Technology*, 24:45011, 2015.
- [142] Hyung Jin Choi, Byeong Ju Park, Ji Ho Eom, Min Ju Choi, and Soon Gil Yoon. Achieving Antifingerprinting and Antibacterial Effects in Smart-Phone Panel Applications Using ZnO Thin Films without a Protective Layer. *ACS Applied Materials and Interfaces*, 8(1):997–1003, 2016.
- [143] Bih Show Lou, Wei Ting Chen, Wahyu Diyatmika, Jong Hong Lu, Chen Te Chang, Po Wen Chen, and Jyh Wei Lee. High power impulse magnetron sputtering (HiPIMS) for the fabrication of antimicrobial and transparent TiO₂ thin films. *Current Opinion in Chemical Engineering*, 36:100782, 2022.
- [144] Reiner Kukla. Magnetron sputtering on large scale substrates: An overview on the state of the art. *Surface and Coatings Technology*, 93(1):1–6, 1997.
- [145] Papken Ehiasarian Hovsepian, Arutiun Papken Ehiasarian, Yashodhan Purandare, Arunprabhu Arunachalam Sugumaran, Tim Marriott, and Imran Khan. Development of superlattice CrN/NbN coatings for joint replacements deposited by high power impulse magnetron sputtering. *Journal of Materials Science: Materials in Medicine*, 27(9), 2016.
- [146] R. W. Vook and C. H. Chung. Ag films formed simultaneously on (111) and (100) NaCl. *Thin Solid Films*, 37(3):461–473, 1976.
- [147] F. Reniers, M. P. Delplancke, A. Asskali, V. Rooryck, and O. Van Sinay. Glow discharge sputtering deposition of thin films of Ag, Cr, Cu, Ni, Pd, Rh and their binary alloys onto NaCl and MgO experimental parameters and epitaxy. *Applied Surface Science*, 92:35–42, 1996.
- [148] C. Gaire, F. Tang, and G. C. Wang. In-situ reflection high-energy electron diffraction study of epitaxial growth of Cu on NaCl (100) under oblique angle vapor deposition. *Thin Solid Films*, 517(16):4509–4514, 2009.